博士論文(要約)

Electron temperature and density measurements by Thomson scattering on the QUEST spherical tokamak

(QUEST球状トカマクにおける トムソン散乱による電子温度・密度の計測)

山口　隆史

Doctor Thesis

Electron temperature and density measurements by Thomson scattering on the QUEST spherical tokamak

Takashi Yamaguchi

Department of Complexity Science and Engineering
Graduate School of Frontier Sciences
The University of Tokyo

Abstract

Nuclear fusion is one candidate of future energy source. Many plasma devices have been built to study the physics of high temperature plasmas and to develop scenarios for a fusion reactor. The QUEST spherical tokamak device was built in 2008 at Kyushu University. The major radius of the device is about 0.65 m, the minor radius is about 0.4 m, and the toroidal magnetic field strength is 0.25 T. The main objective of the QUEST project is steady state operation by radiofrequency (RF) wave current drive under controlled plasma-wall interaction. QUEST is equipped with several RF systems with frequencies in the range of electron cyclotron frequency (8.2 GHz and 28 GHz were used in this experiment). Waves excited by these RF systems are used for current drive.

The electron temperature measurement by Thomson scattering is reliable, and is used in many devices. Temperature and density profiles are useful for equilibrium analysis and for studying the RF current drive mechanism. On a typical tokamak device, the electron density is usually much higher than $10^{18}\,\mathrm{m}^{-3}$. However typical electron densities of RF driven QUEST plasmas measured by a microwave interferometer is of the order of $10^{17}\,\mathrm{m}^{-3}$ - $10^{18}\,\mathrm{m}^{-3}$. Thomson scattering measurement in such a low density plasma is quite difficult, because the scattered signal intensity is proportional to the electron density. In order to provide reliable electron temperature and density profiles in QUEST RF driven plasmas, a new Thomson scattering system was developed. The Thomson scattering system is comprised of (1) a Nd:YAG laser (wavelength 1064 nm, energy 1.65 J, pulse width 7 ns, repetition rate 10 Hz, output beam diameter $< 9\,\mathrm{mm}$, and beam divergence 0.45 mrad), (2) laser incidence and light collection optics, and (3) polychromators to measure six spatial points in the plasma. The polychromator has six wavelength channels. By fitting the signals at six wavelength channels to scattered light spectrum from a Maxwellian plasma, the electron temperature can be determined. The electron density is determined from the scattered light intensity. Raman scattering was used for calibration of the relative electron density profile. By comparing the integration of the density profile along the major radius and the line integrated density measured by a microwave interferometer, an absolute density profile can be obtained.

Because the Thomson scattering signals for low-density RF driven plasmas are very weak, many scattered signals were accumulated during the long steady state period (typically ~ 10 s) and over many reproducible discharges to obtain a sufficient signal-to-noise ratio. In some cases, up to 2000 pulses were accumulated. The inboard poloidal field null configuration sustained by 8.2 GHz RF power alone, and the limiter configuration sustained by 28 GHz RF power alone were studied in detail.

For the case of the inboard poloidal field null configuration sustained by 8.2 GHz RF power alone, the plasma electron temperature was in the range of 10 – 500 eV. Unlike in typical tokamak plasmas, the temperature profile was hollow. The temperature peak position is located slightly to the low field side of the fundamental electron cyclotron resonance layer. The density is much lower than the cutoff density. When the toroidal magnetic field strength was increased, the peak position of the electron temperature moved to the low field side (large major radius side) with the fundamental electron cyclotron resonance layer, suggesting that the electrons are heated by electron cyclotron damping. The observation that the electron temperature peak is always on the low field side of the resonance layer can be interpreted by

the Doppler up-shift effect, or by the poor confinement of the plasma on the high field side because of the shrinking plasma cross section. The inboard poloidal field null configuration has an X-point (null point) on the inboard side of the tokamak, and is characterized by a very high equilibrium poloidal beta (~ 3). On the other hand, the contribution of the bulk electrons to poloidal beta measured by Thomson scattering is much smaller (~ 0.01), indicating that the contribution of fast electrons to the plasma pressure is dominant.

In the 28 GHz RF experiment, similar features in the temperature profile were observed, with the fundamental resonance replaced by the second harmonic resonance. The density is much lower than the cutoff density, and excitation of EBW by mode conversion is not expected. Comparing the plasmas sustained by 28 GHz RF power (200 kW) and by 8.2 GHz RF power (40 kW), the density is an order of magnitude higher for the 28 GHz case, which is roughly the difference in cutoff densities. The central and the inboard pressures for the 28 GHz case are about twice and four times higher than the 8.2 GHz case. Since the injected power is about five times higher for 28 GHz, the pressure difference is reasonable. The central region has the highest density and low temperature, which may be attributed to poor RF accessibility to the high density core region and poor central confinement due to collisions with neutrals or radiative cooling. For the 28 GHz case, the outboard temperature is higher than the central temperature, but lower than the inboard temperature and temperature equilibration on a flux surface is not perfect.

In order to see the EBW current drive effect, 8.2 GHz RF power was injected to a plasma sustained by 28 GHz RF power. The density was $1.7 \times 10^{18}\,\mathrm{m}^{-3}$, which is overdense for 8.2 GHz. However, a current drive effect was not observed. This is due to the low mode conversion efficiency of about 2%, calculated using the measured density profile.

In conclusion, the electron temperature and density of the low density steady state RF driven plasmas were measured successfully by the new Thomson scattering system on QUEST. Various features of the electron temperature and density were revealed. These results provide important experimental evidence for understanding spherical tokamak plasmas sustained solely by RF power.

Contents

List of Figures

List of Tables

Chapter 1

Introduction

1.1 Nuclear fusion

Power generation by nuclear fusion may solve the energy problem of the world. Among various nuclear fusion reactions, the D-T reaction has the largest reaction cross section at relatively low colliding energies, and will be used for the first generation nuclear fusion reactors [1]. The following two reactions are needed:

$$\mathrm{D} + \mathrm{T} \rightarrow \mathrm{He}^4\,(3.5\,\mathrm{MeV}) + \mathrm{n}\,(14.1\,\mathrm{MeV}), \tag{1.1}$$

$$\mathrm{n} + \mathrm{Li}^6 \rightarrow \mathrm{He}^4\,(2.1\,\mathrm{MeV}) + \mathrm{T}\,(2.7\,\mathrm{MeV}), \tag{1.2}$$

where n, D and T stand for neutron, deuterium and tritium. Since the temperature required for reaction (1.1) is as low as ~ 10 keV, the demand for plasma confinement (represented by the energy confinement time τ_E) is not so stringent. The kinetic energy of fusion-produced neutrons must be collected and converted to electric energy in a heat cycle with a thermodynamic efficiency of about 40 %.

Reaction (1.2) is necessary to produce tritium, which does not exist in nature. In the following two reactions, which occur with equal probabilities, only deuterium is required as the fuel,

$$\mathrm{D} + \mathrm{D} \rightarrow \mathrm{T}\,(1\,\mathrm{MeV}) + \mathrm{p}\,(3\,\mathrm{MeV}), \tag{1.3}$$

$$\mathrm{D} + \mathrm{D} \rightarrow \mathrm{He}^3\,(0.8\,\mathrm{MeV}) + \mathrm{n}\,(2.5\,\mathrm{MeV}). \tag{1.4}$$

In contrast to reactions (1.1) and (1.2), generation of tritium is not necessary. However, the demand for plasma confinement is more stringent.

The primary requirement for generating power by fusion is that the fusion energy output exceeds the energy input needed to sustain the plasma. This translates to the condition that the product of the ion density and the energy confinement time exceeds a critical value (Lawson criterion) [2]. For the D-T reaction,

$$n_\mathrm{i} \times \tau_\mathrm{E} \geq 1.5 \times 10^{20}\,[\mathrm{s/m^3}], \tag{1.5}$$

where n_i is the ion density. The energy confinement time τ_E represents the time scale for the plasma to lose energy, and is defined as [2]

$$\tau_\mathrm{E} = \frac{W}{P_\mathrm{H}}, \tag{1.6}$$

where W is the energy stored in the plasma and $P_{\rm H}$ is the external heating power.

1.2 Plasma

When the electrons gain kinetic energy exceeding the binding energy, either by heating or by applied electric field, atoms are ionized. This is called the plasma state.

Parameters characterizing the plasma are described below [1]. When the electron density is perturbed, the electrons undergo plasma oscillation at angular frequency

$$\omega_{\rm p} = \sqrt{\frac{n_{\rm e}e^2}{\epsilon_0 m_{\rm e}}}. \tag{1.7}$$

In a plasma, the electrostatic potential around a charge is screened by other charged particles, and extend only over the range of Debye length

$$\lambda_{\rm D} = \sqrt{\frac{\varepsilon_0 T_{\rm e}}{n_{\rm e}e^2}}. \tag{1.8}$$

A charged particle of species j in magnetic field B gyrates at cyclotron angular frequency

$$\omega_{{\rm c}j} = \frac{e_j B}{m_j}, \tag{1.9}$$

where e_j is the particle charge and m_j is the particles mass.

The most probable electron velocity distribution in thermal equilibrium is known as the Maxwell distribution. The one dimensional Maxwell distribution function is given by [1]

$$f_{\rm e}(v) = n_{\rm e}\sqrt{\frac{m_{\rm e}}{2\pi T_{\rm e}}}\exp\left(-\frac{m_{\rm e}v^2}{2T_{\rm e}}\right) = \frac{n_{\rm e}}{\sqrt{\pi}v_{\rm the}}\exp\left(-\frac{v^2}{v_{\rm the}^2}\right), \tag{1.10}$$

where $v_{\rm the}$ is the electron thermal speed. The part conforming to the Maxwell distribution is called the bulk, and the broadened skirt is called the tail of the distribution function.

An electron-electron collision frequency is [2, 3]

$$\nu_{\rm e} = \frac{\sqrt{2}}{12\pi^{3/2}}\frac{n_{\rm e}e^4\ln\Lambda}{\epsilon_0^2 m_{\rm e}^{1/2}T_{\rm e}^{3/2}} \tag{1.11}$$

$$= 2.9\times10^{-12}\frac{n_{\rm e}\ln\Lambda}{T_{\rm e}^{3/2}} \tag{1.12}$$

1.3 Waves in plasma

Typical high frequency waves and oscillations in magnetized plasmas in which electron motion is dominant and propagate across B are described below [2, 4].

Ordinary mode

The ordinary mode (O-mode) is an electromagnetic wave that propagates perpendicular to B with the wave electric field polarized parallel to B. The dispersion relation is

$$\frac{c^2k^2}{\omega^2} = 1 - \frac{\omega_{\rm p}^2}{\omega^2}. \tag{1.13}$$

The wave is cutoff (becomes evanescent) at frequencies below the plasma frequency $\omega_{\rm p}$.

Extraordinary mode

The extraordinary mode (X-mode) is an electromagnetic wave that propagates perpendicular to B with the wave electric field polarized perpendicular to B. The dispersion relation is

$$\frac{c^2k^2}{\omega^2} = 1 - \frac{\omega_{\rm p}^2}{\omega^2}\frac{\omega^2 - \omega_{\rm p}^2}{\omega^2 - \omega_{\rm p}^2 - \omega_{\rm ce}^2}. \tag{1.14}$$

The wave has two cutoffs at $\omega = \omega_{\rm R}$ and $\omega = \omega_{\rm L}$

$$\omega_{\rm R} = \frac{1}{2}\left[\omega_{\rm ce} + \sqrt{\omega_{\rm ce}^2 + \omega_{\rm p}^2}\right], \tag{1.15}$$

$$\omega_{\rm L} = \frac{1}{2}\left[-\omega_{\rm ce} + \sqrt{\omega_{\rm ce}^2 + \omega_{\rm p}^2}\right], \tag{1.16}$$

and one resonance at $\omega = \omega_{\rm UH}$

$$\omega^2 = \omega_{\rm UH}^2 = \omega_{\rm p}^2 + \omega_{\rm ce}^2. \tag{1.17}$$

Lower hybrid wave

The lower hybrid wave is an electrostatic wave, which has a resonance at $\omega = \omega_{\rm LH}$, the lower hybrid frequency,

$$\omega_{\rm LH}^2 = \left(\frac{1}{\omega_{\rm ci}^2 + \omega_{\rm pi}^2} + \frac{1}{\omega_{\rm ce}\omega_{\rm ci}}\right)^{-1}. \tag{1.18}$$

Here, ω_{ci} is the ion cyclotron frequency, ω_{pi} is the ion plasma frequency.

1.4 Magnetic confinement fusion devices

Various plasma confinement devices have been developed. Representative devices are listed in Table 1.1. Presently, the tokamak is the mainstream, and leads nuclear fusion research.

The motion of charged particles in magnetic field is constrained along magnetic field lines. A highly successful plasma performance with very good confinement and adequate stability has been demonstrated by the tokamak. The major and minor radii are denoted by R_0 and a, respectively and the elongation and triangularity are denoted by $\kappa = b/a$ and $\delta = (c+d)/2a$, respectively (Fig. 1.1). A strong toroidal field $B_{\rm T}$ and plasma current $I_{\rm p}$ are oriented in the toroidal direction (along ϕ), and are sometimes referred to as B_Φ and I_Φ. The poloidal field B_θ (or $B_{\rm p}$) oriented in the poloidal direction (along θ) is created by $I_{\rm p}$. $B_{\rm T}$ is created by the toroidal field coil (TF coil).

	confinement configuration	representative devices
Torus	Tokamak	JT-60U [5], JET [6]
	Stellarator	LHD [7], Wendelstein 7 [8]
	Reversed field pinch	RFX [9]
	Spheromak	SSPX [10]
Liner	Mirror	MFTF [11], GAMMA-10 [12]

Table. 1.1: Representative magnetic confinement fusion devices.

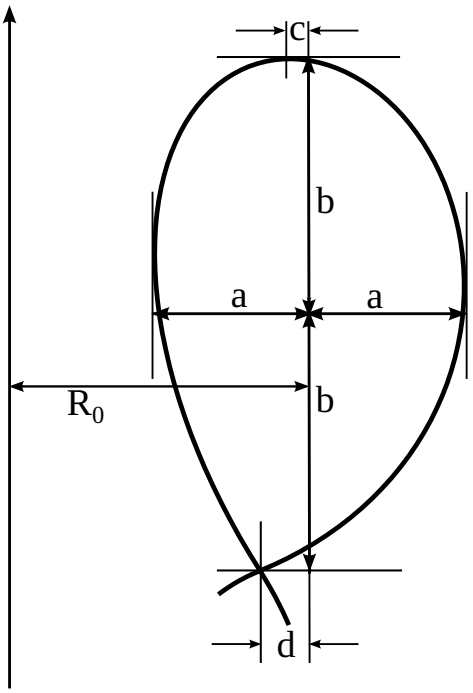

Fig. 1.1: Geometrical parameters of the tokamak cross section.

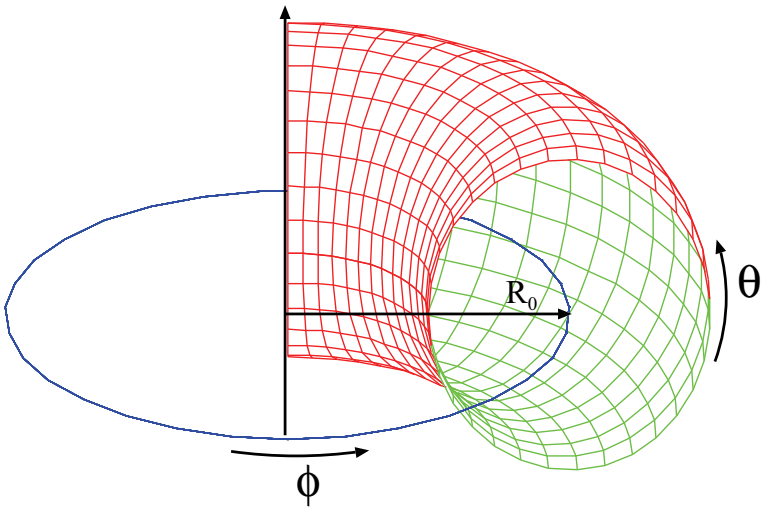

Fig. 1.2: Torooidal angle ϕ and poloidal angle θ.

The parameter β is the ratio of the plasma kinetic pressure to the confining magnetic field pressure [2, 3],

$$\beta = \frac{p}{B^2/2\mu_0}. \tag{1.19}$$

Generally, higher β is preferable, because a higher plasma pressure is confined by a relatively weak magnetic field, but there are equilibrium and stability limits imposed on β. $\beta_{\rm p}$ and $\beta_{\rm t}$ are β values defined using the poloidal and toroidal magnetic field strengths, respectively,

$$\beta_{\rm t} = \frac{\langle p \rangle}{B_\phi^2(0)/2\mu_0}, \tag{1.20}$$

$$\beta_{\rm p} = \frac{\langle p \rangle}{B_\theta^2(a)/2\mu_0}, \tag{1.21}$$

where $\langle\rangle$ denotes the volume averaged value.

The shapes of the temperature and density profiles are often modeled as

$$f(\rho) = C_0(1-\rho^2)^i, \tag{1.22}$$

where, ρ is the normalized radius

$$\rho = \frac{r}{a} \tag{1.23}$$

where r is the horizontal minor radius the flux surface ($0 \le r \le a$).

When the plasma is in force balance,

$$\nabla p = \mathbf{j} \times \mathbf{B}, \tag{1.24}$$

$$\mathbf{B} \cdot \nabla \Psi = 0, \tag{1.25}$$

$$p = p(\Psi). \tag{1.26}$$

The plasma pressure p is constant on the magnetic flux surface (surface of constant poloidal magnetic flux) labeled by the poloidal flux Ψ.

In the tokamak equilibrium, the relationship between the poloidal beta and the externally applied vertical magnetic field B_v is given by [2]

$$B_\mathrm{v} = -\frac{\mu_0 I_\mathrm{p}}{4\pi R}\left(\ln\frac{8R}{a} + \Lambda - \frac{1}{2}\right), \tag{1.27}$$

$$\Lambda = \beta_\mathrm{p} + \frac{l_\mathrm{i}}{2} - 1. \tag{1.28}$$

Λ is called the Shafranov lambda, and l_i is the internal inductance

$$l_\mathrm{i} = \frac{\langle B_\mathrm{p}^2\rangle}{B_\mathrm{p}(a)^2}, \tag{1.29}$$

where $B_p(a)$ is the poloidal magnetic field at the plasma boundary.

The trapped particle move in a banana orbit affected by mirror effect of toroidal magnetic field in small collision. The bootstrap current can be estimated by the following equation [2,3]

$$J = \frac{\sqrt{\epsilon}}{B_\theta}\frac{dp}{dr}. \tag{1.30}$$

This appears at case of small collision frequency. ν_PS and ν_B are the characteristic collision frequencies of the Pfirsch-Shlüter and banana regimes, respectively [3],

$$\nu_\mathrm{PS} = \frac{v_\mathrm{the}}{Rq} \tag{1.31}$$

$$\nu_\mathrm{B} = \left(\frac{r}{R}\right)^{3/2}\nu_\mathrm{PS} \tag{1.32}$$

v_the is thermal velocity ($=\sqrt{kT_\mathrm{e}/m}$), and q is safety factor,

$$q = \frac{r}{R}\frac{B_\mathrm{T}}{B_\mathrm{p}}. \tag{1.33}$$

The banana regime condition is $\nu_\mathrm{e} < \nu_\mathrm{B}$, trapped particle and untrapped particle can move the circuit of torus. The case of $\nu_\mathrm{e} > \nu_\mathrm{PS}$ is called Pfirsch-Shlüter regime, trapped particle and untrapped particle cannot move the circuit of torus, and plasma is treated as magnetohydrodynamics. The case of $\nu_\mathrm{B} < \nu_\mathrm{e} < \nu_\mathrm{PS}$ is called plateau regime.

The International Tokamak Experimental Reactor (ITER) [13] is being built by international collaboration among Japan, EU, USA, Russia, Korea, China, and India. The main objective of ITER is to achieve $Q = 10$, where Q is the amplification factor defined as the fusion output power divided by the heating input power, and thus to explore the physics of burning plasmas in which the alpha particle heating becomes the primary heating source.

In the past two decades, the low-aspect-ratio tokamak, more commonly called the spherical tokamak (ST) [14], has made a dramatic progress. The ST has both good confinement and superior stability at high beta. The maximum stable normalized beta and the elongation are functions of the aspect ratio, and they can be much higher in ST than in conventional tokamaks. It is hoped that the ST can contribute greatly to accelerating the development of fusion as a commercial power source.

1.5 Non-inductive plasma current start-up

Due to the very limited space at the center of the device, ST reactors require initiating the plasma current and forming the ST configuration without using the central solenoid. Non-inductive plasma current start-up using the electron cyclotron wave is one such method, and many experiments on ST devices have been performed. However, the physics mechanism is still not clearly understood. In addition, the current jump, which occurs when closed flux surfaces start to form, is not understood completely. Since the phase-space (i.e., spatial and velocity space) distribution of the electrons is crucial for these studies, the electron temperature measurement is very important.

In the early 1980 ' s, non-inductive start-up experiments using the lower hybrid wave were demonstrated successfully on WT-2 [15], JIPP-II [16], PLT [17], and Alcator-C [18]. TRIAM-1M has the longest discharge duration record [19]. The main absorption mechanism of the lower hybrid wave is Landau damping. On WT-3, X-ray measurements were performed to obtain information on the electron temperature profile. During the initial phase of EC heating, the electron temperature around the EC resonance was higher than in the central region, but during the sustainment phase, the electron temperature was centrally peaked [20].

Many experiments were performed by injecting Electron cyclotron wave(ECW) to Ohmically (inductively) formed target plasmas. In these experiments, the electron temperature profile is almost always peaked at the center [21–23]. In addition, many non-inductive plasma current start-up experiments using ECW were performed. On DIII-D, ECW at 60 GHz was launched from the high field side with a low loop voltage, and a plasma currents up to 33 kA have been obtained [24]. ECW at 110 GHz was used on JT-60U, and a plasma current is initiated and increased up to 20 kA under a vertical field having a high decay index [25].

On TST-2, current start-up and sustainment are studied using waves in various frequency ranges. On TST-2@K (TST-2 experiment at Kyushu University), ECW with a frequency of 8.2 GHz was used, and plasma currents of up to 4 kA were achieved. The line averaged electron density was about $6 \times 10^{17}\mathrm{m}^{-3}$ [26]. On TST-2 (at the University of Tokyo) ECW with a frequency of 2.45 GHz was used for plasma generation, and plasma currents of up to 1.2 kA were obtained [27]. RF wave at 21 MHz (corresponding to high harmonics of ion cyclotron frequency) was used with 2.45 GHz, and a plasma current of 1 kA was sustained [28]. Recently, successful start-up using the 200 MHz lower hybrid wave was demonstrated on TST-2. Plasma current ramp-up to 15 kA was achieved [29]. Using the plasma generated by ECW at 8.2 GHz at higher toroidal field, the plasma current was ramped up to 10 kA by LHW at 200 MHz [30].

The ECW cannot propagate in the high density region exceeding the cutoff density. However, the electron Bernstein wave (EBW), which is an electrostatic wave that can propagate above the cutoff density, can be generated by mode conversion from the ECW near the upper hybrid resonance layer [31–33]. EBW is used for heating in many STs [34–37]. Since the ST plasmas typically have high beta and high density, the ECW launched from the low magnetic field side is reflected at the cutoff layer before reaching the EC resonance layer.

On LATE, current jump was observed [38]. In this experiment 2.45 GHz was used, and the plasma current reached 10.5 kA. The line averaged electron density was about $5.5 \times 10^{17}\mathrm{m}^{-3}$. Since the cutoff density for 2.45 GHz is $7.5 \times 10^{16}\mathrm{m}^{-3}$, the occurrence of mode-conversion from ECW to EBW was suggested. On MAST, the electron temperature profile was measured during a plasma start-up experiment using the EBW [39]. X to EBW conversion method is used in this experiments. X-mode wave is injected from high field side by using reflection plate.

The peak of electron temperature is at about fundamental resonance.

1.6 Thomson scattering system

In 1968, the first generation tokamak in Russia claimed to have achieved a high electron temperature, which was confirmed by Thomson scattering (TS) measurement using a laser from the UK [40]. This result made the tokamak the mainstream of nuclear fusion research. Presently, the Thomson scattering system is used as a standard diagnostics in ASDEX-U [41], JT-60 [43], MAST [44], DIII-D [45] etc.

In glow discharge and electron cyclotron resonance (ECR) plasma experiments, the electron density is orders of magnitude less than fusion plasmas. TS measurements utilize the accumulation method [46–49]. ECR plasmas are widely used in the semiconductor processing industry. The minimum value of density measured by Thomson scattering is $5 \times 10^{15}\mathrm{m}^{-3}$ [50].

The TS system used on ASDEX used a Q-switched Nd:YAG laser and Si-APD (avalanche photodiode) for the first time [51]. The Q-switched Nd:YAG laser can create short and very intense pulses. The Si-APD has a high sensitivity in the near-infrared spectral region.

The TS system installed on the Large Helical Device (LHD) is characterized by high spatial resolution and high repetition rate [42]. The number of spatial points is 200 and the repetition rate is 4×50 Hz. An array of 200 optical fibers with a core diameter of 2 mm and a separation of 2.93 mm was installed along the image of the laser beam. Even with the highly oblique backscattering configuration, spatial resolutions of $1.5 \sim 3$ cm were achieved depending on the spatial channel. These features enable novel studies such as the evolution of an island structure in the plasma.

The Thomson scattering system developed for TST-2 is compact, and its fiber has a large N.A. of 0.38 to obtain a large solid angle [52, 53]. The Thomson scattering system on QUEST was constructed under a collaboration work between the University of Tokyo and Kyushu University. On QUEST, the same types of polychromator and fiber are used.

1.7 Objectives

The main objectives of the QUEST project are steady state operation by RF current drive and controlled plasma-wall interaction. The QUEST device is equipped with RF systems with frequencies around 8 GHz and 28 GHz, in the range of the electron cyclotron frequency. These systems are used for current drive. Excitation of the EBW is expected at high density. Thomson scattering is a reliable method to measure the electron temperature and density profiles. Temperature and density profiles are useful for equilibrium analysis and for studying the physical mechanism of RF current drive. In order to provide reliable measurements of the electron temperature and density profiles, a TS system is needed on QUEST.

Chapter 2

QUEST spherical tokamak

2.1 Background and objective

QUEST stands for Q-shu University Experiments with Steady-State Spherical Tokamak [56]. Its predecessor, TRIAM-1M was a high-field (up to 8 T) superconducting tokamak that demonstrated a very long pulse (over 5 hours [19]) LH driven tokamak operation. The discharge duration was limited by wall pumping [54, 55]. Hydrogen inventory and recycling were studied extensively [55]. QUEST follows this line of research.

The nominal major radius and minor radius of QUEST are 0.65 m and 0.4 m, respectively. The toroidal magnetic field of up to 0.25 T can be sustained for long pulse operation.

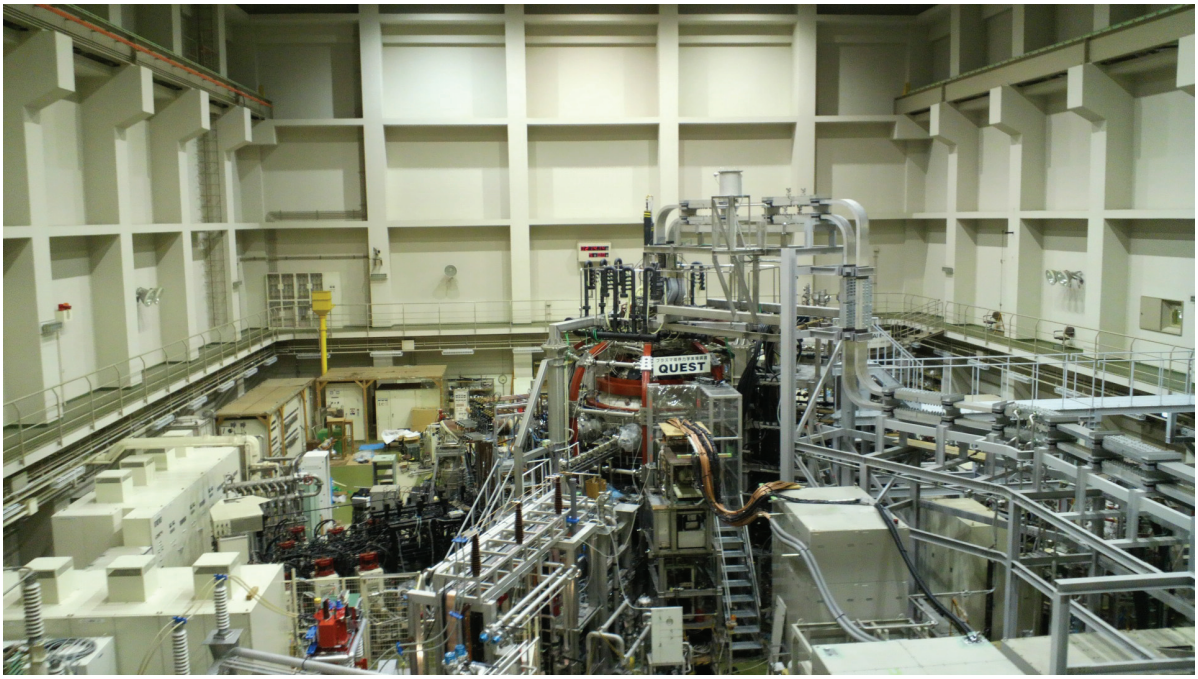

Fig. 2.1: Photograph of QUEST.

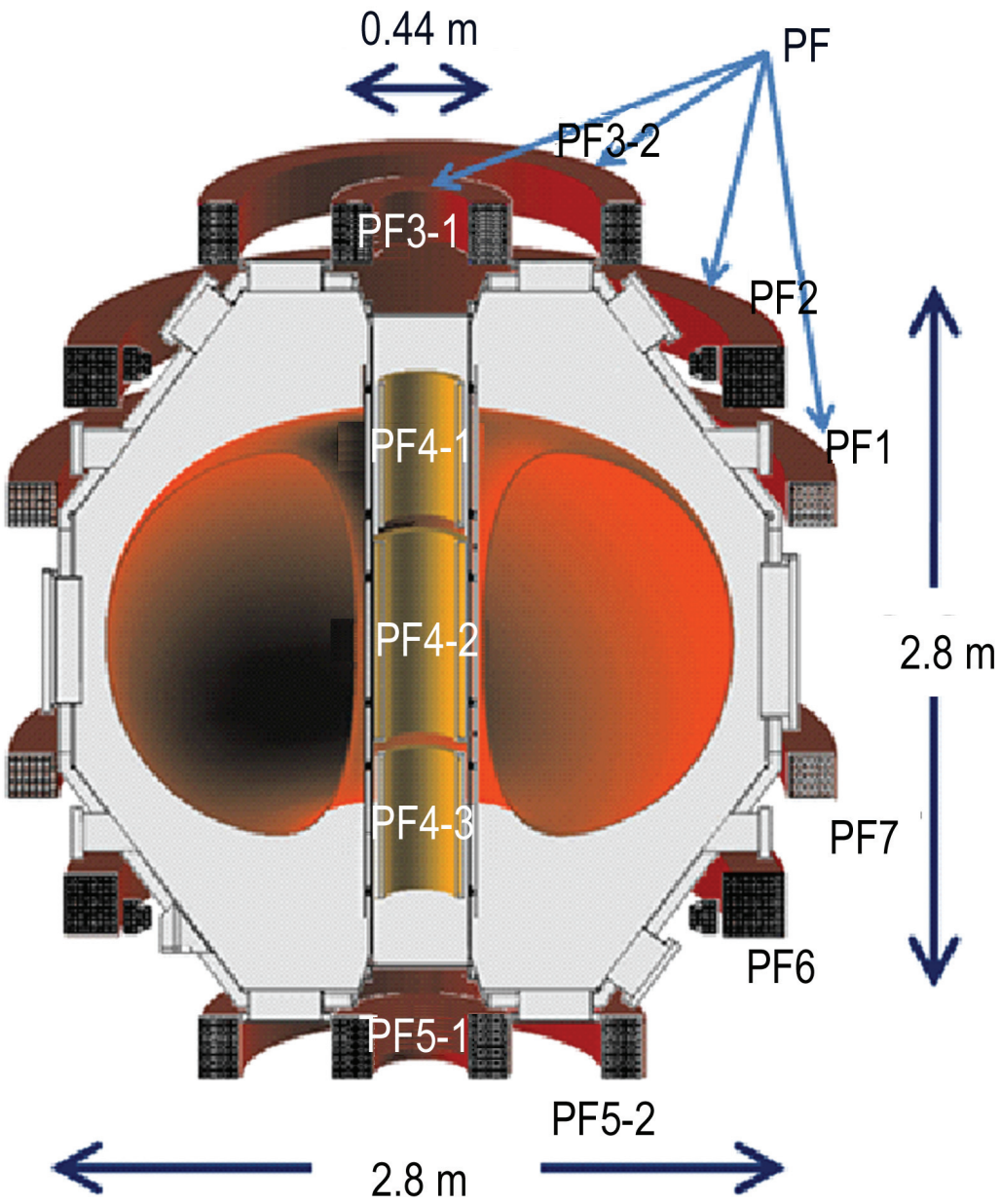

Fig. 2.2: Schematic view of QUEST [57].

TRIAM-1M ran as the predecessor of QUEST in 1986-2005. On QUEST, hot ($\geq$ 300°C) tungsten wall is being prepared as the plasma facing first wall. The temperature dependence of the retained deuterium concentrations in C, Be and W deposits was studied [58]. It can be seen that deuterium concentration can be reduced to a very low level at high temperature for tungsten.

A photograph and a schematic drawing of QUEST are shown in Fig. 2.1 and Fig. 2.2. The poloidal field coils consist of pairs PF1 & PF7, PF2 & PF6 and PF3 & PF5. PF4 is the central solenoid for inductive current drive and Ohmic heating. The toroidal magnetic field B_T [T] at

major radius R [mm] is given by

$$B_{\mathrm{T}} = 3.2 \times I_{\mathrm{TF}}/R, \tag{2.1}$$

where I_{TF} [kA] is the TF coil current.

An Ohmic heating is used for generating plasma at typical tokamak devices. The plasma has high density and high collision, and that is thermal plasma closing to maxwell distribution. RF4 coil of QUEST is used for Ohmic heating. The rise and fall of coil current generate inductive electronic field. The heating power is product of a loop voltage and a plasma current. Since coil power supply is fly wheel and don't generate rapid change, the loop voltage is small on QUEST. The experiments include Thomson scattering on QUEST are shown at Appendix A.3.

Two kind of gas hydrogen and helium are available and those gas puffed by piezo electric valve. Also compact torus (CT) injection device is installed. The objective of CT injection is central fueling [59–61]. The device provide higher particle increase than pellet injection. The injected CT plasmas have a spheromak magnetic configuration and they can penetrate the target ST plasmas by pushing away the ST magnetic field lines. The experiments include Thomson scattering on QUEST are shown at Appendix C.

2.2 Magnetic configurations

A variety of magnetic configurations can be realized on QUEST. The inboard limiter is located at $R = 230.5$ mm and the outboard limiter is located at $R = 1314$ mm. In many cases, the plasmas are limited by the inboard limiter. A typical example is shown in Fig. 2.3. Contours of equal poloidal flux are shown by dashed lines. The solid line indicates the plasma boundary defined by the last closed flux surface, in this case limited by the inboard limiter.

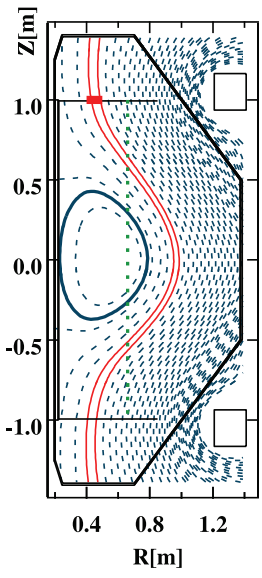

Fig. 2.3: Example of the limiter configuration equilibrium reconstructed by PCF [62]. Contours of equal poloidal flux are shown. The solid line indicates the last closed flux surface.

QUEST has flat divertor plates at the upper and lower sides of the vacuum vessel. In the

divertor configuration, the field lines on the separatrix surface, which separates the closed flux surface region from the open field region, intersect either a divertor plate (top, bottom, or both). Divertor configurations with the poloidal field null (X-point) located on the top and bottom are shown in Fig. 2.4.

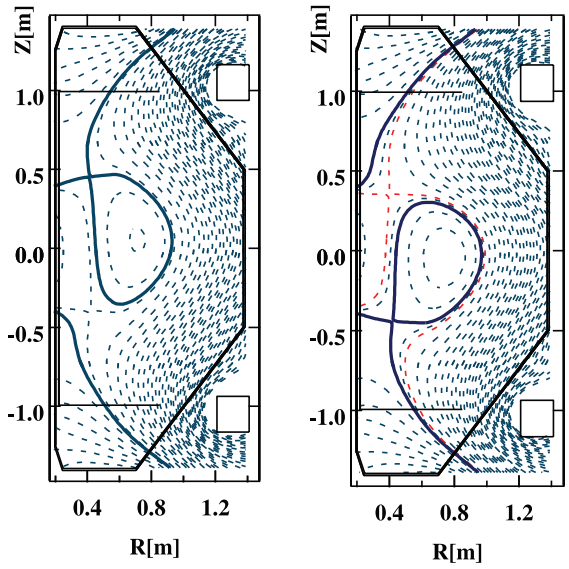

Fig. 2.4: Examples of the upper single-null (left) and lower single-null (right) divertor configurations reconstructed by PCF [62].

The inboard poloidal field null configuration has an X-point on the inboard side of the tokamak (Fig. 2.5), and is characterized by a very high poloidal beta $\beta_{\rm p}$, $\epsilon\beta_{\rm p} \gtrsim 1.25$. This configuration was also observed on TFTR [63]. A naturally diverted configuration is formed, but the plasma volume becomes very small.

2.3 Diagnostics

Photon emission from the plasma can be measured by photon detectors such as the absolute extreme ultraviolet (AXUV) photodiode, which is sensitive to photons over a wide range of energy. Line emissions including the Hα line (657.7 nm) and the OII line (465.3 nm) are measured by a visible spectrometer. SBD detectors are sensitive to soft X-ray photons. Figure 2.6 shows the sensitivity of SBD used on QUEST. Measurements of hard X-rays emitted by energetic electrons (10–500 keV) are performed using CdTe semiconductor detectors [64].

The line integrated density is measured by a microwave (140 GHz) interferometer system. The measurement sightline is along the major radius on the equatorial plane. The incident microwave is reflected from the inboard wall, and makes a round-trip.

QUEST is equipped with 67 flux loops and a Rogowski coil. Equilibrium flux surfaces are reconstructed by equilibrium codes such as EFIT [65] using these measurements. The parabolic current fitting (PCF) code was developed for ECH start-up experiments on LATE [66, 67]. The current profile is modeled by a power law parabolic profile bounded by four

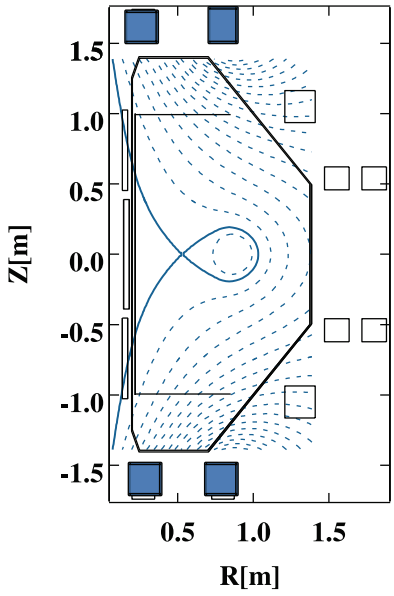

Fig. 2.5: Example of the inboard poloidal field null configuration reconstructed by PCF [62].

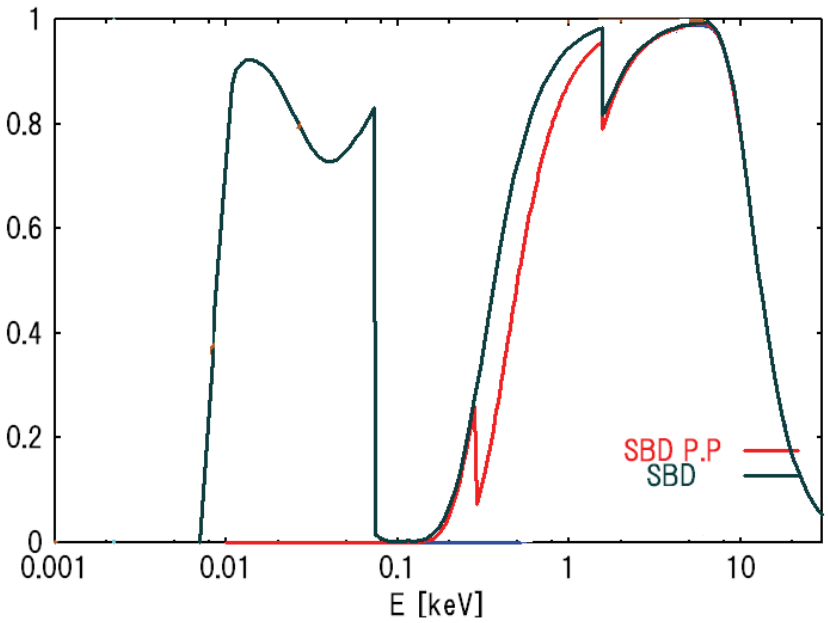

Fig. 2.6: Energy dependence of SBD sensitivity. The black line is sensitivity without filter and the red line is sensitivity with P.P. filter

elliptic arcs with axis lengths (a_1, a_2, a_3, a_4) and a common center position (R_c, Z_c). The current density in one quadrant of poloidal cross section is given by $j(R,Z) = j_0\{1-(R-R_c)^2/a_1^2-(Z-Z_c)^2/a_2^2\}^\alpha$. Its position, extent, and broadness (total of eight parameters) are fitted by adjusting these parameters to the magnetic measurements. RTFIT [68] is a filament current code that calculates the inboard and the outboard LCFS positions and the magnetic axis position. In this code, plasma is represented by one current filament, whose coordinates are free parameters. The QUEST numerical calculation system has been developed to draw approximate magnetic flux surfaces [68]. The vacuum magnetic field is calculated from currents in the external coils. The plasma current is assumed to flow inside a circular cross section boundary with a parabolic current density profile.

2.4 Heating and current drive systems

The following RF systems are available for use on QUEST.

- 2.45 GHz, 200kW
- 8.2 GHz, 200kW
- 8.56 GHz, 250kW
- 28 GHz, 600kW

The 8.2 GHz system is a CW system, and is used for long-pulse experiments. A traveling wave with adjustable polarization is excited and can be steered using a phased array antenna (Fig. 2.7).

The cutoff densities for 8.2 GHz and 28 GHz are $8.3\times10^{17}\,\mathrm{m}^{-3}$ and $9.7\times10^{18}\,\mathrm{m}^{-3}$, respectively. Second harmonic EC resonance is used for the 28 GHz experiment.

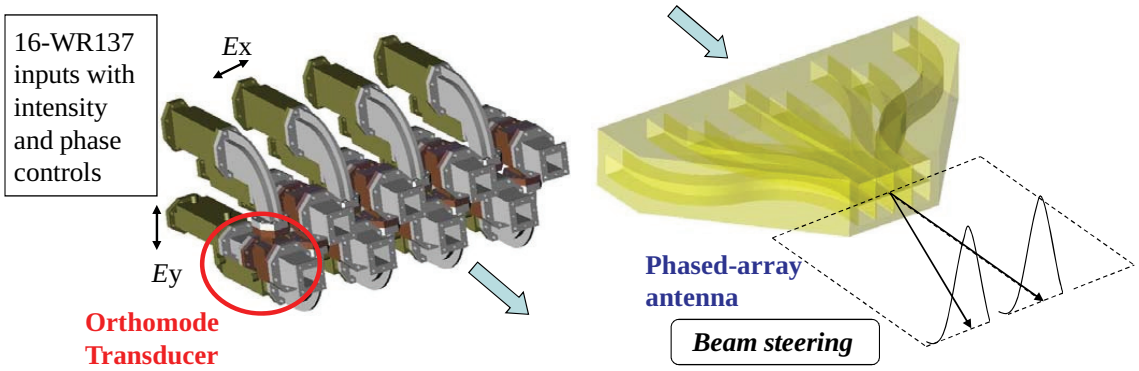

Fig. 2.7: Phased array antenna used on QUEST [69].

The wave of 2.45 – 28 GHz are electron cyclotron wave range for $B_T = 0.13 - -0.25\,T$, that is magnetic field strength of QUEST device. The ECW is absorbed by electron cyclotron

damping by electrons that satisfy the resonance condition [70]

$$\omega - k_{\parallel} v_{\parallel} - \frac{n\Omega_e}{\gamma} = 0 \tag{2.2}$$

$$n = \pm 1, \pm 2, ... \tag{2.3}$$

$$\gamma = \frac{1}{\sqrt{1 - v^2/c^2}}. \tag{2.4}$$

The EBW was first introduced in 1958 [71], and there are many studies on the physics and applications since then [72–76]. The EBW satisfies the following dispersion relation

$$\varepsilon(\omega, \boldsymbol{k}) = 1 + 2\frac{\omega_p}{k v_t} 2 \left[1 + \sum \xi_0 Z(\zeta) e^{-\lambda} I_n(\lambda)\right]. \tag{2.5}$$

It is an electrostatic wave and its wavelength is of the order of the electron gyroradius [77]. In the region where $k_\perp \rho$ is small, the EBW can couple to the X-mode, and mode conversion between the two modes is possible. The two possible conversion processes are X-mode to Bernstein mode (X-B) conversion and O-mode via X-mode to Bernstein mode (O-X-B) conversion. The O-X-B conversion is expected on QUEST. The O-mode launched from the antenna located on the low-field side is converted to the X-mode at the cutoff layer, and the X-mode propagating back to the low-field side is converted to the EBW near the upper hybrid resonance layer. Typical spatial profiles of relevant frequencies across the plasma midplane is shown in Fig. 2.8. The conversion efficiency from the O-mode to the X-mode is [78]

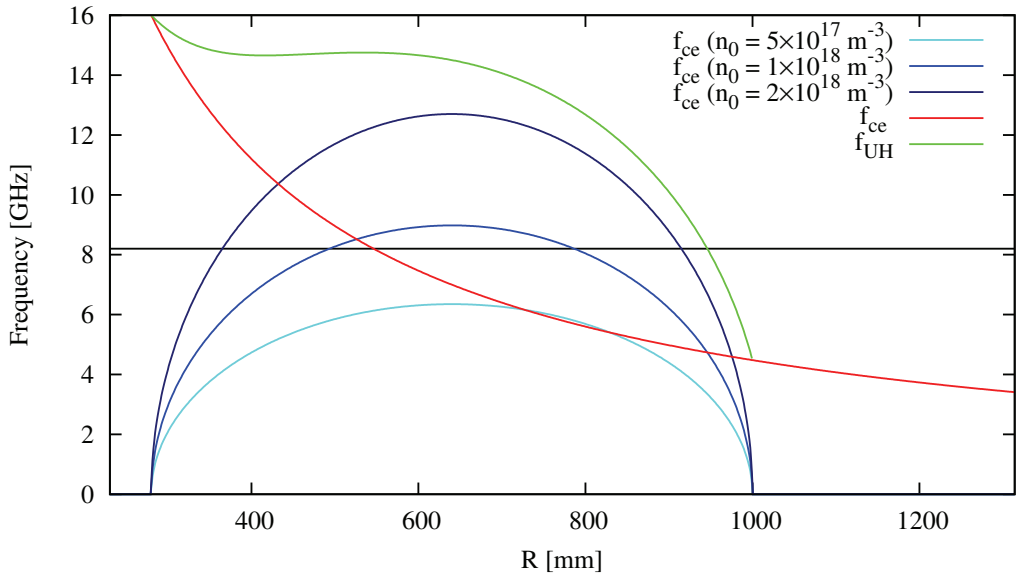

Fig. 2.8: Frequency diagram for the QUEST experiment ($B_{\mathrm{T}} = 0.25$ T at $R = 650$ mm).

$$T(N_{\parallel}, N_{\perp}) = \exp\left\{-\pi k_0 L_n \sqrt{\frac{Y}{2}} \left[2(1+Y)(N_{\parallel,\mathrm{opt}} - N_{\parallel})^2 + N_{\perp}^2\right]\right\}. \tag{2.6}$$

$N_{\parallel}$ and $N_{\perp}$ are refractive indices in the parallel and perpendicular directions to the magnetic field, k_0 is the wave number of the incident RF wave in free space, and Y is the normalized

cyclotron frequency

$$Y = \frac{\omega_c}{\omega_0}. \tag{2.7}$$

$L_{\rm n}$ is the density scale length

$$L_n = \frac{n_{\rm e}}{\frac{\partial n_{\rm e}}{\partial r}}. \tag{2.8}$$

$N_{\parallel,\rm opt}$ is the optimum refractive index,

$$N_{\parallel,\rm opt} = \frac{Y}{1+Y}. \tag{2.9}$$

The conversion efficiency of the X-mode to the EBW is

$$C = 4e^{-\pi\eta}(1-e^{-\pi\eta})\cos^2\left(\frac{\phi}{2}+\theta\right), \tag{2.10}$$

$$\eta = \frac{\omega_{\rm ce}L_n}{c}\frac{\alpha}{\sqrt{\alpha^2+2(L_n/L_B)}}\left[\frac{\sqrt{1+\alpha^2}-1}{\alpha^2+(L_n/L_B)\sqrt{1+\alpha^2}}\right], \tag{2.11}$$

where $\alpha = \omega_{\rm p}/\omega_{\rm ce}$ at the upper hybrid layer. The density scale length $L_{\rm n}$ and the magnetic field scale length $L_{\rm B}$ are evaluated at the upper hybrid layer. In the limit $L_{\rm B} \gg L_{\rm n}$

$$\eta \approx \frac{\omega_{\rm ce}L_n}{c\alpha}\left[\sqrt{1+\alpha^2}-1\right]^{1/2}. \tag{2.12}$$

ECW and EBW rays and absorption profiles for a typical QUEST plasma are calculated using a ray trace code [79–81].

Chapter 3

Thomson scattering

3.1 Principle of Thomson scattering

Thomson scattering [82] is the elastic scattering of photons by electrons. In the non-relativistic limit, the radiated power per solid angle from a particle with charge q and acceleration $\dot{\boldsymbol{v}}$ is given in the dipole approximation as

$$\frac{dP}{d\Omega} = \frac{q^2}{16\pi^2\varepsilon_0 c^3}|\dot{\boldsymbol{v}}|^2 \sin^2\Theta, \tag{3.1}$$

where Θ is the angle between the acceleration vector and the scattering vector, ε_0 is the permittivity of free space, and c is the speed of light.

The Poynting vector is

$$\boldsymbol{S}\frac{1}{\mu_0}\boldsymbol{E}\times\boldsymbol{B}, \tag{3.2}$$

Considering Poynting vector of laser, electric field is

$$\boldsymbol{E} = \boldsymbol{E}_0 \sin(\boldsymbol{k}_\mathrm{i}\cdot\boldsymbol{r} - \omega t) \tag{3.3}$$

The average energy flow of an electromagnetic wave per unit time is expressed by the average of the Poynting vector,

$$\bar{S_\mathrm{L}} = \frac{1}{\mu_0}\langle \boldsymbol{E}\times\boldsymbol{B}\rangle = \frac{1}{2\mu_0}\boldsymbol{E}_0\times\boldsymbol{B}_0 = \frac{1}{2}\sqrt{\frac{\mu_0}{\varepsilon_0}}|\boldsymbol{E}_0|^2\frac{\boldsymbol{k}_\mathrm{i}}{|\boldsymbol{k}_\mathrm{i}|}. \tag{3.4}$$

The intensity of the Laser light is equal to the absolute value of the Poynting vector,

$$I \quad = |\bar{S_\mathrm{L}}| \quad = \frac{1}{2\Omega_0}\,|\boldsymbol{E_0}\,[\mathrm{V/m}]|^2 \ \ [\mathrm{W/m^2}], \tag{3.5}$$

$$\Omega_0 \quad = \sqrt{\tfrac{\varepsilon_0}{\mu_0}} \quad = 337\ [\Omega]. \tag{3.6}$$

A particle with mass m is accelerated by the electric field of laser,

$$\dot{\boldsymbol{v}} = \frac{q}{m}\boldsymbol{E}. \tag{3.7}$$

Since wave scattering by ions is negligible because of the inverse mass dependence, so only scattering by electrons needs to be considered. The electron mass m_e and charge e are substituted. Eq. (3.1) is rewritten as follows using the Poynting vector S_L,

$$\frac{dP}{d\Omega} = r_\mathrm{e}^2 c\varepsilon_0 |\boldsymbol{E}|^2 \sin^2\Theta = S_\mathrm{L} r_\mathrm{e}^2 \sin^2\Theta = S_\mathrm{L}\left(\frac{d\sigma}{d\Omega}\right)^T, \tag{3.8}$$

$$S_\mathrm{L} = \frac{1}{\mu_0}|\boldsymbol{E}\times\boldsymbol{B}| = c\varepsilon_0|\boldsymbol{E}|^2, \tag{3.9}$$

$$\left(\frac{d\sigma}{d\Omega}\right)^T = r_\mathrm{e}^2\sin^2\Theta. \tag{3.10}$$

r_e is classical electron radius,

$$r_\mathrm{e} \equiv \frac{e^2}{4\pi\varepsilon_0 m_\mathrm{e} c^2}. \tag{3.11}$$

The total Thomson scattering cross section is obtain by integration over the whole solid angle Ω

$$\sigma^T = \frac{8\pi}{3} r_\mathrm{e}^2, \tag{3.12}$$

which is a physical constant.

Scattering from each single electrons in the plasma occur with different phases of particles. When the phase differences are uncorrelated, the scattered powers from different electrons can be summed to give the total scattered power in the far field. This condition is satisfied when the following condition is satisfied,

$$\alpha = \frac{1}{k\lambda_\mathrm{D}} < 1, \tag{3.13}$$

where $\mathbf{k} = |\mathbf{k}_\mathrm{s} - \mathbf{k}_\mathrm{i}|$, λ_D is the Debye length, $\mathbf{k}_\mathrm{i}$ and $\mathbf{k}_\mathrm{s}$ are the wavevectors of the incident wave and scattered wave, respectively. Since $k_\mathrm{i} \sim k_\mathrm{s}$, $k \sim 2k_\mathrm{i}\sin(\theta/2)$ where θ is the angle between the incident and the scattered wavevectors (Fig. 3.1). The condition (3.13) can be rewritten as

$$\alpha = \frac{1}{\lambda_\mathrm{D}}\frac{\lambda_\mathrm{i}}{4\pi\sin(\theta/2)} < 1. \tag{3.14}$$

This condition is satisfied in QUEST plasmas.

The spectrum of incoherent Thomson scattering contains information on the electron distribution function. The frequency of the light scattered from an electron at rest is identical to the incident frequency. However, an electron in motion feels a Doppler-shifted incident wave, and radiates a scattered wave at a Doppler-shifted frequency. The frequency of the scattered wave is

$$\omega_\mathrm{s} = \omega_\mathrm{i} + \ \boldsymbol{k}\cdot\boldsymbol{v} = \omega_\mathrm{i} + (\ \boldsymbol{k}_\mathrm{s} - \boldsymbol{k}_\mathrm{i})\cdot\boldsymbol{v} = \omega_\mathrm{i}\left(\frac{1-\boldsymbol{k}_\mathrm{i}\cdot\boldsymbol{v}\ /c}{1-\boldsymbol{k}_\mathrm{s}\cdot\boldsymbol{v}\ /c}\right). \tag{3.15}$$

The optical system of a Thomson scattering system can collect only a limited fraction of the scattered light. The collection optics must be designed to maximize the collection efficiency,

$$P = P_\mathrm{i} r_\mathrm{e}^2 n_\mathrm{e} L S(T_\mathrm{e}, \theta, \lambda). \tag{3.16}$$

Here, n_e is the electron density, L is the length of the scattering volume, P_i is the energy of the incident laser pulse, When the electron temperature is low, $S(T_\mathrm{e}, \theta, \lambda)$ is represented by

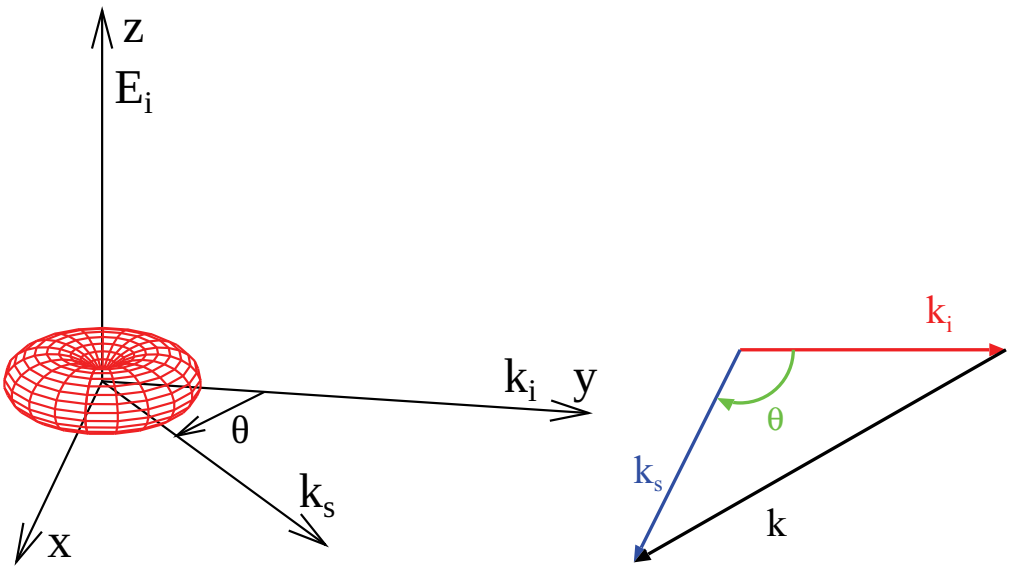

Fig. 3.1: Geometry of scattering.

the nonrelativistic spectral function $S_{\mathrm{N}}(T_{\mathrm{e}}, \theta, \lambda)$,

$$S_{\mathrm{N}}(T_{\mathrm{e}}, \theta, \lambda) = \frac{c}{2\sqrt{2\pi}\lambda_0 \sin(\theta/2)} \sqrt{\frac{m_0}{T_{\mathrm{e}}}} \exp\left[\frac{-m_0 c^2 (\lambda - \lambda_0)^2}{8 T_{\mathrm{e}} \lambda_0^2 \sin^2(\theta/2)}\right], \tag{3.17}$$

$$= \frac{\sqrt{\alpha}}{2\sqrt{\pi}\lambda_0 \sin(\theta/2)} \exp\left[-\frac{\alpha}{4\sin^2(\theta/2)}\epsilon^2\right], \tag{3.18}$$

$$\epsilon = \frac{\lambda - \lambda_0}{\lambda_0}, \tag{3.19}$$

$$\alpha = \frac{m_0 c^2}{2T_{\mathrm{e}}}. \tag{3.20}$$

When the electron temperature is high, $S_{\mathrm{N}}(T_{\mathrm{e}}, \theta, \lambda)$ should be replaced by the relativistic spectral function $S_{\mathrm{R}}(T_{\mathrm{e}}, \theta, \lambda)$,

$$S_{\mathrm{R}} = S_{\mathrm{N}}\left[1 - \frac{7}{2}\epsilon + \frac{\alpha}{4\sin^2(\theta/2)}\epsilon^3\right], \tag{3.21}$$

This is the first order approximation given by Sheffield [83].

The second order approximate relativistic function is [84]

$$S_{\mathrm{R}} = S_{\mathrm{N}}\left[1 - \frac{7}{2}\epsilon + \frac{\alpha}{4\sin^2(\theta/2)}\epsilon^3\right] - \frac{1}{8\alpha}\left[\frac{39}{4} - 5\cos(\theta)\right] + \frac{1}{8}\left[29 + \frac{5}{2\sin^2(\theta/2)}\right]\epsilon^2$$
$$- \left[28 - \frac{1}{2\sin^2(\theta/2)}\right]\frac{\alpha}{32\sin^2(\theta/2)}\epsilon^4 + \frac{\alpha^2}{32\sin^4(\theta/2)}\epsilon^6. \tag{3.22}$$

The signal intensity of Thomson scattered light detected by the i-th APD of the polychromator is expressed as

$$I_{\mathrm{i}} = n_{\mathrm{e}} L P_{\mathrm{i}} \Delta\Omega G C_{\mathrm{T}} \int f_{\mathrm{i}}(\lambda) S_{\mathrm{R}}(T_{\mathrm{e}}, \theta, \lambda) \frac{d\sigma}{d\Omega} d\lambda. \tag{3.23}$$

Here, $\Delta\Omega$ is the observation solid angle, G is the gain of the second amplifier, C_{T} is the total transmission coefficient of the incidence and collection optics, $f_{\mathrm{i}}(\lambda)$ is the spectral responsivity function for each channel described in Section 4.1, S is the form factor describing the shape of the spectral distribution, and σ is the Thomson scattering cross section.

The electron temperature and density are calculated by the following procedure. The measured signal is integrated over a duration which includes the scattered pulse, and fitted to Eq. (3.23), which is a function of T_{e}, n_{e}, and the spectral responsivity f_{i} for the corresponding channel. The error of the integrated value for each wavelength channel is used as the weight for fitting to a Maxwell distribution function. The IDL CURVEFIT function, which adopts a gradient-expansion algorithm, is used to compute the non-linear least squares fit. In order to confirm the goodness of fit, deviations of the signal from the fitted value are analyzed. In addition, the same measurements were repeated for several similar discharges. Unfortunately, because the reproducibility from shot to shot is not perfect, the errors for T_{e} and n_{e} are estimated from the deviation from the fitted value using several discharges. These errors could be overestimated values.

The number of photons incident on a fiber optic cable is

$$N = \frac{P_{\mathrm{i}}}{hc/\lambda} n_{\mathrm{e}} \cdot L \cdot \sigma_{\mathrm{T}} \Delta\Omega \cdot C_{\mathrm{T}}, \tag{3.24}$$

where P is energy of the laser, c is the velocity of light, λ is the wavelength of the laser light, h is the Planck constant, n_{e} is the electron density, L is the length of the scattering volume along the laser, σ_{T} is the Thomson scattering cross section, $\Delta\Omega$ is the detection solid angle, and C_{T} is the transmission efficiency of the detection system, respectively.

3.2 Description of the QUEST Thomson scattering system

The QUEST Thomson scattering system consists of three parts: the incidence optics, the light collection optics, and the spectroscopic system. Each part consists of many components as listed below.

1. Laser and incidence optics
   laser, focusing lens, input and output Brewster windows, beam dump
2. Light collection optics
   spherical mirror, optical fiber
3. Spectroscopic system
   polychromator, detector, fast digitizing oscilloscope

3.2.1 Laser

The intensity of incoherent Thomson scattering is proportional to the Thomson scattering cross section, which is very small. Therefore, a very intense light source is required to obtain a detectable signal. On the other hand, the noise will generally increase with the pulse length, because the signal integration time should be longer than the laser pulse length. Hence, both high power and high energy are required for the laser. This is why Thomson scattering measurements almost always use intense pulsed lasers.

In the QUEST Thomson scattering system, a 10 Hz, 1064 nm Nd:YAG laser is used. The laser is operated in the Q-switched mode, providing a laser pulse length of about 7 ns. An advantage of using an infrared light around 1 μm, instead of a visible light, is that the plasma radiation, which becomes the background noise, is weak in this spectral region. The Continuum Power Lite 8010 laser, with its main specifications shown in Table 3.2.1, is used.

Parameter	Value
Wavelength	1064 [nm]
Repetition Rate	10 [Hz]
Energy	1650 [mJ]
Pulse Duration	$6-8$ [ns]
Beam Diameter	≤ 9 [mm]
Divergence	0.45 [mrad]
Energy stability	± 2.5 [%]
Pointing stability	± 30 [μrad]

Table. 3.1: Laser specifications.

For safety, the laser is interlocked with the door monitor interlock of QUEST. The circuit becomes active in the "External mode" of the laser firmware. The interlock controls the internal shutter. In the "External mode", the laser can be operated from the control box in the QUEST control room. During QUEST operation, the user switches from the "Internal mode" to the "External mode".

The laser system has the following states: "Stop", "Standby", "Flash lamp", "Q-switch", and "Shutter". The laser sequence proceeds in this order. Each mode button is displayed on the control application window of the laser control PC (3.3), which is located near the laser.

The laser control box in the QUEST control room has "Standby", "Flash lamp", "Q-switch", and "Shutter", and the "Stop" state is realized by turning off all of these switches.

- "Stop": beginning state just after turning on the power unit.
- "Standby": power is supplied to the laser unit.
- "Flash": the flash lamp is started.
- "Q-switch": Q-switch operation is started.
- "Shutter": the internal shutter of the laser is opened.

The laser operation sequence is as follows:

1. The circuit breaker and the safety key of the power unit, and the cooling water system are turned on.
2. The laser is set to be "Standby" mode.
3. Laser warm-up (about one hour).
4. "Flash lamp" is turned on.
5. The flash lamp heats the laser rod to 35°C for the oscillator rod and 40°C for the amplifier rod.

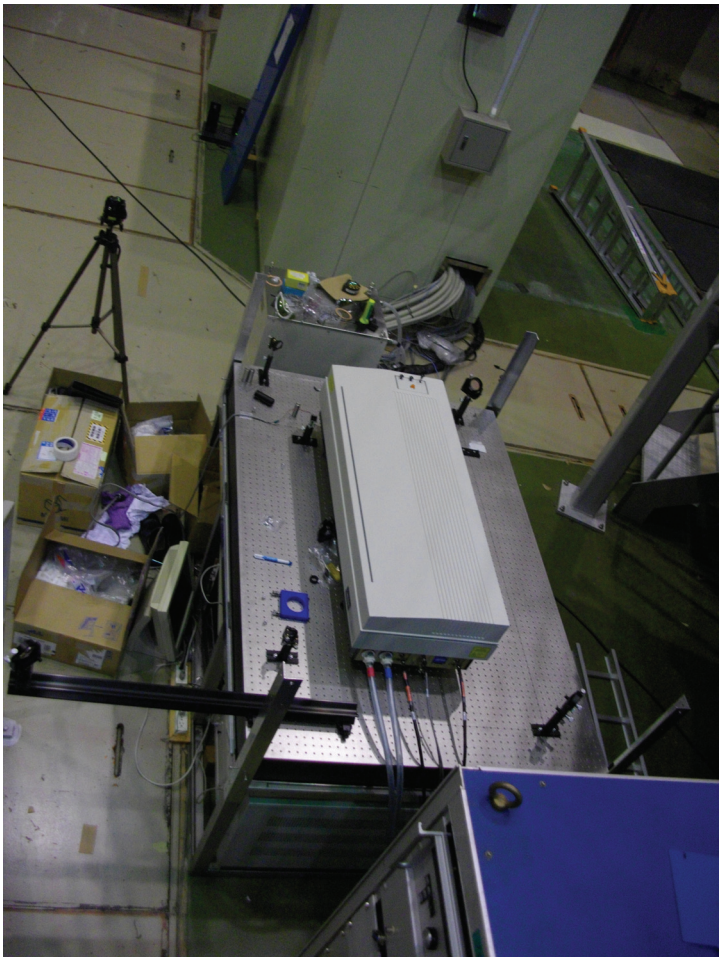

Fig. 3.2: Photograph of the Nd:YAG laser used on QUEST.

Fig. 3.3: Laser control application [85] window.

6. Warming of the laser rod (more than ten minutes).
7. While the discharge repetition time is less than 30 minutes, the flash lamp is always in the active sate.
8. About 30–60 seconds before the start of a QUEST discharge, “Q-switch” is turned on.
9. Very shortly afterward, the “Shutter” mode is turned on.

3.2.2 Incidence optics

Arrangement of the main components of the QUEST Thomson scattering system is shown in Fig. 3.4. The magenta line indicates the optical path of the laser light. The aqua line indicates the scattered light. Two green circles indicate the inboard and outboard limits of Thomson scattering spatial coverage.

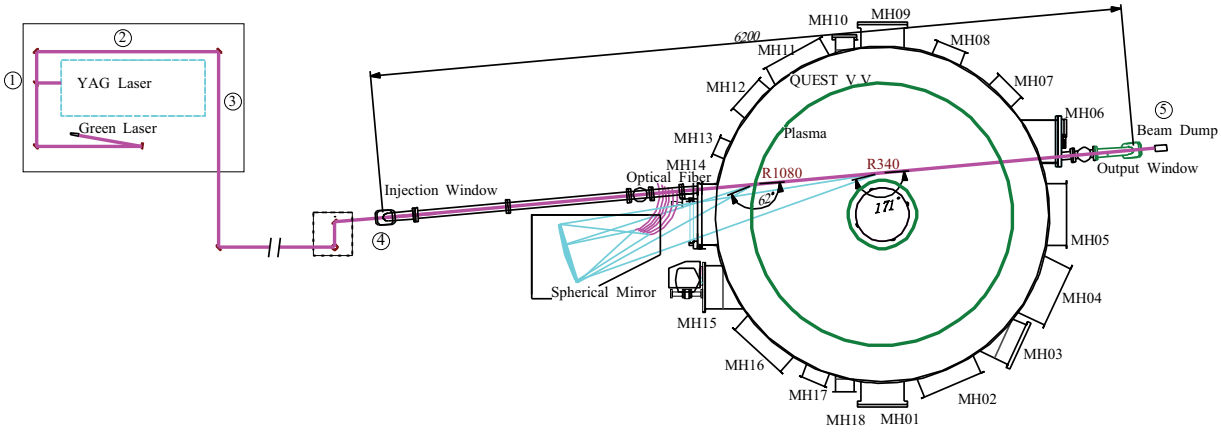

Fig. 3.4: Arrangement of the main components of the QUEST Thomson scattering system.

In order to collect the scattered light efficiently, the laser beam is focused inside the plasma. Before entering the vacuum vessel, the laser light is focused by a convex lens whose focal length is 3000 mm. The convergence of the laser light was confirmed using burn patterns on burn papers (Figs. 3.5, 3.6).

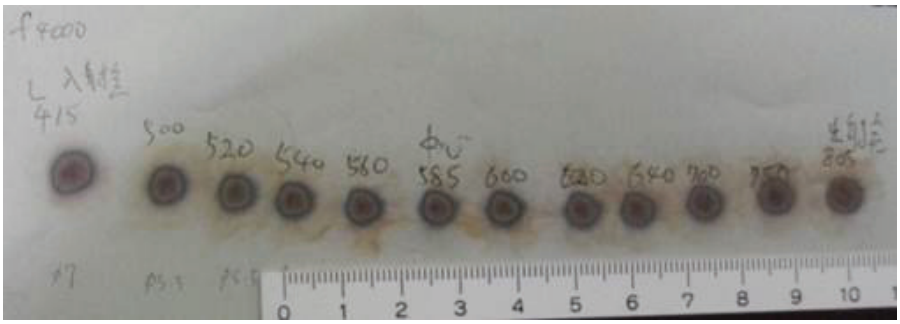

Fig. 3.5: Photograph of burn patterns.

Brewster’s vacuum windows are used to reduce the stray light and to achieve high transmission of the incident laser beam (Fig. 3.7). When light travels from one medium to another

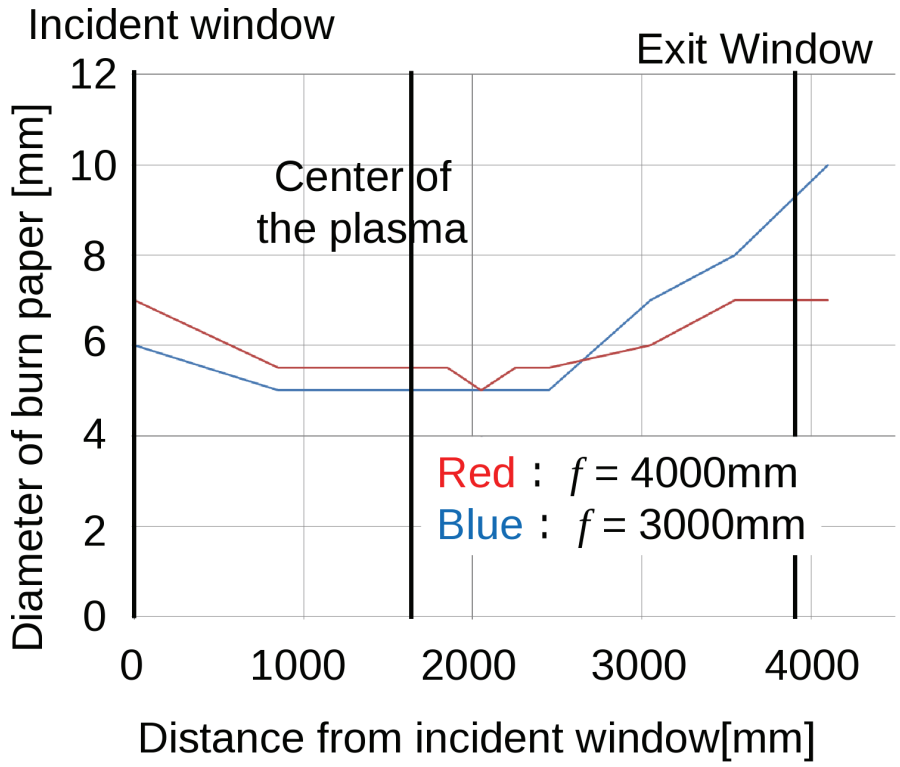

Fig. 3.6: Diameter of burn pattern as a function of distance from the incidence window.

medium with different refractive indices, a fraction of the incident light is reflected at the medium boundary. However, at a particular angle of incidence, light with the electric field polarized in the same plane as the incident ray and the surface normal (p-polarization) is not reflected. This angle of incidence is called the Brewster's angle. This condition and Snell's law are

$$\theta_1 + \theta_2 = \frac{\pi}{2}, \tag{3.25}$$

$$n_1 \sin\theta_1 = n_2 \sin\theta_2, \tag{3.26}$$

where θ_1 is the angle of incidence and θ_2 is the angle of refraction. The Brewster's angle $\theta_B = \theta_1$, where no p-polarized light is reflected, is

$$\theta_B = \tan^{-1}\left(\frac{n_2}{n_1}\right). \tag{3.27}$$

For a BK7 window ($n_2 = 1.507$ for Nd:YAG laser), the Brewster's angle is approximately 56.4 ° from the normal.

A beam dump is necessary to absorb the laser light which was not scattered, since it can be a source of stray light. The incident light cannot be reflected back towards the laser without hitting the graphite plate many times. However, since the beam dump is not a perfect absorber, it can be a dominant source of stray light.

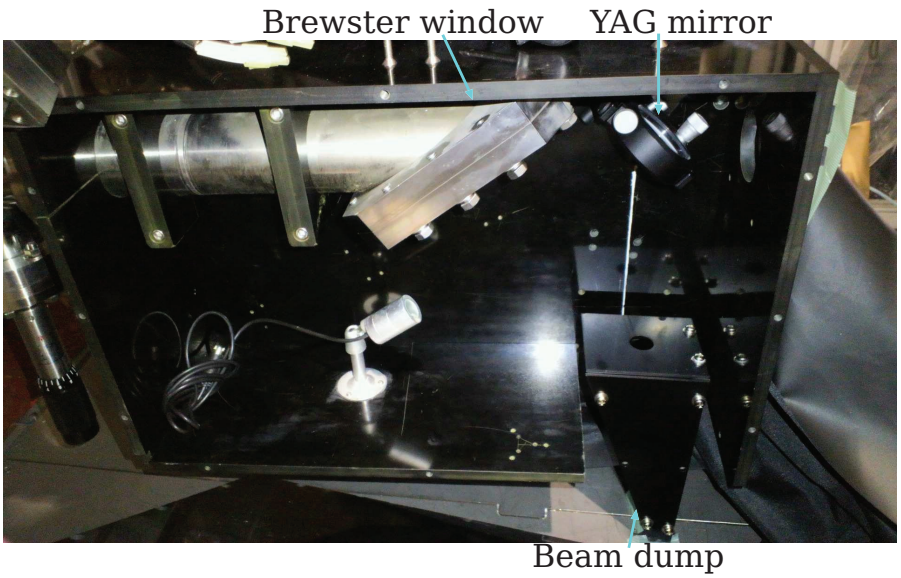

Fig. 3.7: Photograph of Brewster's window and the beam dump.

Transmission losses from the laser to the beam dump were measured. The measured powers normalized by the laser output power are shown in Fig. 3.8. Assuming that the loss from the first Brewster's window to the center of the plasma is equal to that from the center of the plasma to the beam dump, the transmission loss from the laser to the plasma center is 6% .

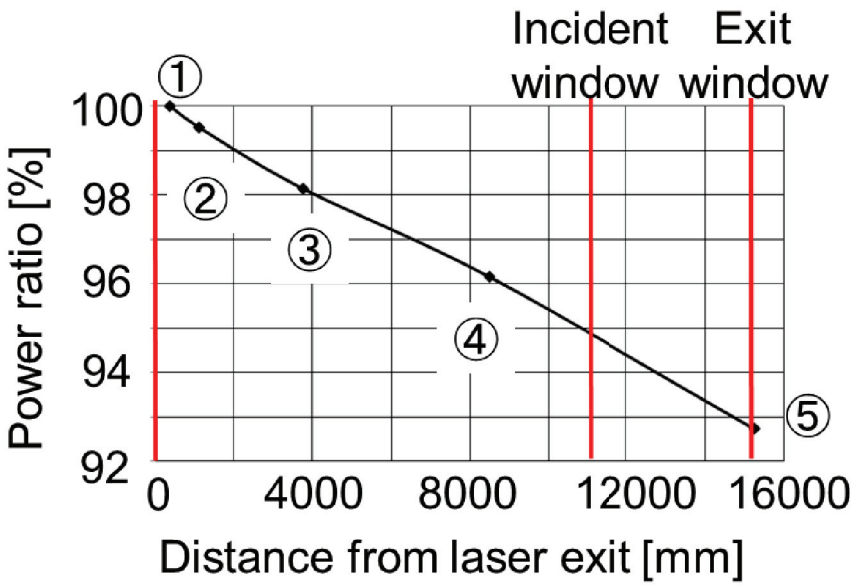

Fig. 3.8: Power relative to the incident laser power as a function of the distance from the laser.

3.2.3 Light collection optics

The configuration of the light collection optics is shown in Figs. 3.9 and 3.10.

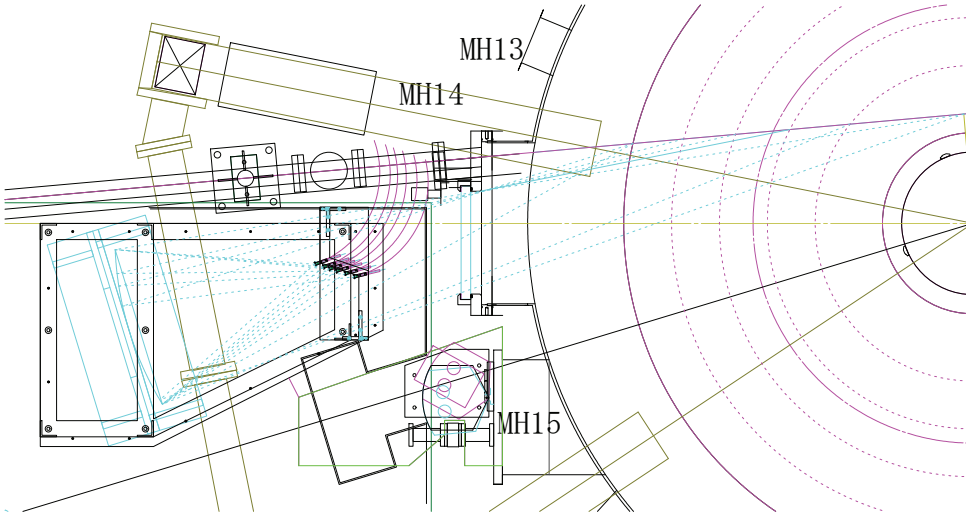

Fig. 3.9: Plan view of the collection optics.

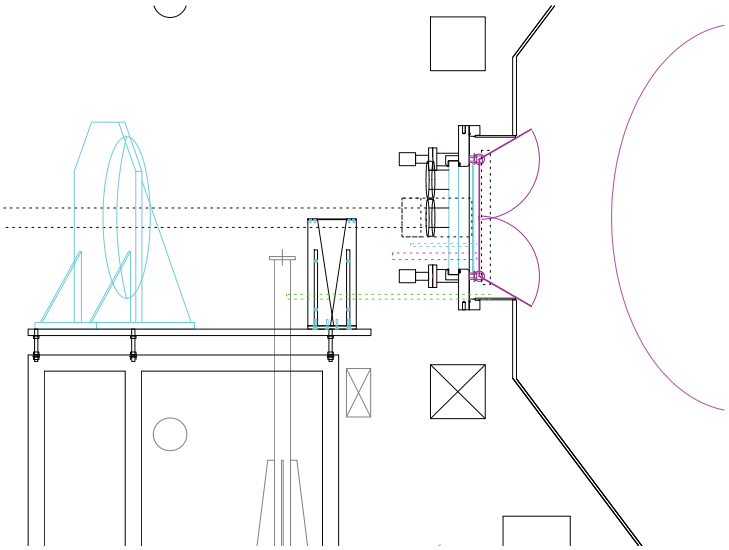

Fig. 3.10: Side view of the collection optics.

The scattered light passes through the collection window, focused by the collection mirror onto fiber optic cables, and are transmitted to the spectrometers (Figs. 3.13 and 3.12).

The collection window becomes coated by metal impurity deposited during plasma operation, and the transmissivity deteriorates as shown in Fig. 3.11. The metal deposit must be removed to recover the transmissivity.

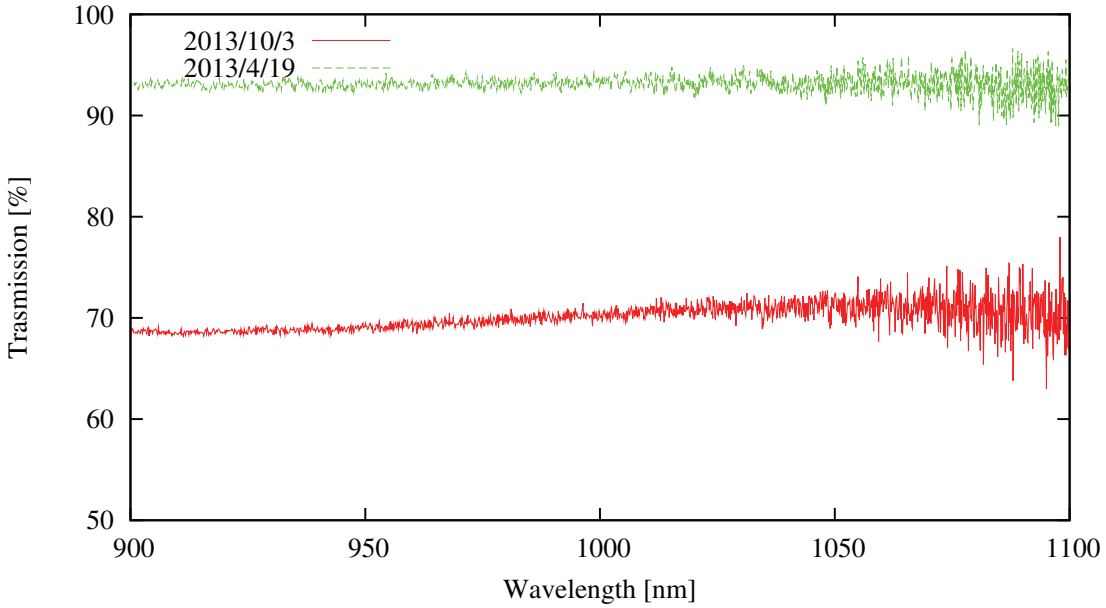

Fig. 3.11: Transmissivity of the window, measured before an experimental campaign on April 19, 2013 (green curve) and after the campaign on October 3, 2013 (red curve).

The collection mirror is a spherical mirror of radius 500 mm, with a radius of curvature of 1000 mm and a focal length of 500 mm. The surface of the mirror is gold plated (Figs. 3.12).

Fig. 3.12: Collection mirror.

The input end of the fiber optic cables are held by a fiber holder at the focal line of the collection mirror. The fiber holder is aligned using the green laser with a target plate positioned inside the QUEST vacuum vessel.

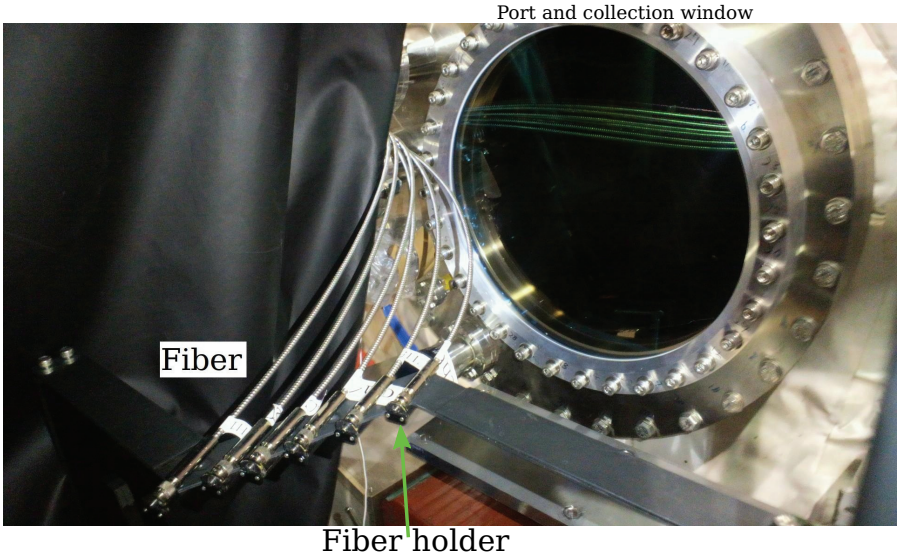

Fig. 3.13: Photograph of fiber holder, fiber and collection window.

Optical fibers (APC2000N, Fiberguide, 2 mm core diameter) with a large numerical aperture (NA) are used to collect the scattered light imaged by the spherical mirror with a large acceptance angle of 22° [86]. The NA is expressed as

$$NA = n\sin(\theta) \tag{3.28}$$

$$NA = \sqrt{n_1^2 - n_2^2}, \tag{3.29}$$

where n_1 and n_2 are the refractive indices of the fiber core and the clad. Although the maximum theoretical NA of this fiber is 0.37, this value is guaranteed only for a short fiber length (2 m). Guided rays close to the maximum acceptance angle are selectively attenuated by the cladding material, so the NA is reduced somewhat over a distance longer than the guaranteed distance. The NA of the fiber was measured, and was confirmed to be sufficiently large.

3.2.4 Alignment

For alignment of the infrared laser, a continuous visible (green) laser with a wavelength of 532 nm, an output power of 5 mW, a divergence of 1.2 mrad, and a diameter of 2 mm was used. Table 3.2 shows the parameters of the six scattering volumes of the QUEST Thomson scattering system. The scattering volumes are distributed from major radius 340 mm to 1080 mm. The scattering angle is in the range 165 – 171°. The backward scattering configuration, in which the scattering length and the scattering intensity are larger than the perpendicular scattering configuration, is used. The scattering lengths are 18 – 53 mm, and the solid angles are 0.03 – 0.07 sr. The configuration of our collection optics is shown in Fig. 3.9 and Fig. 3.10.

Channel	Radius [mm]	Scattering angle [°]	Scattering length [mm]	Solid angle [sr]
S1	340	171	52.9	0.0282
S2	488	169	39.2	0.0365
S3	636	168	32.4	0.0430
S4	784	167	26.7	0.0506
S5	932	166	21.9	0.0597
S6	1080	165	17.7	0.0711

Table. 3.2: Parameters of QUEST Thomson scattering measurement volumes.

Figures 3.14 and Fig. 3.15 display the result of ray tracing calculation and the calculated intensity of the collected light, respectively. $L\Omega$ is the product of the scattering length L and the solid angle Ω. The values on the inboard side are higher than those on the outboard side. The value at the innermost point is lower because of shadowing by the collection window.

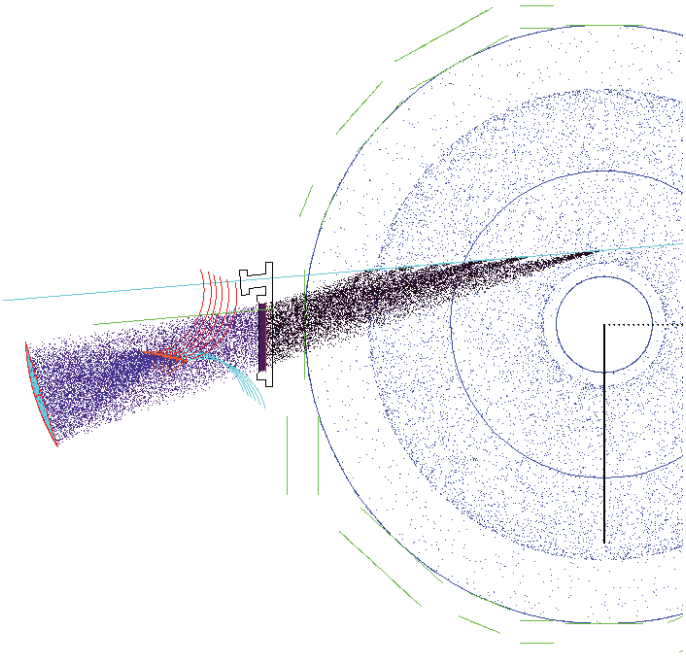

Fig. 3.14: Scattered rays from scattering volumes inside the plasma, and rays focused on the fiber entrance by the collection mirror.

3.2.5 Light detection

The scattered light is transported to the polychromator through fiber optic cables, divided into six different wavelength bands by interference filters and detected by avalanche photo-diodes (APDs). The light exiting the fiber spreads with the angle corresponding to the NA of the fiber (= 0.37). The light is collimated by an aspheric collimating lens,and is transferred to

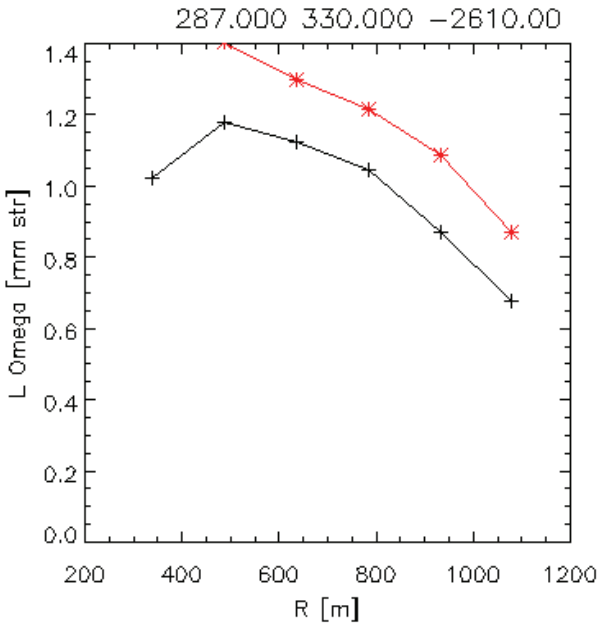

Fig. 3.15: Calculated $L\Omega$ as a function of major radius. Plus symbols are results of ray tracing, and asterisks include the effect of the collection mirror.

different filters by relay lenses. The light that is transmitted through each filter is focused onto an APD by a collection lens.

The interference filter is a multilayer thin-film optical device. The principle is the same as the Fabry-Perot interferometer. Common specifications of the filters at the incidence angle of 4° for use in collimated light are: peak transmission of more than 80 % within the pass band, blocking of $OD = 5$ (10^{-5} transmittance) at 1064.3 nm and out of band from 200 to 1100 nm, and average reflection of greater than 90 % from 450 to 1100 nm. OD is the optical density defined as $-\log_{10}(T)$, where T is the transmittance. If OD is small at 1064.3 nm, stray light may enter the detector, resulting in a spurious signal.

The relationship between the wavelength and energy of a photon is

$$E_{\text{photon}} = \frac{hc}{\lambda} = \frac{1.24}{\lambda\,[\mu\text{m}]}\,[\text{eV}]. \tag{3.30}$$

The photocurrent I_{photo} is given by the product of electronic charge q and the number of electrons generated per unit time n_{e},

$$I_{\text{photo}} = q \cdot n_{\text{e}}. \tag{3.31}$$

The incident energy flux is given by the product of the number of photons per second n_σ and the energy per photon $h\nu$,

$$P_{\text{opt}} = n_\sigma \cdot h\nu. \tag{3.32}$$

The quantum efficiency of a photo diode is defined as

$$\eta_{\text{Q}} = \frac{n_{\text{e}}}{n_\sigma} = \frac{I_{\text{photo}}/q}{P_{\text{opt}}/h\nu}. \tag{3.33}$$

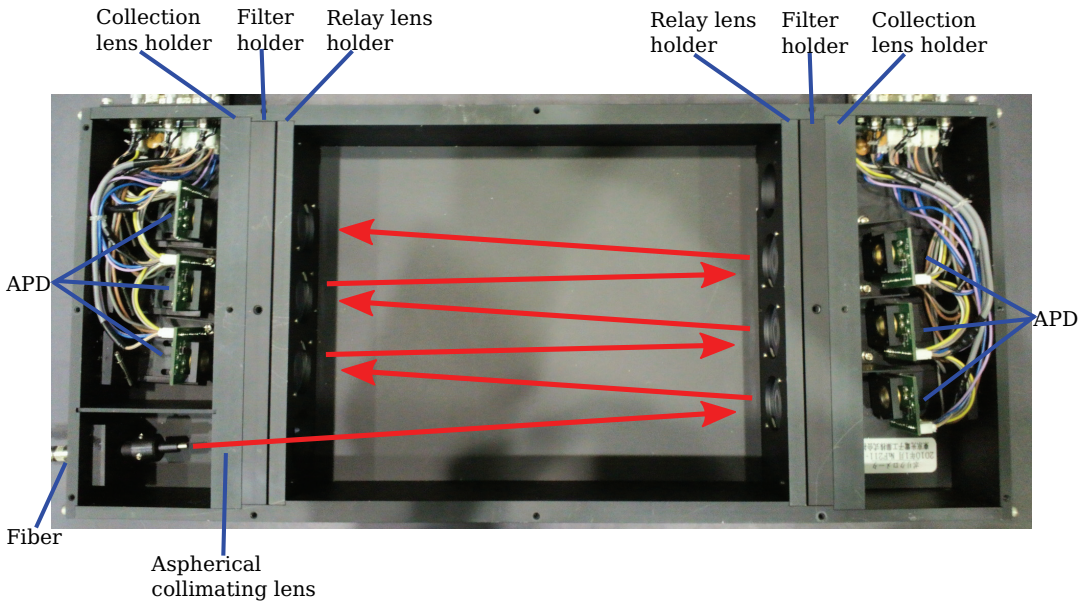

Fig. 3.16: Photograph of the polychromator with the top panel removed.

For fast detection of a weak light in the wavelength range of 200 to 1150 nm range, basic detector choices include Si photo-diode, Si PIN photo-diode, Si APD, and photomultiplier tube (PMT). APDs are widely used in instrumentation and aerospace field, providing a combination of high speed and high sensitivity, while standard PIN photo-diodes have high sensitivity [87]. PMTs have a fast response, but typical ranges of sensitive wavelength are shorter than 700 nm. When electron hole pairs are generated in the depletion layer of a photo-diode with a reverse voltage applied to the PN junction, the electrons drift towards the N+ side while the holes drift towards the P+ side due to the electric field [88]. If the reverse voltage is sufficiently high, some of the carriers which do not suffer collisions with the crystal lattice will gain a great deal of energy. When these high energy carriers collide with the crystal lattice, electron-hole pairs are newly generated. These electron-hole pairs then create additional electron-hole pairs in the manner. The QUEST Thomson scattering system uses Si-APD (S8890-30 Hamamatsu Photonics) with a sensitive diameter of 3 mm. The gain of an APD depends on the ambient temperature. Figure 3.17 shows the as a function of the reverse voltage at various temperatures.

The time evolution of the room temperature in the QUEST experimental hall is about 1°C during the experiment on a given day (Fig. 3.18). When the gain of the APD is 100, the gain decreases by about 5% for one degree rise in the ambient temperature. The relative sensitivities among different wavelength channels are calibrated using a standard light source, as described in the next Chapter.

3.3 Noise of electronics and back light

The photo-diode noise $i_{\rm n}$ consists of the thermal noise (or Johnson noise) $i_{\rm j}$ of a resistor, and the shot noises generated from the dark current ($i_{\rm D}$) and from the photocurrent ($i_{\rm L}$),

$$i_{\rm n} = \sqrt{i_{\rm j}^2 + i_{\rm D}^2 + i_{\rm L}^2}. \tag{3.34}$$

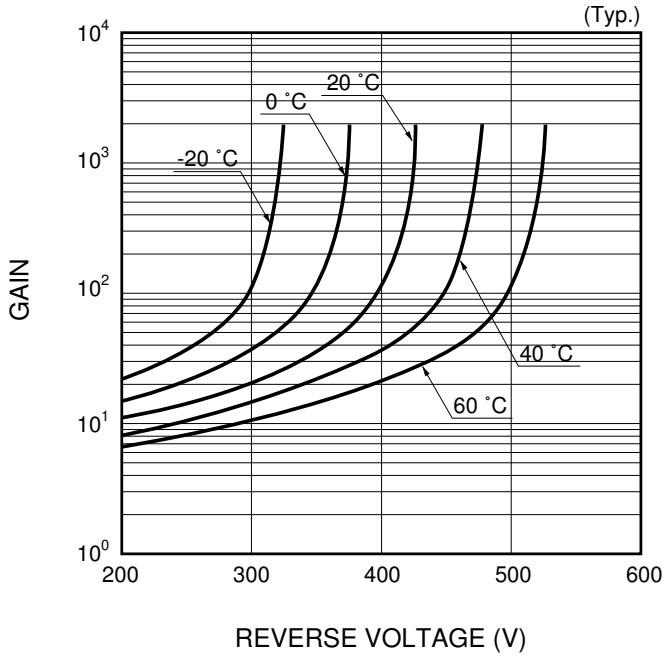

Fig. 3.17: Avalanche gain of the S8890 APD as a function of the reverse voltage at different temperatures [89].

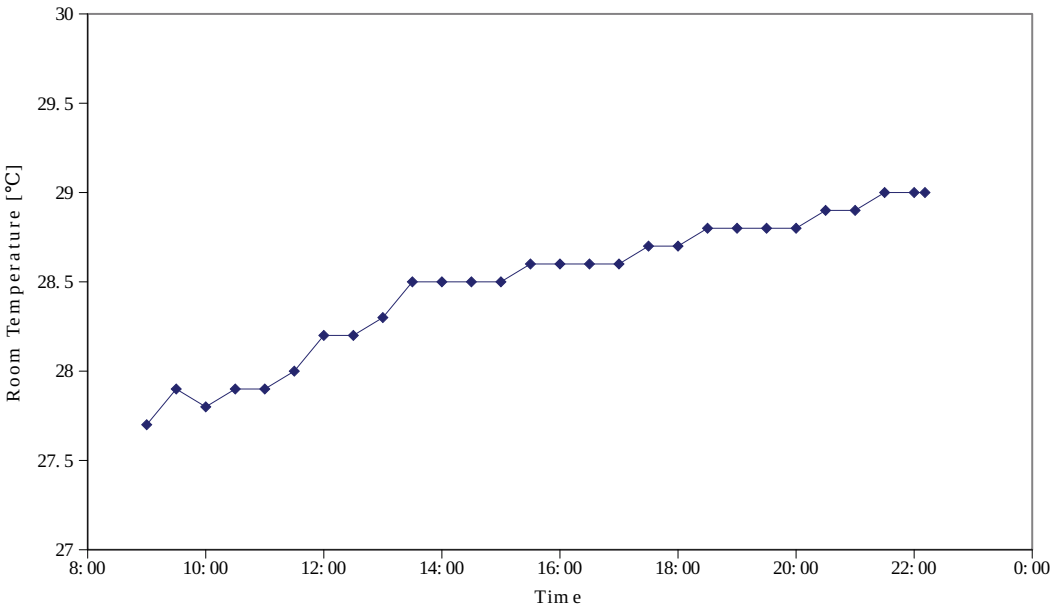

Fig. 3.18: Room temperature in the QUEST experimental hall. The experiment started at 10:30.

The thermal noise of a shunt resistance $R_{\rm sh}$ is given as

$$i_{\rm j} = \sqrt{\frac{4kTB}{R_{\rm sh}}}, \tag{3.35}$$

where B is the bandwidth of the measurement. There is always a dark current $I_{\rm D}$ when a bias voltage is applied. The shot noise $i_{\rm D}$ generated by the dark current is given by

$$i_{\rm D} = \sqrt{2eI_{\rm D}B}. \tag{3.36}$$

A photocurrent $I_{\rm L}$ is produced by the incident light, and the resultant noise $i_{\rm L}$ is given by

$$i_{\rm L} = \sqrt{2eI_{\rm L}B}. \tag{3.37}$$

The amplitudes of these noise sources are proportional to the square root of the measurement bandwidth B, so they are expressed in units of $\mathrm{A/Hz^{1/2}}$ and is called as the noise equivalent power (NEP). The plasma background light noises are composed of short time scale (μs) components arising from local fluctuations and long time scale (ms) components arising from macroscopic fluctuations.

All 6 wavelength channels of the polychromator are measured simultaneously using an 8-channel high-speed oscilloscope (YOKOGAWA DL7480 or DLM4058) with a sampling rate of 1 GHz (or 1.25GHz), and a band width of 500 MHz. Therefore, the goodness of fit to a Maxwell distribution function can be confirmed. In a sustained low density plasma, the signal to noise ratio is very low. The raw digitized signals from different laser pulses are accumulated. The peak time of the laser monitor signal is used for synchronization. There is an uncertainty in time during a plasma discharge of 0.05 second (0.5 laser pulse), because the laser timing is not synchronized with the QUEST plasma timing.

Chapter 4

Calibration and Analysis

4.1 Calibration of polychromator

For the calibration of polychromator, the monochromator, lens and chopper are used. Set up of the calibration is shown Fig. 4.1

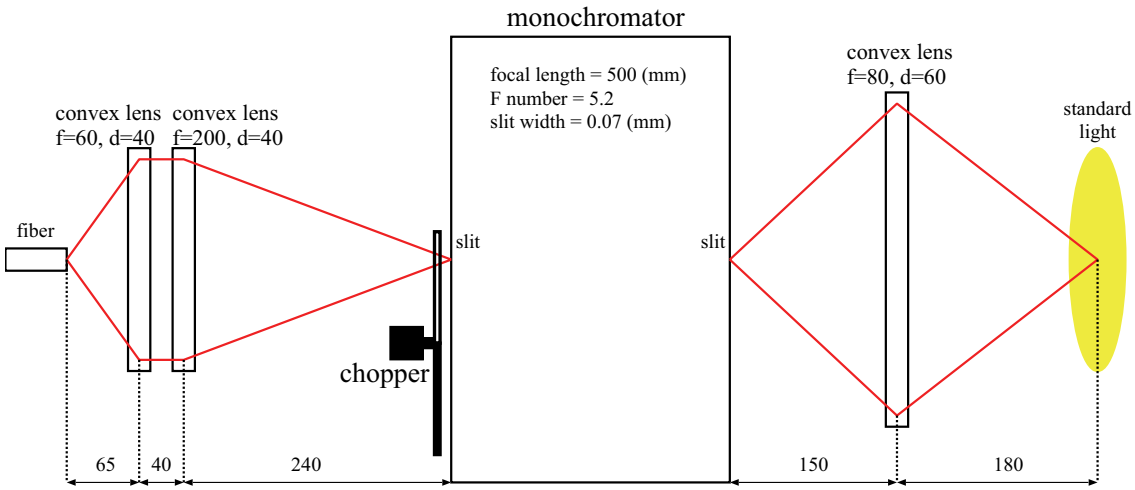

Fig. 4.1: Set-up of the monochromator for calibration of the polychromator. The parameters f and d are focal length and lens diameter in mm, respectively.

A standard light source and a monochromator were used for calibration of the polychromator used in the QUEST Thomson scattering system. A diffraction grating is used in this monochromator. The objective is to determine the spectral responsivity for each channel of the polychromator. The wavelength resolution of the monochromator must be high to preserve the accuracy of the wavelength sensitivity function of the filter. When the entrance or exist slit is relatively wide, the resolution is simply proportional to the slit width. In this case, the resolution $\Delta\lambda$ is expressed as

$$\Delta\lambda = \frac{d \cdot \cos\theta_{\mathrm{d}}}{kf}\Delta s, \tag{4.1}$$

where Δs is the slit width, d is the pitch of the grating, θ_{d} is the diffraction angle, f is the focal

length (twice the radius of curvature of the collection mirror) and k is the order of diffraction, respectively. As the slit width decreases, it approaches the following limit,

$$\Delta\lambda = kN, \tag{4.2}$$

where N is the number of grooves on the grating.

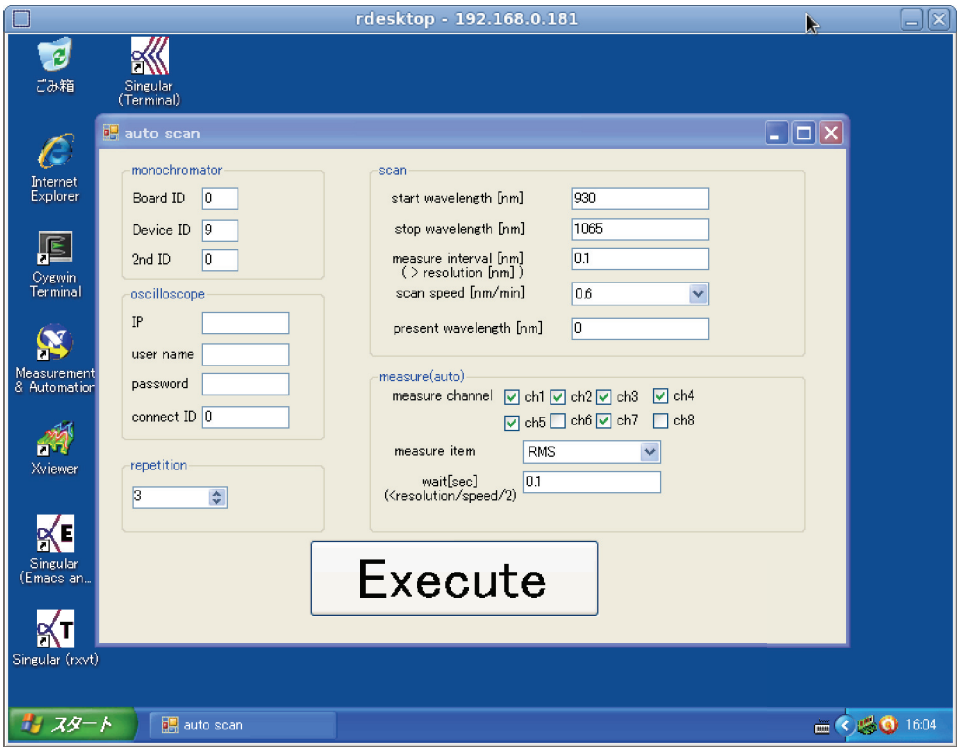

Fig. 4.2: Windows application for automatic calibration of the polychromator. The monochromator and the oscilloscope (data recorder) are controlled and the wavelength is scanned automatically.

The wavelength distribution of the standard light source approximately follows the black body spectrum,

$$I(T)d\lambda = \frac{2hc^2}{\lambda^5}\frac{1}{\exp(hc/\lambda kT) - 1}d\lambda. \tag{4.3}$$

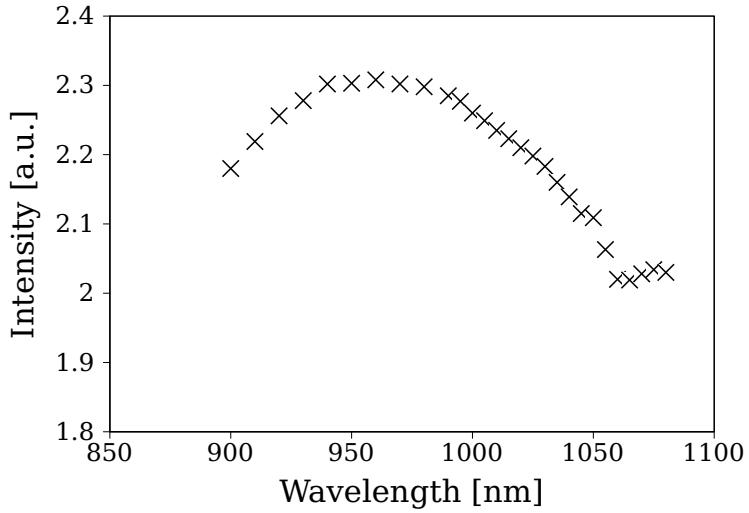

Fig. 4.3: Wavelength distribution of the standard light source measured at the fiber entrance (focal point).

The temperature of this standard lamp can be calculated by Wien's displacement law,

$$T\,[K] = \frac{2897768}{\lambda\,[\mu\mathrm{m}]}. \tag{4.4}$$

to be about 3100 [K] .

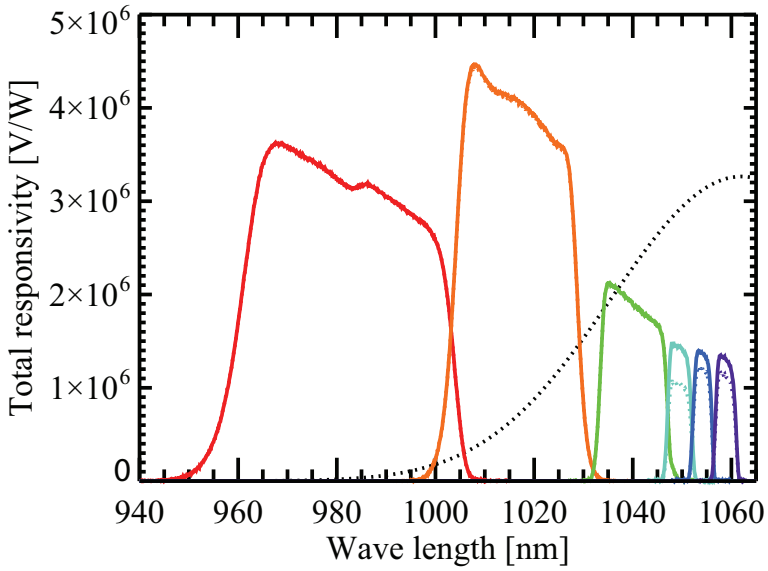

Fig. 4.4: Wavelength sensitivity of each filter.

The light exiting the monochromator is modulated at 500Hz by a chopper. Harmonic wavelengths are reduced by colored filters. The output voltage is measured at intervals of 0.1 nm. An automatic calibration system was developed to perform calibration efficiently. For

each wavelength, the measured output voltage is divided by the power at the exit of the fiber (entrance to the polychromator) to obtain the spectral responsivity shown in Fig. 4.4. The dotted line shows a Maxwellian distribution.

A simple calibration was performed using a calibrated standard light source traceable to the National Institute of Standards and Technology (NIST) standard. The light is modulated at 80 Hz by a chopper and irradiates a diffuser placed on the atmosphere side of the collection window (Fig. 4.5). The light reflected from the diffuser is collected by the fibers to simulate the scattered light. The output voltage v_i of each polychromator channel is

$$v_i \propto \int f_i(\lambda) L_{\mathrm{S}}(\lambda) d\lambda, \tag{4.5}$$

where f_i is the spectral responsivity function of each polychromator channel and $L_{\mathrm{S}}(\lambda)$ is the wavelength distribution of the calibrated standard light source. The relative gain of the responsivity functions are calibrated.

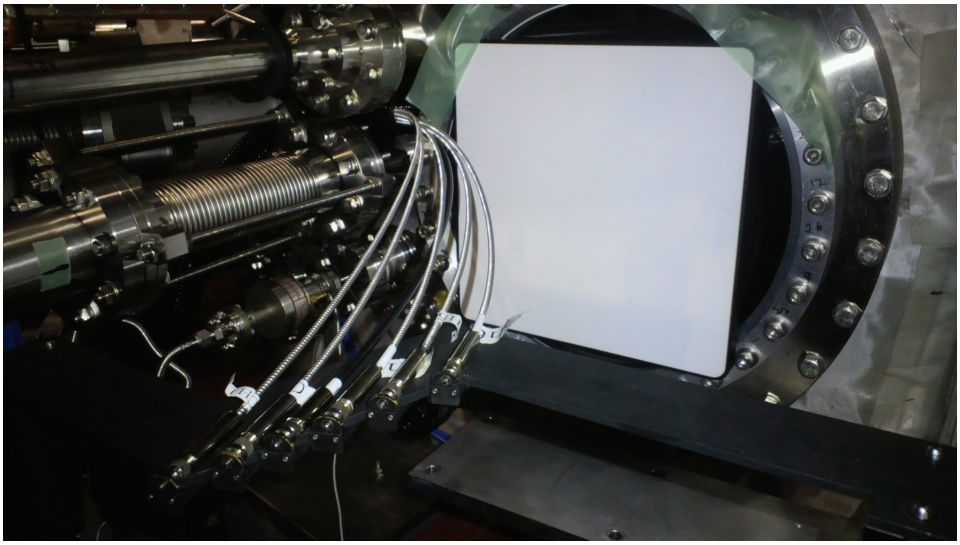

Fig. 4.5: Photograph of the diffuser placed in front of the collection window for simple calibration.

4.2 Density calibration

Raman scattering is used for density calibration. In a gas, Raman scattering can occur with a change in energy of a molecule due to a rotational transition [90, 91]. The wavelength shift λ_J of the initial rotational state J is given by

$$\frac{1}{\lambda_J} = \frac{1}{\lambda_{\mathrm{YAG}}} + \frac{1}{c}\left[(4B_0 - 6D_0)\left(J - \frac{1}{2}\right) - 8D_0\left(J - \frac{1}{2}\right)^3\right], \tag{4.6}$$

Where λ_{YAG} is the wavelength of the incident Nd:YAG laser, c is the speed of light, $B_0 = 198.97$ is the rotational constant, $D_0 = 5.74 \times 10^{-4}$) is the centrifugal distortion constant. The

population of the rotational state J is

$$w_{\mathrm{J}} = W^{-1} g_J (2J-1) \exp\left(-J(J+1)B_0 \frac{hc}{kT}\right), \tag{4.7}$$

where h is the Planck constant, k is the Boltzmann constant, T is the temperature of gas (=295 K), W is the normalization constant (for $\Sigma w_J = 1$), g_J is the statistical weight factor depending on the nuclear spin (6 for even J, 3 for odd J). The cross section of the rotational state J is

$$\sigma_J = \frac{64\pi^4}{45} \frac{3J(J-1)}{2(2J+1)(2J-1)} \frac{\gamma^2}{\lambda_J^4}, \tag{4.8}$$

where $\gamma_0 = 0.66 \times 10^{-30}$ is the polarizability anisotropy. The angular distribution for quadrupole Raman transition is

$$\frac{dI^{\mathrm{R}}}{d\Omega} = \frac{3}{8\pi} \frac{6 + \sin^2(\theta)}{10}, \tag{4.9}$$

$$\sigma_{\mathrm{R}}(\lambda_J, J) = w_J \sigma_J \frac{dI^{\mathrm{R}}}{d\Omega}, \tag{4.10}$$

$$\sigma_i = \sum_J \sigma_{\mathrm{R}}(\lambda, J) f_i(\lambda). \tag{4.11}$$

where $f_{\mathrm{i}}(\lambda)$ is the spectral responsivity function for each polychromator channel. A calculated Raman scattering spectrum is shown in Fig. 4.6. The Raman scattering spectrum decreases as the wavelength shifts away from the laser wavelength, and the signals in channels 5 and 6 are much smaller than the signals in channels 1 – 4.

The slope of Thomson scattering signal versus electron density l_{T} is calculated from the slope of Raman scattering signal versus gas pressure l_R (Fig. 4.7) as

$$l_{\mathrm{T}} = l_{\mathrm{R}} kT \frac{\sigma_{\mathrm{T}}}{\sigma_i} \frac{760}{101325}. \tag{4.12}$$

Based on the calibration results thus obtained, the density profile was measured in high density, reproducible plasmas sustained by 28 GHz RF power (Fig. 4.9). The result graph is close to result of ray trace $L\Omega$ (Fig. 3.15) The values at inboard side are high and those at outboard side is low. The value at second inner point is lower, it is seem that effect of shadow.

The measured Raman scattering intensities for different spatial channels of the polychromator are shown in Fig. 4.8.

The electron density n_{e} is calculated from the coefficient $n_{\mathrm{e}} L P_i \Delta\Omega G C_{\mathrm{T}} \frac{d\sigma}{d\Omega}$ obtained from Maxwell fitting analysis, using the Raman scattering calibration result. However, the density obtained from Thomson scattering data is not in agreement with other measurements, and the values from different channel are inconsistent. Since the line integrated density measurement by microwave interferometry is highly reliable, the absolute density is determined by normalizing the line integrated density obtained by Thomson scattering.

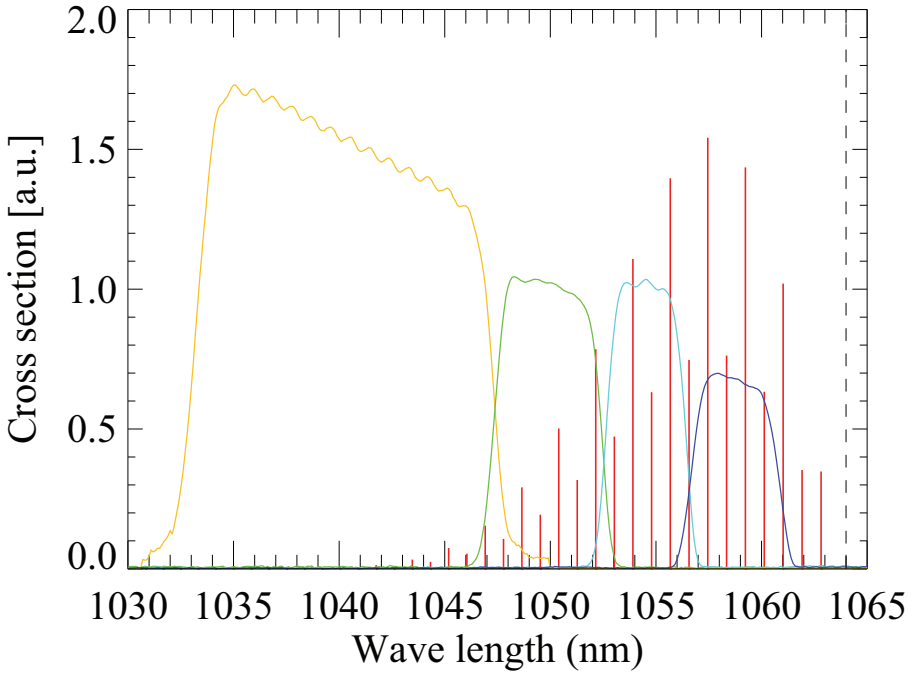

Fig. 4.6: Calculated spectrum of rotational Raman shift (red vertical bars).

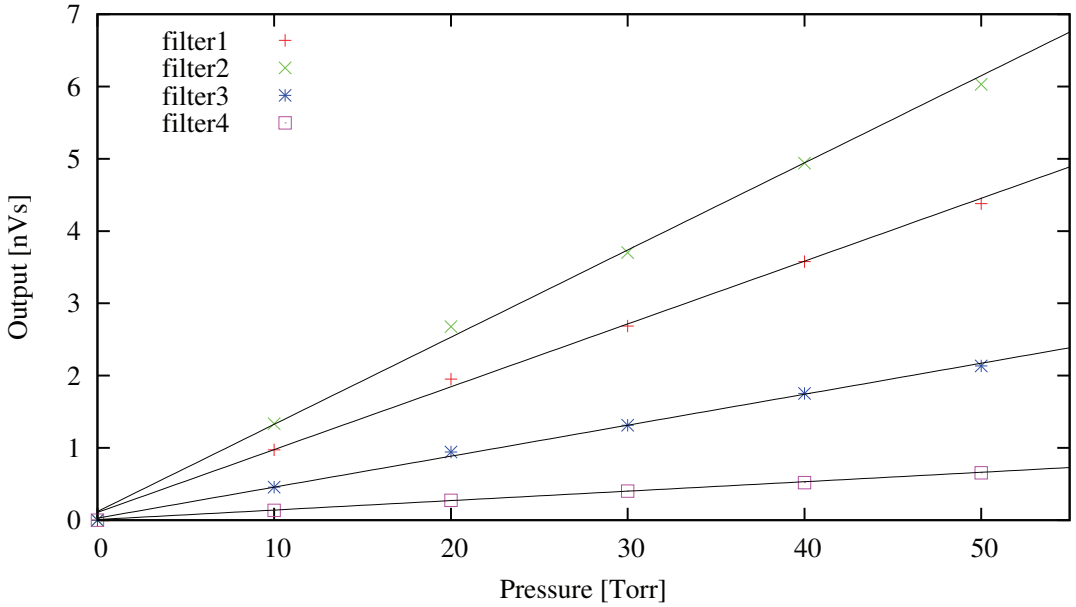

Fig. 4.7: Raman scattering signal as a function of nitrogen gas pressure for 4 channels of the polychromator. The signals of channel 5 and 6 are very low and unreliable

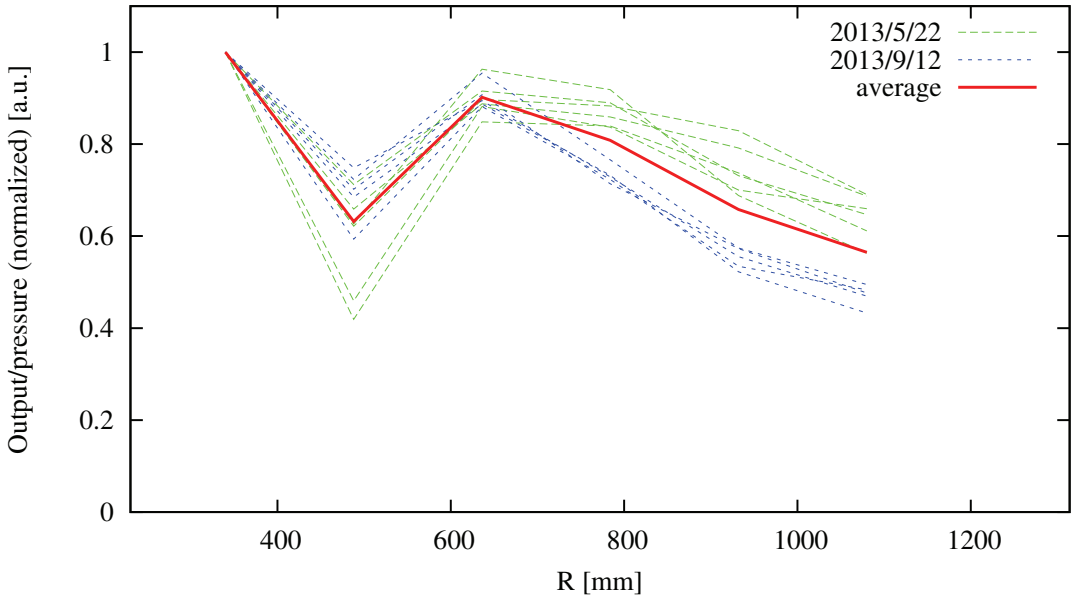

Fig. 4.8: Radial profile of Raman scattering intensity for different polychromator channels measured on two different dates separated by about four months. The intensities are normalized by the intensity at $R = 340\,\mathrm{mm}$. The red curve is the average.

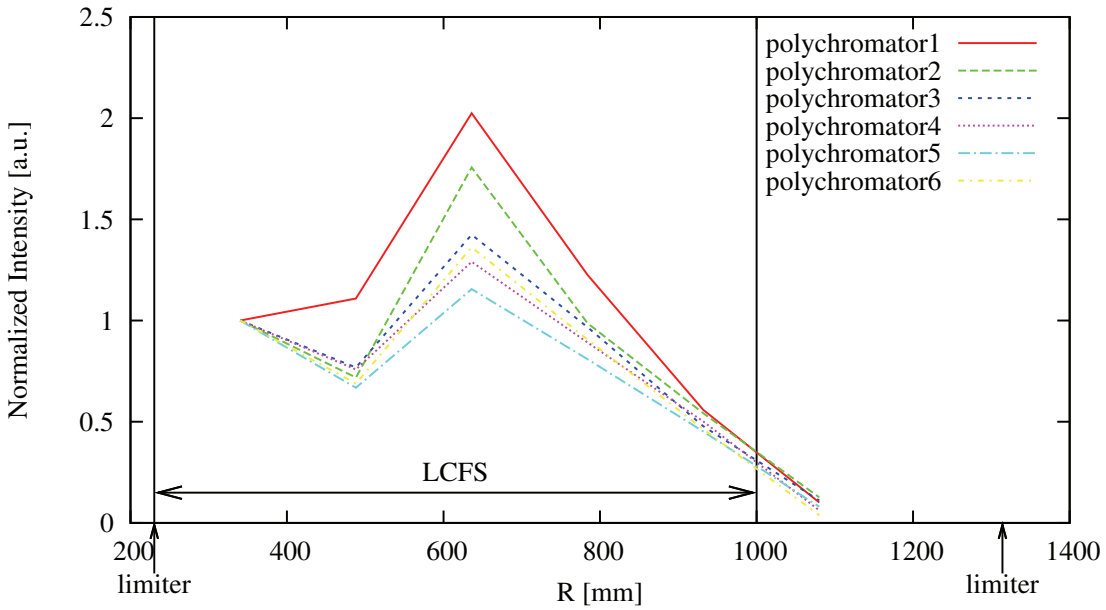

Fig. 4.9: Electron density profile measured by Thomson scattering (in arbitrary units) in high density, reproducible plasmas sustained by 28 GHz RF power. The six polychromator channels (and six fibers) were rearranged to measure every spatial point by each polychromator.

4.3 Signal processing

The expected shape of the scattered laser pulse, $I_s(t)$, can be constructed by convolving the Gaussian laser pulse with the low-pass characteristic response of the amplifier system, [92].

$$I_s(t; C, \tau_L, \tau_a, t_L) = C \int_0^t \exp\left[-\frac{(t' - t_L)^2}{\tau_L^2}\right] \exp\left(-\frac{t - t'}{\tau_a}\right) dt'. \tag{4.13}$$

where t_L is the time when the laser pulse amplitude reaches its peak, τ_L is the time duration of the laser pulse, and τ_a is the characteristic time of the amplifier system. These time constants were adjusted to produce the best fit to the measured time evolution of the scattered pulse. Calculating the integral in Eq. (4.13),

$$I_s(t; C', \tau_L, \tau_a, t_L) = C' \exp\left(-\frac{t - t_L}{\tau_a}\right)\left(1 - \mathrm{erf}\left(\frac{\tau_L}{2\tau_a} - \frac{t - t_L}{\tau_L}\right)\right). \tag{4.14}$$

The parameters C', τ_L, τ_a, t_L are determined by fitting. Although C' is a function of τ_L and τ_a, it is assumed to be a constant.

Figure 4.10 shows an example of the fitted pulse shape function to a Raman scattered signal waveform. The signal to noise ratio is high for Raman scattering at high pressure. This signal was measured at scattering volume S1 at 40 Torr, and averaged over 32 pulses.

The stray light is measured immediately after a plasma discharge. The measured pulse width is longer than discharge time,as shown in Fig. 4.11.

In order to explain signal processing, an example with strong scattered signal is described. Figure 4.12 shows waveforms of scattered light detected by each APD in a polychromator. The measured scattering volume is at $R = 340\,\mathrm{mm}$, and four pulses were accumulated. In this case, the plasma density was relatively high ($\sim 10^{18}\,\mathrm{m}^{-3}$), and strong signals were observed. The output signal was fitted well by a template pulse shape function. The time integral of this pulse shape function was evaluated analytically to yield the scattered signal intensity which is proportional to the detected photon number. The error in the scattered signal intensity is estimated from function fitting, and was almost constant and independent of channels. This error is used as the weight in fitting to a Maxwell distribution.

The integrated signals for different spectral channels of a polychromator were fitted the expected scattered signals for a Maxwell distribution with given density and temperature. The fitting calculation is repeated twice. In the first fitting, the errors described above were used to determine the weights, as the inverse square of errors of integrated signals, and χ^2 is calculated. In the second fitting, this $\sqrt{\chi^2}$ was used as the error for each integrated signal. It should be noted that the errors are the same for all APD ' s. Figure 4.13 shows the integrated signal divided by the wavelength bandwidth for the six filters. The error bars are the ones used in the second fitting, also divided by the wavelength bandwidth of each filter. The resultant electron temperature was 89 ± 5 eV for this case. The relative electron density can also be calculated from the fit. The coefficient to convert from the relative density to the absolute density was obtained by the method described in the previous section. The errors of electron temperature and density are calculated from the propagation law of errors [93, 94].

Plasmas sustained by 8.2 GHz RF power have low densities. Therefore, scattered signals are very weak, and the signal to noise ratio is very low (≤ 1). In order to improve the signal to noise ratio, raw scattered signals are accumulated over many laser pulses. The noise can

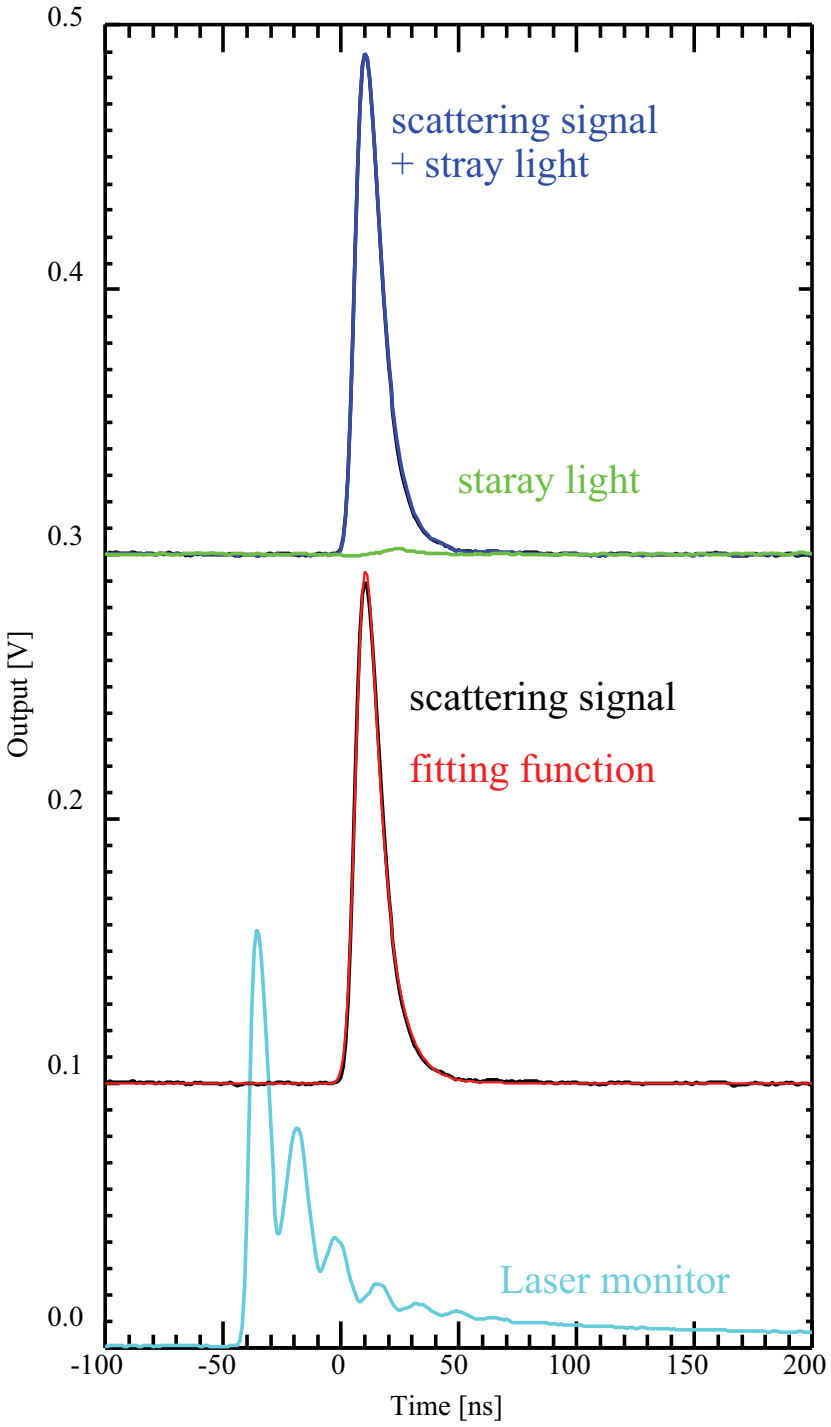

Fig. 4.10: Waveform of Raman scattered signal and the fitted pulse shape function $I_{\rm s}(t; C', \tau_{\rm L}, \tau_{\rm a}, t_{\rm L})$. The laser monitor signal is also displayed.

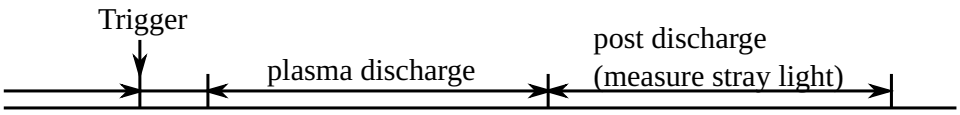

Fig. 4.11: Time line of measurement relative to a plasma discharge.

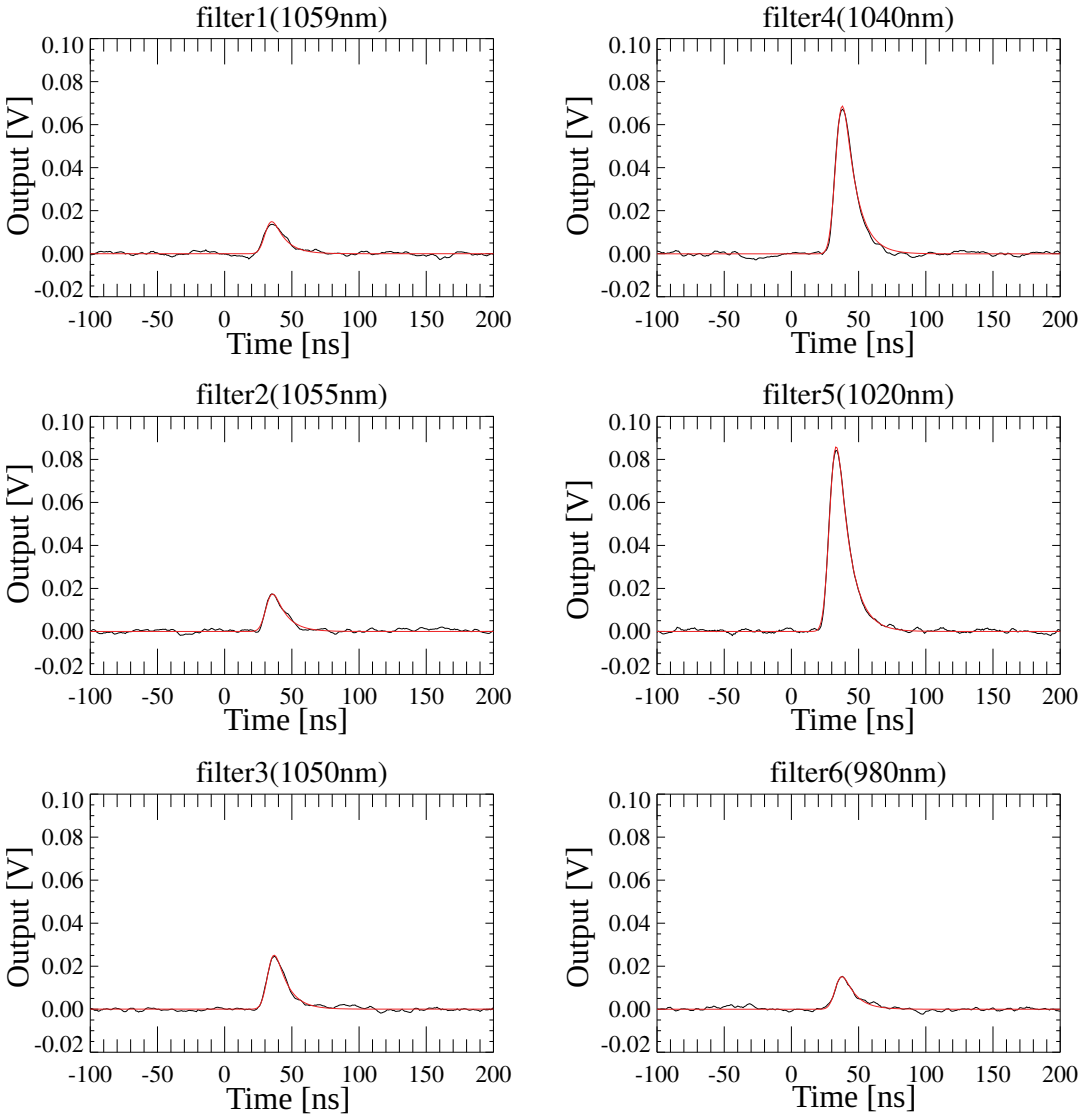

Fig. 4.12: Waveforms of scattered light(black) and fitted function (red) for the six spectral channels of a polychromator.

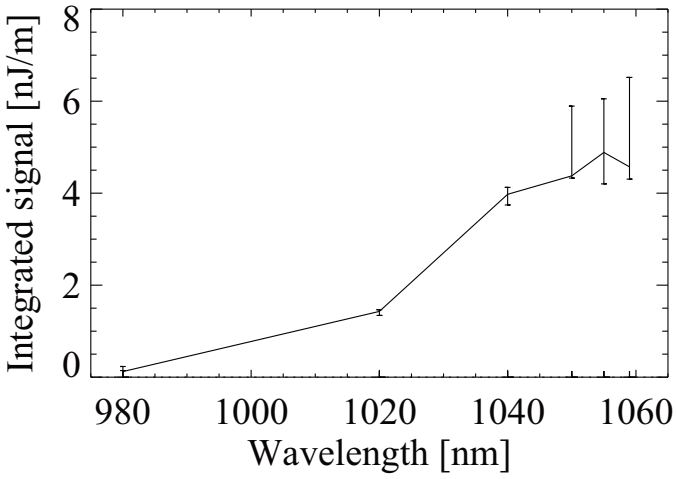

Fig. 4.13: Example of fit to a Maxwell distribution.

be reduced by factor of $\sqrt{N}$, where N is the number of accumulated pulses. This is justified when the plasma can be assumed to be in steady state so that the temperature and density remain the same over many laser pulses.

In QUEST, long steady state periods and reproducible discharges are achieved relatively easily. The effect of accumulation is shown in Fig. 4.14. In this case, the discharge duration was 20 sec (200 laser pulses per discharge) and 10 reproducible discharges were used. The signal to noise ratio was improved dramatically by signal accumulation.

When scattered signals are accumulated over a long discharge period, the plasma must be confirmed to be in steady state. Figure 4.15 shows the time evolutions of the electron temperature and density for a long pulse, low density discharge sustained by 8.2 GHz RF power. It can be seen that the temperature and density are nearly constant over a long period. The discharge is divided into four time windows to see the time evolution, each with accumulation of 12 plasma shots with 50 laser pulses per shot (total of 600 laser pulses).

An example of a higher density, shorter pulse discharge sustained by 28 GHz RF power is shown in Fig. 4.16. The density is an order of magnitude higher than discharges sustained by 8.2 GHz RF power, so the required accumulation number is much smaller (5 laser pulses). In order to improve the signal to noise ratio, the scattered signals are accumulated over the time window of 2.2 – 2.6 sec, during which the temperatures and densities are nearly constant.

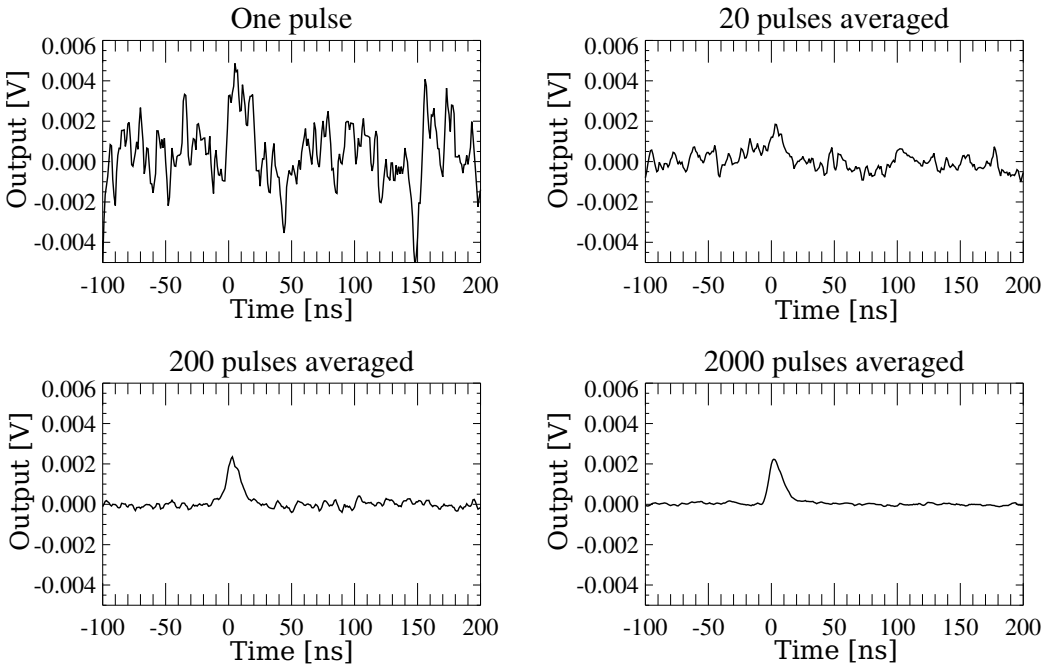

Fig. 4.14: Accumulated scattered light signals showing the improvement of the signal to noise ratio as the number of accumulated laser pulses increases.

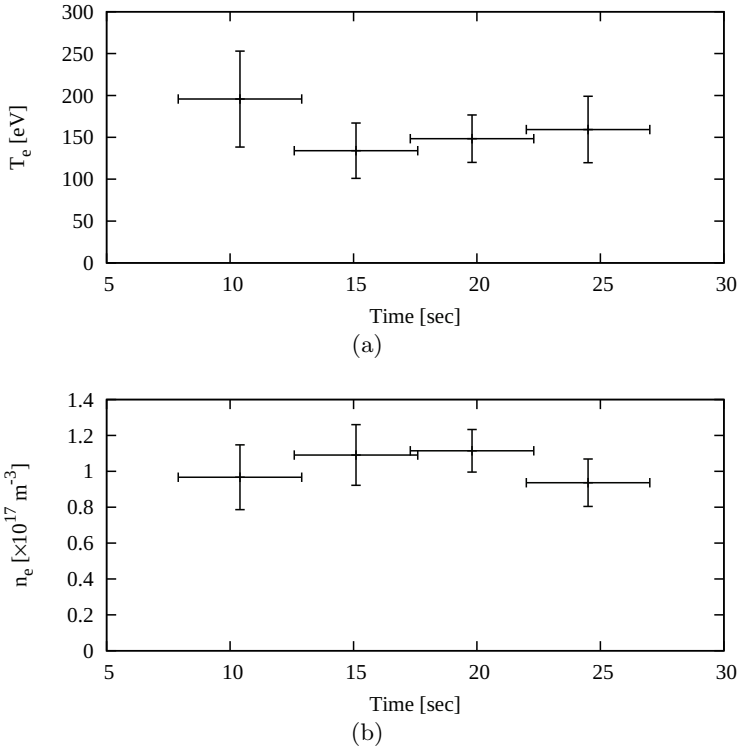

Fig. 4.15: Electron temperature (a) and density (b) evolutions for a long pulse, low density discharge sustained by 8.2 GHz RF power.

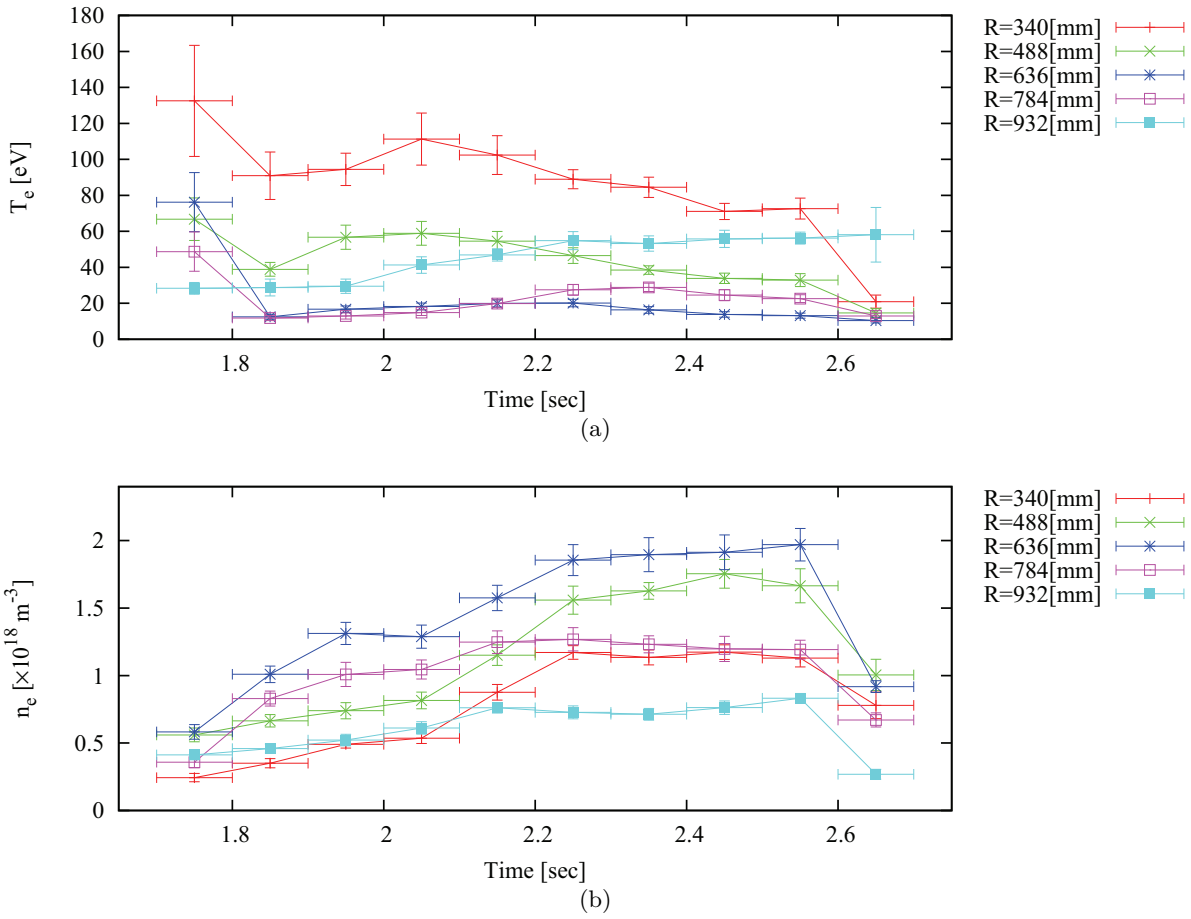

Fig. 4.16: Electron temperature (a) and density (b) evolutions for a higher density and shorter pulse discharge sustained by 28 GHz RF power. The plasma is in steady state during the period 2.2 – 2.6 sec.

Chapter 5

Experimental Results

5.1 28 GHz Experiment

Plasmas driven by 28 GHz RF power have much higher densities than plasmas driven by 8.2 GHz RF power because the cutoff density is an order of magnitude higher. The cutoff density for 28 GHz is $9.7 \times 10^{18}\,\mathrm{m}^{-3}$. Typical magnetic flux surfaces and waveforms of a plasma sustained by 28 GHz RF power are shown in Fig. 5.1 and Fig. 5.2, respectively. The toroidal field coil current is $I_{\mathrm{TF}} = 50$ kA, corresponding to the toroidal field strength (at $R = 650$ mm) of 0.25 T. The second harmonic EC resonance for 28 GHz is located at $R = 320$ mm. The plasma boundaries (LCFS) are located on the inboard limiter and at $R = 1000$ mm (inboard limiter configuration). The plasma major radius is 600 mm and the minor radius is 400 mm. Two hundred kilowatts of 28 GHz RF power was injected from 1.6 s to 2.6 s. Hydrogen gas was puffed at 1.7 s, 1.85 s, 2.0 s and 2.15 s. The Hα emission increased at these times. The plasma current is stable at 22 kA from 2.2 s to 2.6 s. This period is taken as the steady state period, because most measured quantities are nearly constant during this period. The line integrated density is stable at $1.7 \times 10^{18}\,\mathrm{m}^{-2}$. The loop voltage is nearly zero, indicating that the plasma current is sustained non-inductively. The 28 GHz stray RF power, measured by a detector outside the vacuum vessel, samples the RF power that was not absorbed by the plasma and escaped from the vacuum vessel. The Hα emission decreases slightly and the OII emission increases slightly during the steady state period. Both AXUV signal (total photon emission) and SBD signal (soft X-ray emission) increase slightly during the steady state period. Since AXUV and SBD signals are affected easily by impurities in the plasma, the large shot-to-shot variation might be caused by different levels of impurity contamination.

Figure 5.3 shows the electron temperature, density and pressure profiles at different times for the discharge shown in Fig. 4.16. During the steady state period (labeled 2.25 s – 2.55 s), the temperature and density profiles remain nearly the same. The inboard density during this period is higher than at other times (1.75 s – 2.15 s and 2.65 s). The scattered signal was too weak to obtain a satisfactory fit for the unplotted times at $R = 1080$ mm. During the steady state period (labeled 2.25 s – 2.55 s), the profiles remain nearly the same. The inboard density during this period is higher than at other times (1.75 s – 2.15 s and 2.65 s). The initial electron temperature at innermost point is highest than other point or period. The electron densities are increased. The inner three points or the outer two points are seem the same tendency.

The electron temperature profile is unusual, with a low temperature (about 20 eV) near the

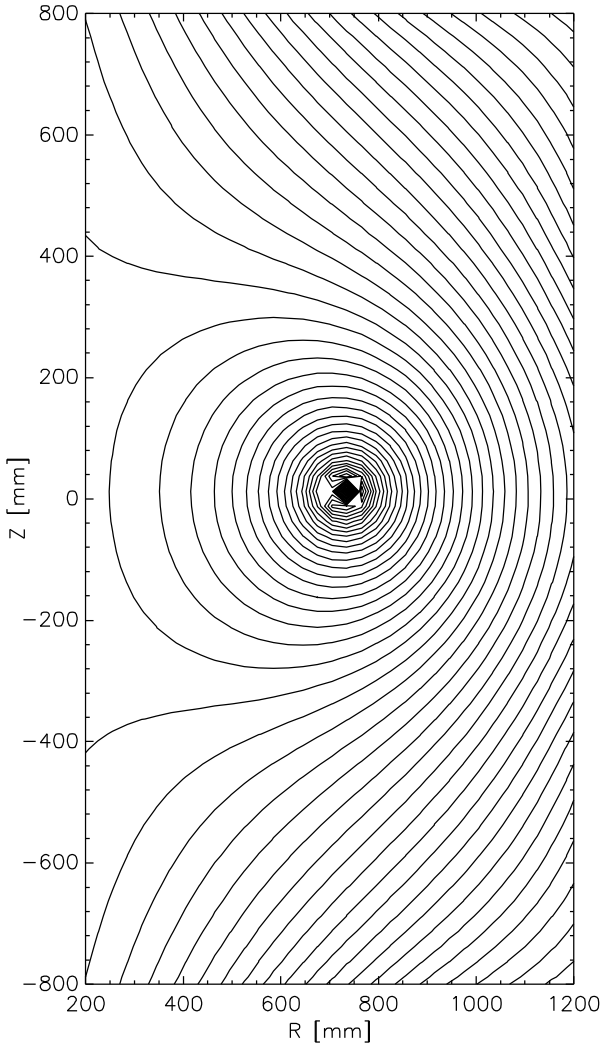

Fig. 5.1: Typical magnetic flux surfaces by EFIT of a plasma sustained by 28 GHz RF power (shot no. 22400, 2.5 s).

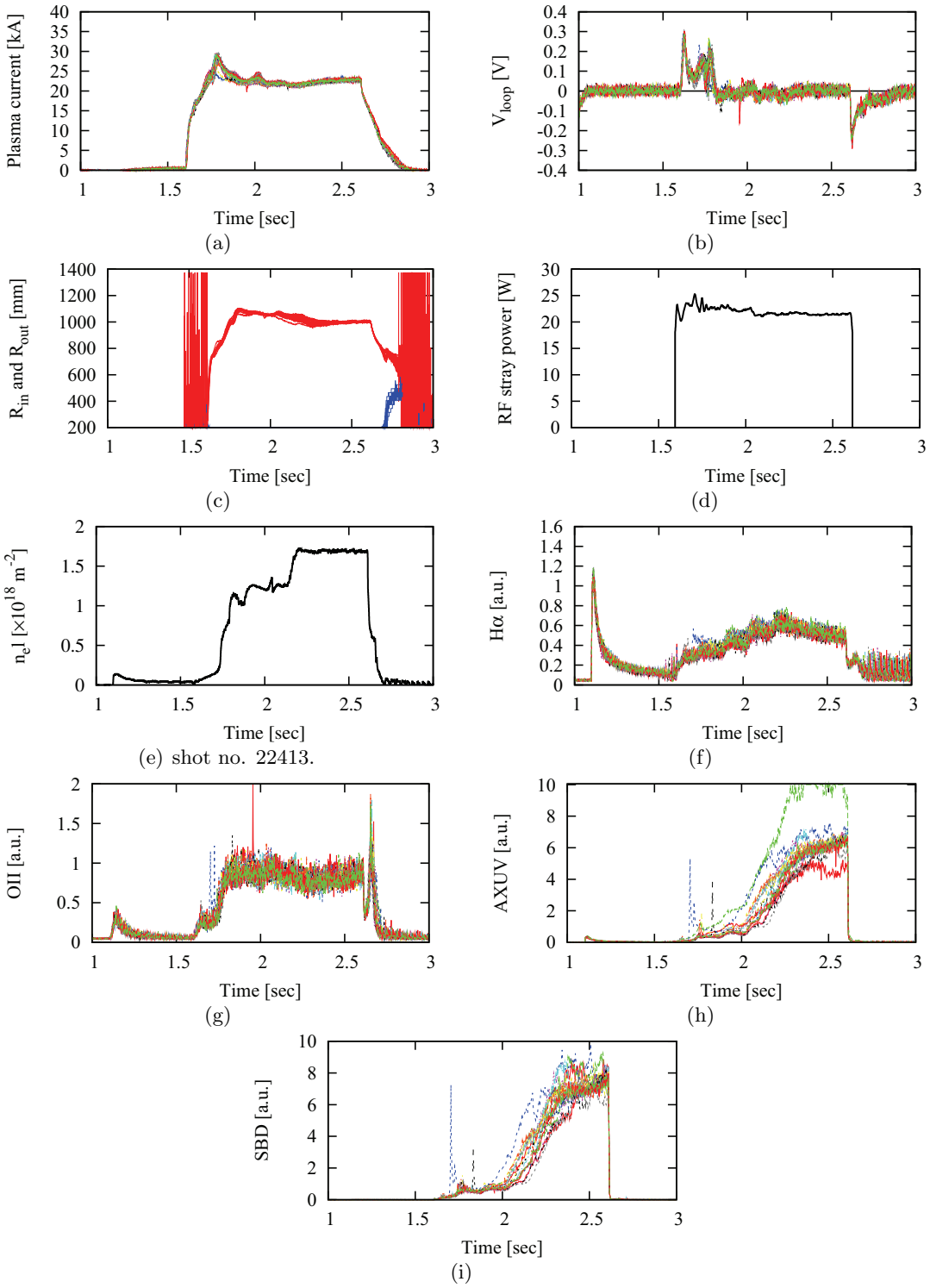

Fig. 5.2: Waveforms of plasmas sustained by 28 GHz RF power. (a) Plasma current, (b) loop voltage, (c) inboard (blue) and outboard (red) boundary positions ($R_{\rm in}$ and $R_{\rm out}$) of the plasma determined by RTFIT, (d) 28GHz stray RF power to indicate RF injection timing, (e) line integrated electron density, (f) Hα emission, (g) OII emission, (h) total photon emission, and (i) soft X-ray emission. Colors indicate different discharges used for photon accumulation.

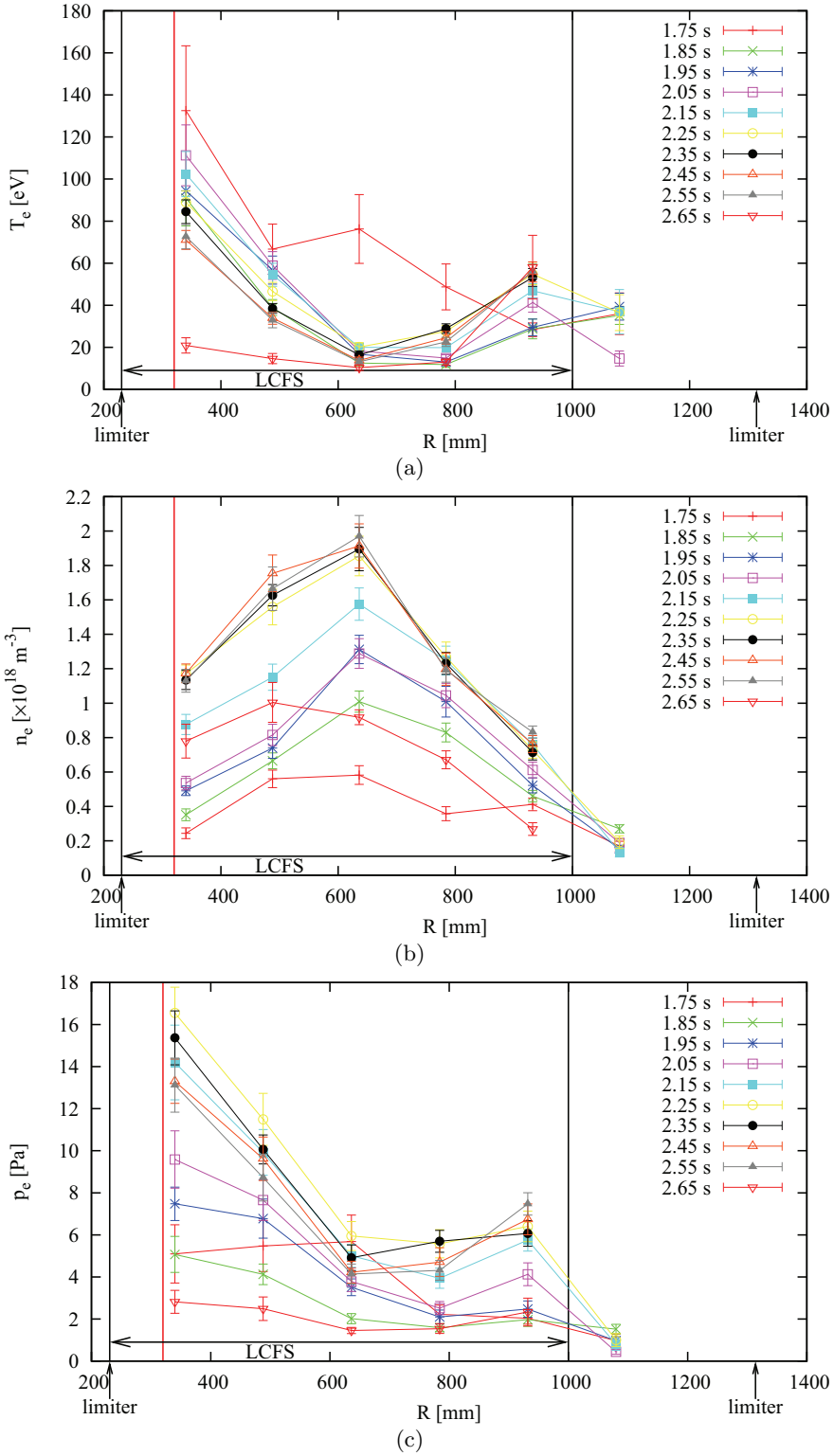

Fig. 5.3: Profiles of (a) electron temperature T_e, (b) electron density n_e, and (c) electron pressure p_e in plasmas sustained by 28 GHz RF power. The black lines indicate the inboard and outboard boundaries of the plasma determined by RTFIT, and the red line indicates the position of the second harmonic EC resonance (shot nos. 22389 – 22418).

plasma center and higher temperatures near the inboard and outboard edges. The temperature near the inboard edge, where the second harmonic EC resonance layer is located, was about 100 eV during the steady state period. For lower density plasmas sustained by 8.2 GHz RF power, electron temperatures as high as 400 eV were measured (see Section 5.2).

5.2 8.2 GHz Experiment

In QUEST, experiments with 8.2 GHz RF power have been performed with various configurations. Among them, the inboard poloidal field null configuration is most reproducible and relatively high density plasmas are obtained. The cutoff density for 8.2 GHz is $8.3 \times 10^{17}\,\mathrm{m}^{-3}$. In this section, experimental results obtained with the inboard poloidal field null configuration are presented. Data obtained with other magnetic configurations are presented in Appendix A.

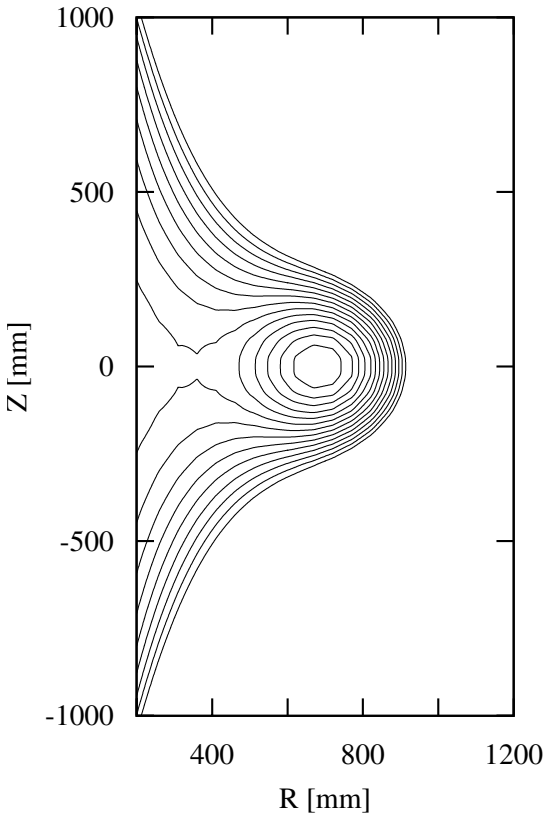

(a)

This figure cannot be displayed in the web version due to the copyright of the journal.

Fig. 3 (d). S. Tashima et al., Plasma Fusion Res. 8, 2402118 (2013).

(b)

Fig. 5.4: Typical magnetic flux surfaces of an inboard poloidal field null configuration sustained by 8.2 GHz RF power (shot no. 19102 during the steady state period: 3 s – 8 s). Figures (a) and (b) show flux contours calculated by the QUEST numerical calculation system and by the PCF code, respectively [64].

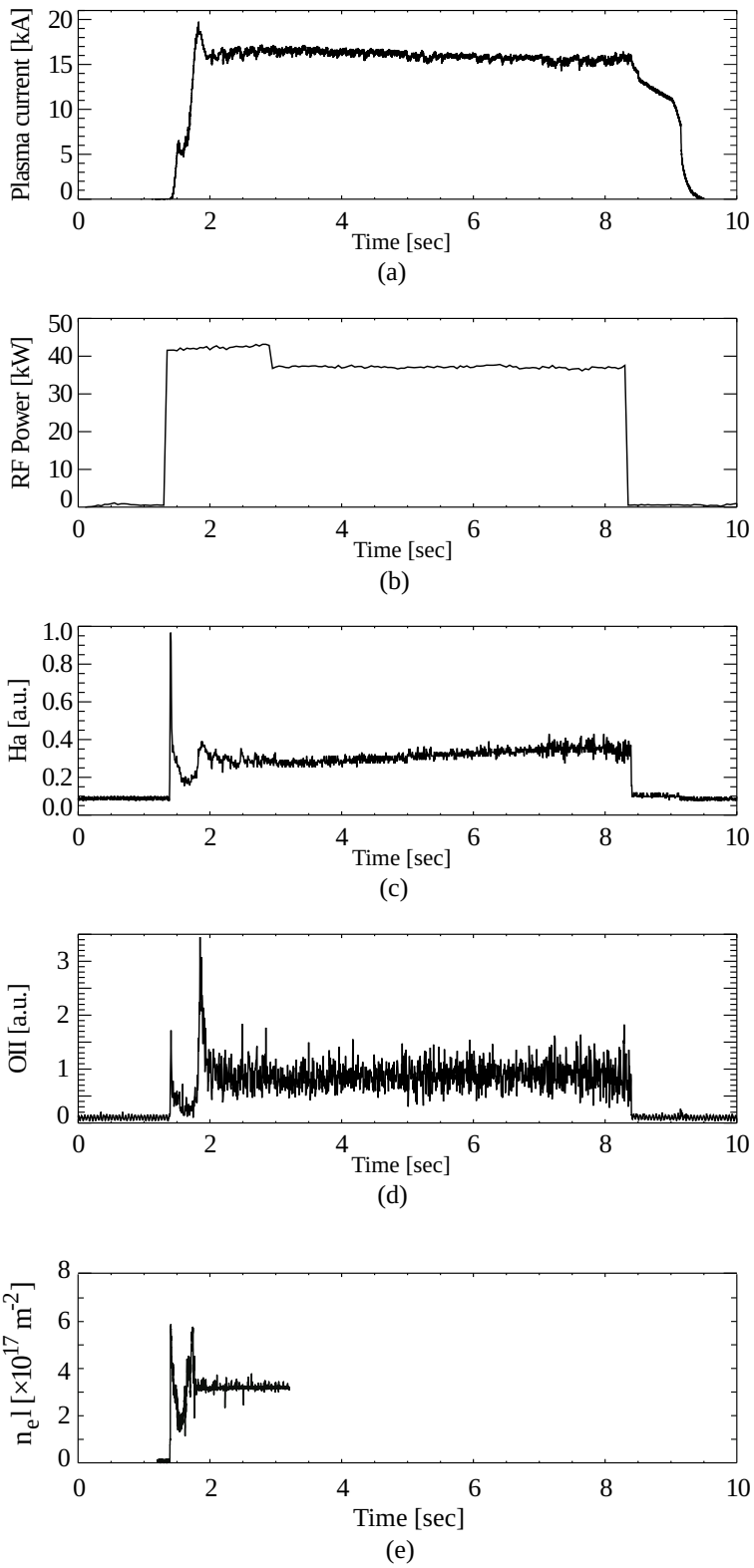

Fig. 5.5: Waveforms of (a) plasma current, (b) net RF power, (c) H_α emission, (d) O_{II} emission, and (e) line integrated density in an inboard poloidal field null plasma sustained by 8.2 GHz RF power (shot no. 19102).

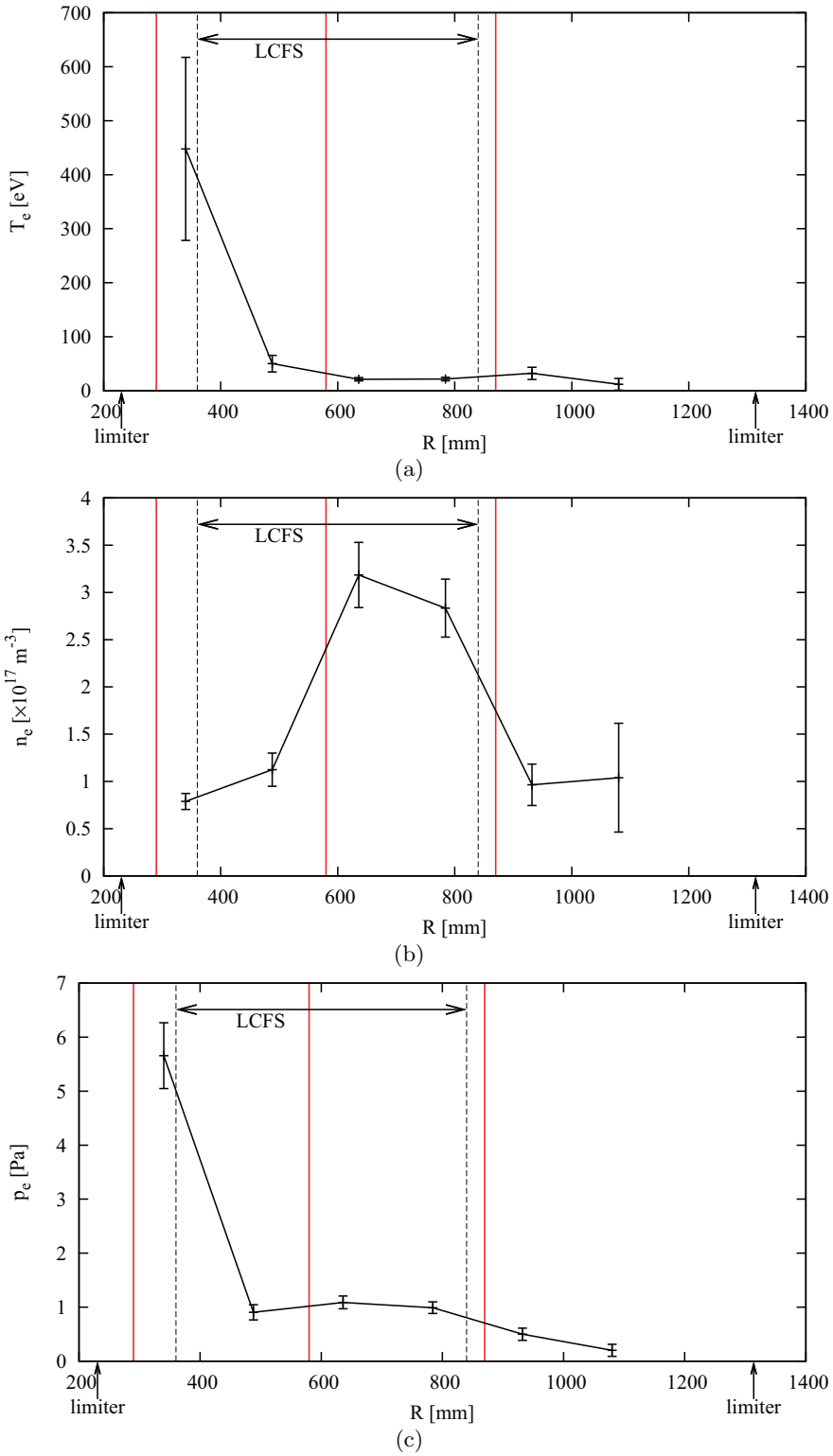

Fig. 5.6: Profiles of (a) electron temperature, (b) electron density, and (c) electron pressure of an inboard poloidal field null plasma sustained by 8.2 GHz RF power. The black lines indicate the inboard and outboard plasma boundaries determined by RTFIT. The red lines indicate the EC resonance layers (shot nos. 19101 – 19117).

Typical magnetic flux surfaces of an inboard poloidal field null plasma sustained by 8.2 GHz RF power, calculated by the QUEST numerical system and by the PCF code are shown in Fig. 5.4. Discharge waveforms are shown in Fig. 5.5. The toroidal field coil current is $I_{\mathrm{TF}} = 26.6$ kA, corresponding to the toroidal field strength at $R = 650$ mm of 0.13 T. The fundamental resonance for 8.2 GHz is located at $R = 290$ mm. In the inboard poloidal field null configuration on QUEST, strong poloidal magnetic fields are produced by driving 3 kA in the upper and lower PF coils (PF 35).

The plasma current is nearly constant at 17 kA from 3 s to 8 s (steady state period). The line integrated density is stable at about $3 \times 10^{17}\,\mathrm{m}^{-2}$ during this period. The net injected 8.2 GHz RF power measured by directional couplers was 37 kW. The gas was puffed every 0.2 sec. The Hα emission increases slightly but OII emission stays nearly constant during the steady state period.

A highly unusual electron temperature profile was observed, as shown in Fig. 5.6. The electron temperatures were very low (several tens of eV) inside the LCFS, but a very high electron temperature (400 eV) was observed on the inboard side of the poloidal field null, near the fundamental EC layer.

The location of the fundamental resonance layer for 8.2 GHz depends on the TF coil current I_{TF} [kA] as $R_{\mathrm{res}} = 10.9 \times I_{\mathrm{TF}}$. The toroidal field strength B_{T} [T] (at $R = 650$ mm) was varied from 0.13 T to 0.20 T ($I_{\mathrm{TF}} = 26.6$ kA to 40 kA). Compared to the discharge shown in Fig. 5.6, the injected RF power is doubled (about 80 kW in this scan), and the high temperature ($> 200\,\mathrm{eV}$) region is broader. The gas puff rate and the colloidal field strength are also different as a consequence. Figure 5.7 shows time evolutions of the plasma current for three discharges used in this scan. The vertical lines indicate the beginning and the end of the accumulation time window for Thomson scattering analysis.

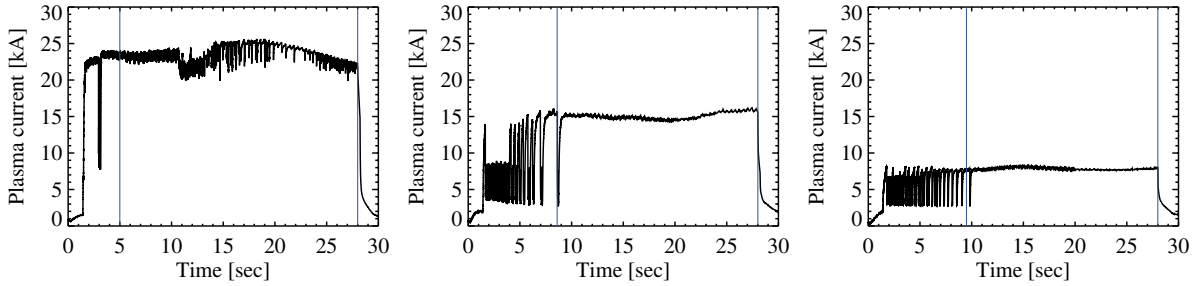

(a) $B_{\mathrm{T}} = 0.13\,\mathrm{T}$ (SN23140) (b) $B_{\mathrm{T}} = 0.17\,\mathrm{T}$ (SN23194) (c) $B_{\mathrm{T}} = 0.20\,\mathrm{T}$ (SN23184)

Fig. 5.7: Time evolutions of the plasma current at various toroidal field strengths. The vertical lines show the beginning and the end of the accumulation time window for Thomson scattering analysis.

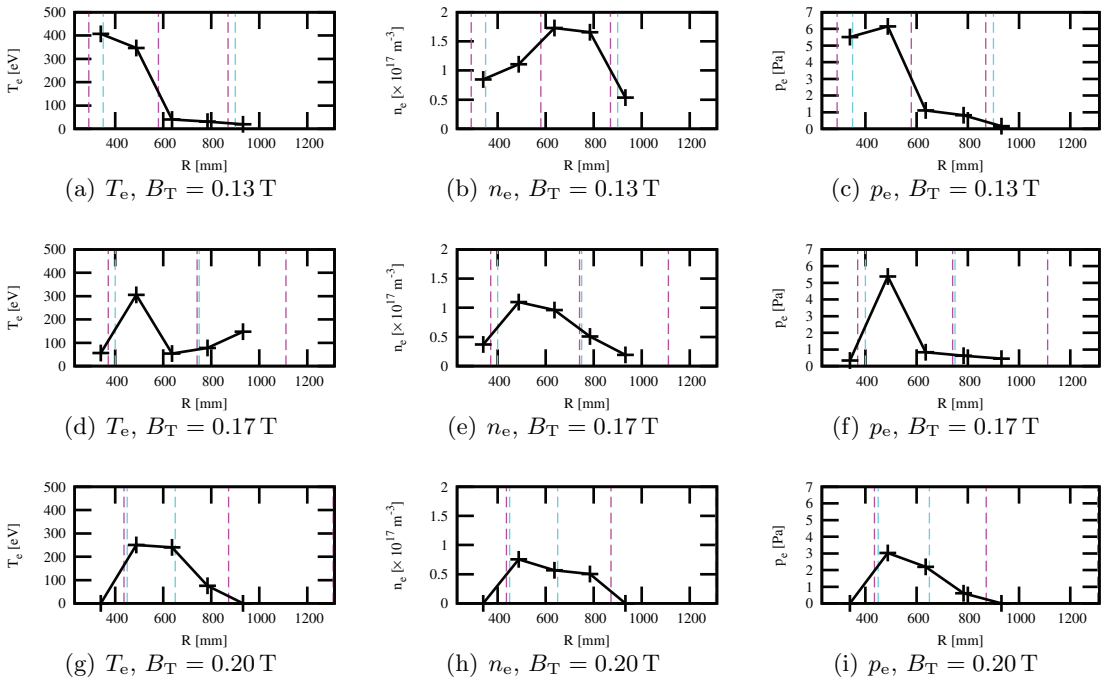

(a) T_e, $B_T = 0.13\,T$ (b) n_e, $B_T = 0.13\,T$ (c) p_e, $B_T = 0.13\,T$

(d) T_e, $B_T = 0.17\,T$ (e) n_e, $B_T = 0.17\,T$ (f) p_e, $B_T = 0.17\,T$

(g) T_e, $B_T = 0.20\,T$ (h) n_e, $B_T = 0.20\,T$ (i) p_e, $B_T = 0.20\,T$

Fig. 5.8: Electron temperature, density and pressure profiles for three different toroidal field strengths. The blue lines indicate the inboard and outboard plasma boundaries calculated by RTFIT. The red lines indicate the EC resonance layers.

The peak of the electron temperature profile is shifted to larger major radius as B_T is increased and the resonance layer is shifted outward. When the fundamental resonance layer is located to the low field side of the innermost changed, $R = 340\,mm$ ($B_T \geq 0.17$), the temperature measured at this location becomes very low. The high temperature region is located on the low field side of the resonance layer.

5.3 Discussion

5.3.1 Difference between 28 GHz and 8.2 GHz experiments

Here, we would like to compare the plasmas sustained by 28 GHz RF power (200 kW) (Fig. 5.3) and by 8.2 GHz RF power (40 kW) (Fig. 5.6). The density in the 28 GHz experiment is about an order of magnitude higher than that in the 8.2 GHz experiment. This fact is probably due to the difference in the cutoff density, which affects the refraction of the injected rays. The central and the inboard pressures in the 28 GHz experiment are about twice and four times higher than those in the 8.2 GHz experiment, respectively. Since the injected power is about five times higher for the former, this pressure difference is reasonable, when we consider confinement degradation due to the higher power. In both cases, the position of the highest temperature is located near the inboard resonance (second harmonic for 28 GHz, fundamental for 8.2 GHz). In addition, the central region seems to have the lowest temperature (and the highest density). Since RF wave power is absorbed near the lowest order EC resonance layer located in the inboard edge region, such temperature profiles may be expected. The reason for

the low central temperature is probably due to poor RF wave accessibility to the high density region and poor central confinement due to collisions with neutrals or radiation. It should be noted that the effect of radiation can be serious for the temperature range of several tens of eV, and the neutral density can be high in these low density plasmas. In general, the electrons heated at the inboard side resonance travel towards the outboard side on the magnetic surface. As a result, the temperature tends to equalize on the same magnetic surface. In the 28 GHz experiment, the outboard temperature is higher than the central temperature, but lower than the inboard temperature. Therefore, temperature equalization is not perfect. Furthermore, the pressure profile is asymmetric. One possible reason is poor bulk electron confinement. Qualitatively similar features are observed in the 8.2 GHz experiment.

5.3.2 Dependence on the toroidal field strength

Here, we discuss the results of the toroidal field strength scan experiment (Fig. 5.8). The toroidal field strength at $R = 600$ mm was varied from 0.13 T to 0.20 T, and the radial position of the fundamental resonance for 8.2 GHz varied from $R = 290$ mm to 436 mm. The injected RF power (80 kW) and other operational conditions (except the gas puff rate) were the same. The central region seems to have the highest density, and the peak position tends to move inward as the resonance layer moves outward, but this may be a result of the shrinking outboard boundary of the plasma (indicated by blue vertical lines) as the resonance layer moves outward. The position of the maximum temperature is located just on the outboard side of the fundamental resonance layer, and it moves with the resonance layer position. This can be explain by the Doppler shifted resonance condition

$$\omega - k_{\parallel} v_{\parallel} - \frac{n\Omega_e}{\gamma} = 0. \tag{5.1}$$

The electrons with $k_{\parallel} v_{\parallel} > 0$ satisfy this condition and are heated at a lower field. This condition is called up-shift [31, 70, 95]. The electron cyclotron wave is injected in QUEST as the ordinary mode with the parallel refractive index $N_{\parallel} = k_{\parallel} c/\omega \simeq 0.4$, corresponding to a large up-shift [96]. $N_{\parallel}$ is sufficiently large at the fundamental resonance located at $R = 290\,\mathrm{mm}$.

The plasma current decreases and the volume inside the LCFS decreases as the toroidal field strength increases. The shrinking of the LCFS may be responsible for the apparent shift of the peak of the density profile to shift to the high field side as B_{T} is increased. The temperature at the second harmonic resonance layer is always low, and it can be interpreted either by high density (for the lower field cases) or by poor confinement outside LCFS (for the higher field cases).

Figures 5.9(a)–(c) show the toroidal field strength dependencies of the average temperature, the average density and the plasma current. These quantities decrease with the toroidal field strength, most likely because of the shrinking plasma volume. The highest plasma current was achieved when the fundamental resonance layer is located at $R = 290$ mm, which is very close to the inboard limiter position of $R = 230.5$ mm. The position of the second harmonic resonance layer is probably not important for the plasma as explained above. This is quite different from the case of 28 GHz experiment, in which the fundamental resonance layer does not exist inside the vacuum vessel and the second harmonic resonance layer is located near the inboard limiter.

Figure 5.9(d) shows the relationship between the average temperature and the average density. A positive correlation can be seen. In general, increase in pressure arises from improved confinement or from increased heating power. In the present case, the increased plasma current and plasma volume would contribute to improved confinement at lower field. Since the bulk electrons are heated by high energy electrons, their temperature should increase when the density of high energy electrons increases. The relationship between the density of bulk electrons and the density of high energy electrons is not simple, because bulk electrons can be the source and the sink of high energy electrons.

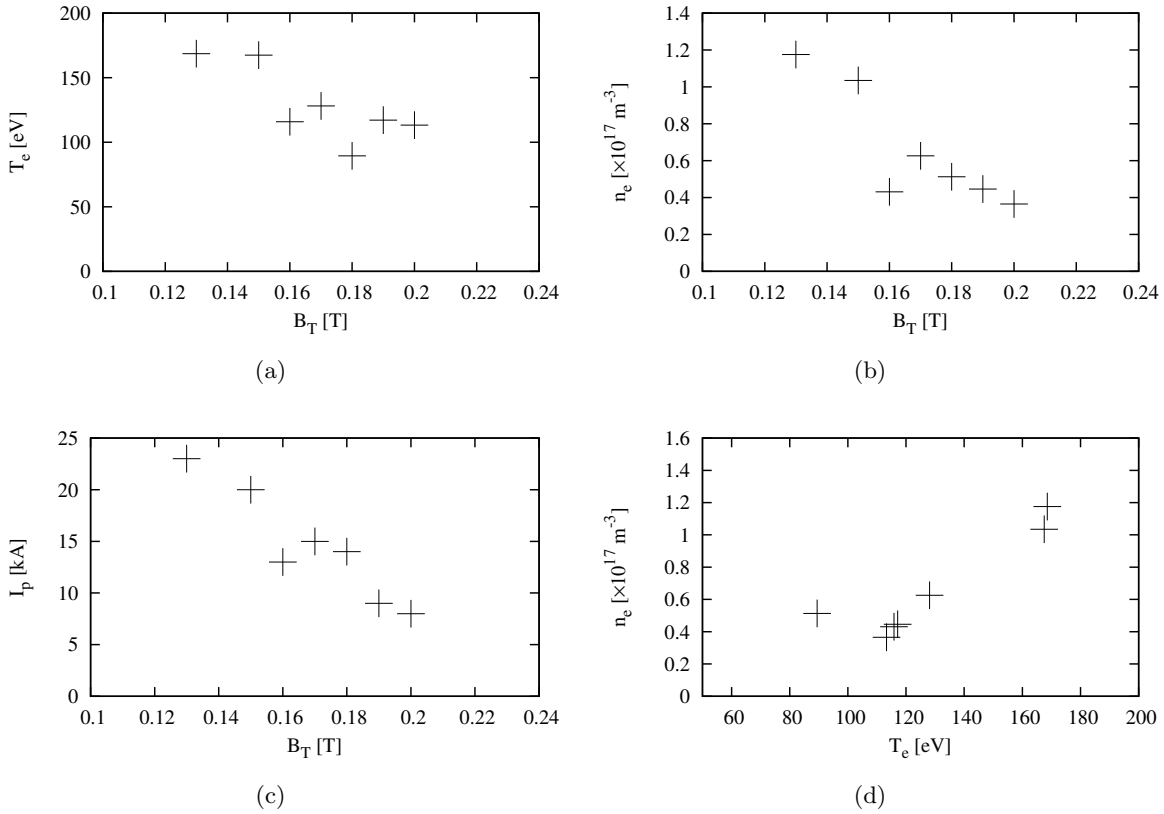

Fig. 5.9: Toroidal field dependence of (a) the average temperature, (b) the average density and (c) the plasma current, and (d) the relationship between the average temperature and the average density.

5.3.3 Collision and transport

Collision frequencies of a typical plasma sustained by 28 GHz RF power are as follows. The collision frequency is given by $\nu_e = 2.9 \times 10^{-12} \ln \Lambda n_e T_e^{-3/2}$ from Eq. (1.12). In the central region, the collision frequency is $9 \times 10^5\,\mathrm{s}^{-1}$, and the plasma is in the Pfirsch-Shlüter regime ($\nu_{PS} \sim 2 \times 10^5\,\mathrm{s}^{-1}$). In the peripheral region, the collision frequency is 8×10^4 – $2 \times 10^5\,\mathrm{s}^{-1}$, and the plasma is in the plateau regime ($\nu_B \sim 6 \times 10^4\,\mathrm{s}^{-1}$ and $\nu_{PS} \sim 3 \times 10^5\,\mathrm{s}^{-1}$). Here, $\nu_{PS} = v_{the}/Rq$ and $\nu_B = (r/R)^{3/2}\nu_{PS}$ are the characteristic collision frequencies of the Pfirsch-Shlüter and banana regimes, respectively. If the plasma is in the banana regime, the bootstrap

current can be estimated by the following equation

$$J = \frac{\sqrt{\epsilon}}{B_\theta}\frac{dp}{dr}. \tag{5.2}$$

In order to estimate the current due to bulk electrons, we use the following values: $\epsilon = 0.25\,\mathrm{m} / 0.6\,\mathrm{m} = 0.42$, $B_\theta = B_\theta(a) = 0.014\,\mathrm{T}$, $dp/dr = 3.8\,\mathrm{Pa}/(2 \times 0.25\,\mathrm{m})$. This gives an upper limit on the bootstrap current due to bulk electrons of about 1 kA, which is 4 % of the total plasma current.

The collision frequency of a typical plasma sustained by 8.2 GHz RF power is in the range 1×10^3 – $3 \times 10^4\,\mathrm{s}^{-1}$, and the plasma is in the banana regime ($\nu_\mathrm{B} \sim 2 \times 10^4\,\mathrm{s}^{-1}$). The bootstrap current due to bulk electrons is estimated to be about 0.4 kA, which is 2 % of the total plasma current. On the other hand, hard X-ray measurements indicate the presence of energetic electrons [97].

In both cases, the bootstrap current due to bulk electrons is negligible. It is inferred that the contribution of fast electrons to the plasma current is dominant.

5.3.4 Equilibrium

The poloidal beta β_p (Eq. 1.21) is an important quantity that characterizes plasma performance and affects equilibrium and stability. Here we estimate β_p of the bulk electrons for the inboard poloidal field null plasma with $B_\mathrm{T} = 0.13\,\mathrm{T}$ using Thomson scattering data (Fig. 5.6). The volume average pressure is approximated by the line averaged pressure. $B_p(a)$ is estimated by averaging the poloidal field strength on a circular circumference ($R_c = 0.6$ m, $a = 0.25$ m). The poloidal field is calculated from external coil currents and a parabolic plasma current profile. The estimated poloidal beta β_p^Thom is about 0.015. The total poloidal beta β_p^EQ can be estimated from the equilibrium relationship

$$B_v = -\frac{\mu_0 I_p}{4\pi R}\left(\ln\frac{8R}{a} + \beta_p^\mathrm{EQ} + \frac{l_i}{2} - \frac{3}{2}\right). \tag{5.3}$$

For $I_p = 17$ kA, $R = 0.63$ m, $a = 0.28$ m, and $l_i = 0.8$, β_p^EQ is about 3. While the necessary condition to form the inboard poloidal field null configuration is $\epsilon\beta_p > 1.25$ [63],in the present case $\epsilon\beta_p^\mathrm{EQ} = 1.3$. Therefore, the calculated value for β_p^EQ is reasonable.

The difference between $\beta_p^\mathrm{Thom} = 0.015$ and $\beta_p^\mathrm{EQ} = 3$ can be attributed to the contribution of high energy electrons. In general, a plasma heated by electron cyclotron wave has bulk and tail (high energy electron) components [98]. Since the energy range measured by the Thomson scattering system is 5 – 500 eV, β_p^Thom reflects the contribution of bulk electrons.

The hard X-ray temperature T_HX is calculated from the energy spectrum of hard X-ray photons in the energy range of less than 200 keV [64, 97]. For this inboard null configuration, $T_\mathrm{HX} \simeq 40\,\mathrm{keV}$ was observed. The peak of the T_HX profile is at $R_\mathrm{mid} = 0.75\,\mathrm{m}$, which corresponds to the magnetic axis. In the plasma core region, T_HX in this inboard null configuration is larger than that in the limiter configuration.

There is an asymmetry in T_HX depending on the viewing angle, in the forward vs. backward directions with respect to the current carrying electron flow. The ratio of forward to backward T_HX is 2 – 4 in RF sustained discharges. The asymmetry suggests that the plasma current is carried by electrons accelerated to high energies by ECW. Langmuir probe measurements also

confirm the existence of fast electrons [99, 100]. In limiter discharges, $T_{\mathrm{HX}} = 4$–$6\,\mathrm{keV}$ and the fast electron density is $\sim 10^{16}\,\mathrm{m}^{-3}$.

Therefore, high energy electrons with such energies exist and they contribute to β_p^{EQ}. Assuming that β_p^{EQ} is dominated by contributions from the high energy electrons, we can estimate their density to be $2 \times 10^{16}\,\mathrm{m}^{-3}$. Figure 5.10 shows the calculated model electron velocity distribution function using the parameters described above. Here, the bulk electron temperature is assumed to be 100 eV (corresponding to a thermal velocity of 6×10^6 m/s).

Furthermore, the plasma current carried by these high energy electrons can be estimated using the density and the average energy of high energy electrons. The estimated current is about 20 kA, which is roughly the same as the measured plasma current.

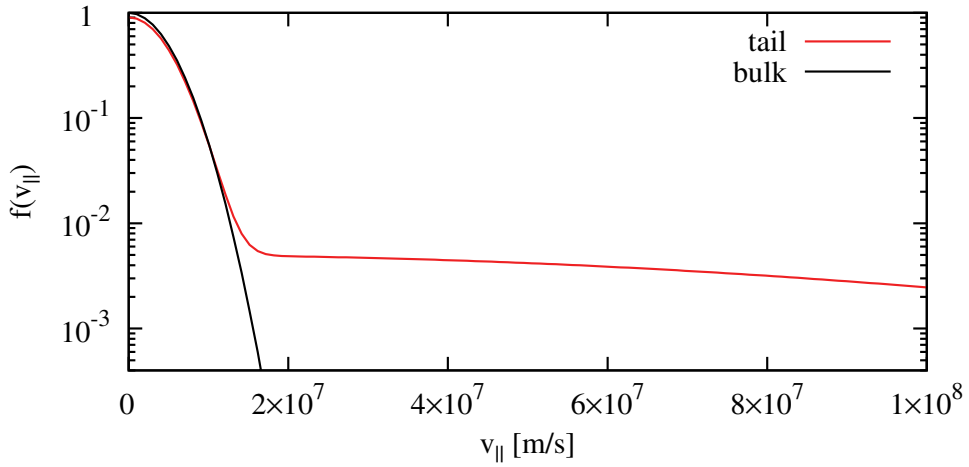

Fig. 5.10: Parallel velocity distribution function of bulk electrons (black) and all electrons including the tail component (red).

5.3.5 EBW current drive experiment

The maximum densities obtained by 28 GHz or 8.2 GHz RF power alone are much lower than respective cutoff densities. Therefore, mode conversion from the injected electromagnetic wave to EBW is not possible. In order to satisfy the condition for mode conversion, 8.2 GHz RF power was injected to a high density target plasma formed by 28 GHz RF power. Figure 5.3.5 shows the radial profiles of characteristic frequencies for such target plasma. The plasma was overdense for 8.2 GHz, so mode conversion to EBW is possible.

In this case, the injected O-mode wave would be converted to the X-mode, and then to EBW. Therefore, the total mode conversion efficiency is the product of efficiencies for these two steps. The X to EBW mode conversion efficiency C for the optimum injection angle is written as [78]

$$C \leq 4e^{-\pi\eta}(1 - e^{-\pi\eta}), \tag{5.4}$$

$$\eta = \frac{\omega_{ce} L_n}{c} \frac{\alpha}{\sqrt{\alpha^2 + 2(L_n/L_B)}} \left[\frac{\sqrt{1+\alpha^2} - 1}{\alpha^2 + (L_n/L_B)\sqrt{1+\alpha^2}} \right]. \tag{5.5}$$

The density scale length L_n of the target plasma was 0.2 m, the magnetic field scale length

L_B was 1.0 m at the upper hybrid resonance layer, and $\alpha = \omega_p/\omega_{ce} = 1.5$, which gives $\eta = 1.6$. Using these values, the maximum X to EBW mode conversion efficiency for the optimum angle is calculated to be 2 %.

The efficiency of O to X mode conversion is 100 % at the optimum angle, but it decreases when the angle deviates from the optimum. The angular dependence is given by Eq. (2.6), and the FWHM angle is given in terms of $N_\parallel$ as

$$\Delta N_{\parallel FWHM} = 2\log(2)\left\{\pi k_0 L_n \sqrt{\frac{Y}{2}}\,[2(1+Y)]\right\}^{-\frac{1}{2}}, \tag{5.6}$$

$$N_\parallel = \frac{ck_\parallel}{\omega}. \tag{5.7}$$

The FWHM angle around the optimum angle is 4.3 degrees, which corresponds to the refractive index range of 0.08. Therefore, in the present EBW current drive experiment, it is reasonable that we did not observe a clear dependence on the injection angle (Appendix B). Optimization of the target plasma and the injection angle remains a future work.

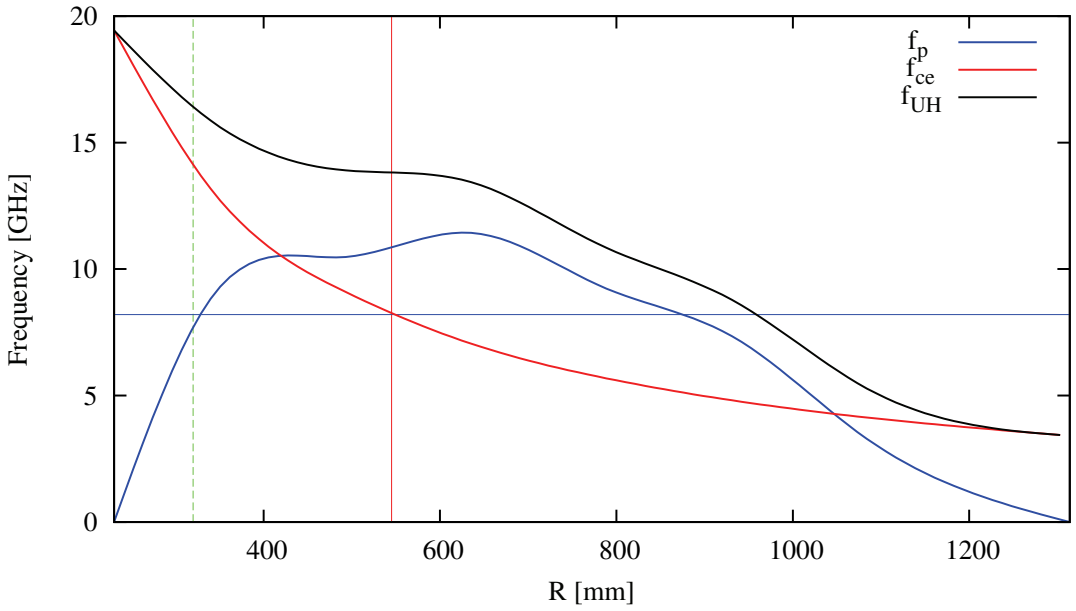

Fig. 5.11: Plot of the plasma frequency f_p, electron cyclotron frequency f_{ce}, and the upper hybrid frequency f_{UH}. The red vertical bar indicates the fundamental resonance layer for 8.2 GHz, the green vertical bar indicates the second harmonic resonance layer for 28 GHz, and the blue horizontal bar indicates 8.2 GHz.

Chapter 6

Conclusions

A new Thomson scattering system was developed for QUEST, and electron temperature and density profiles, as well as their time evolutions were measured successfully. A Nd:YAG laser (wavelength 1064 nm, energy 1.65 J, pulse width 7 ns, and repetition rate 10 Hz) was used as the light source. The scattered light was collected by a spherical mirror and transmitted by fiber optic cables. Measurements were made at six spatial points in the plasma by six polychromators, each with six wavelength channels.

The scattered signals from plasmas sustained by 8.2 GHz RF power are quite low, because the electron density is extremely low. In such cases, we have demonstrated that signal accumulation of repetitive laser pulses is quite effective. The scattered signals were accumulated during the steady state period (typically $\sim$ 10 s), and also over many reproducible discharges. Up to 2000 pulses were accumulated to obtain a very high signal-to-noise ratio. Using this Thomson scattering system, (i) the inboard poloidal field null configuration sustained by 8.2 GHz RF power alone, and (2) the limiter configuration sustained by 28 GHz RF power alone were studied extensively.

(i) The electron temperature obtained in steady-state spherical tokamak plasmas sustained by 8.2 GHz RF power was in the range of 10 – 500 eV. The density was much lower than the cutoff density for 8.2 GHz (by a factor of five). Unlike in typical conventional tokamak plasmas, the temperature profile was hollow. The peak position of the electron temperature profile was located slightly to the low field side of the fundamental electron cyclotron resonance layer. When the toroidal magnetic field strength was increased, the peak position of the electron temperature profile moved towards the low field side (larger major radius side) as the fundamental resonance layer moved outward, indicating that the electrons are heated by electron cyclotron damping. The observation that the electron temperature peak is always on the low field side of the resonance layer can be interpreted by the Doppler up-shift effect, or by the poor confinement of the plasma on the high field side because of the shrinking plasma cross section. The inboard poloidal field null configuration has an X-point (poloidal field null) on the inboard side of the torus, and is characterized by a very high poloidal beta. The poloidal beta of the bulk electrons calculated from the Thomson scattering data was much smaller ($\sim$ 0.01) than the total poloidal beta obtained from equilibrium analysis ($\sim$ 3), indicating that the contribution of energetic electrons to the pressure is dominant. Hard X-ray measurements indicate the existence of high energy electrons accelerated by ECW, and suggests strongly that the plasma current is mostly carried by these fast electrons.

(ii) In the 28 GHz RF experiment, similar features were observed, but since the fundamental resonance layer does not exist inside the vacuum vessel, heating occurs near the second harmonic resonance layer. The density is again much lower than the cutoff density for 28 GHz (by a factor of five). Therefore, mode conversion of ECW to EBW is not expected. The density is an order of magnitude higher in plasmas sustained by 28 GHz RF power (200 kW) compared with the plasmas sustained by 8.2 GHz RF power (40 kW), which is approximately the ratio of cutoff densities for the two frequencies. The central and the inboard pressures for the 28 GHz case are about twice and four times higher than the 8.2 GHz case. Since the injected power is about five times higher for 28 GHz, the pressure difference is reasonable. In both cases, the peak position of the electron temperature profile is located near the resonance layer. The central region has the highest density and a lower temperature. This is probably due to poor RF accessibility to the high density core region and poor central confinement due to collisions with neutrals or due to radiative cooling. In plasmas sustained by 28 GHz RF power, the outboard temperature is higher than the central temperature, but lower than the inboard temperature. The pressure profile is asymmetric due to imperfect temperature equilibration over the flux surface.

In conclusion, the electron temperature and density profiles were measured successfully in QUEST using the newly developed Thomson scattering system. These measurements have revealed various features of the electron temperature and density profiles in the low density ($\leq 2 \times 10^{18}\,\mathrm{m}^{-3}$), RF-driven steady state QUEST plasmas. These results provide important experimental evidence for understanding spherical tokamak plasmas sustained solely by RF power.

Acknowledgements

I would like to thank the members of the Takase-Ejiri Laboratory. Professor Takase and Associate Professor Ejiri gave me many effective and detailed advices and instructions. Associate Professor Nagashima advised me and helped me on QUEST. Professor Zushi, Assistant Professor Hasegawa, Professor Hanada, Professor Nakamura, Professor Fujisawa, Associate Professor Idei, Dr. Santanu, Dr. Onchi, Mr. Mishra and other members of the QUEST Team for their help on QUEST. Professor Narihara gave me important information and advices related to Thomson scattering. Dr. Tojo, Dr. Hiratsuka, Mr. Togashi and Mr. Nakamura helped me with Thomson scattering. Dr. Watanabe helped me in Kyushu and Dr. Ohsako helped me in Tokyo. Other member of the TST-2 Group, Assistant Professor Tsujii, Mr. Kakuda, Dr. Wakatsuki, Mr.Sonehara, Mr. Furui, Mr. Shinya, Mr. Imamura, Mr. Inada, and Mr. Tsuda helped me in various ways. This thesis work could not have been completed without their help.

Appendix A

Profiles measured in other magnetic configurations

A.1 Limiter configuration

Electron temperature and density profile s were measured in an inboard limited plasma with a plasma current of 8 kA, sustained by 75 kW of 8.2 GHz RF power (Fig. A.1). The toroidal magnetic field was $B_{\mathrm{T}} = 0.20\,\mathrm{T}$ ($I_{\mathrm{TF}} = 40\,\mathrm{kA}$) and the fundamental resonance layer was located at $R = 440\,\mathrm{mm}$. The inboard LCFS touches the inboard limiter, while the outboard LCFS is located at $R = 1100\,\mathrm{mm}$.

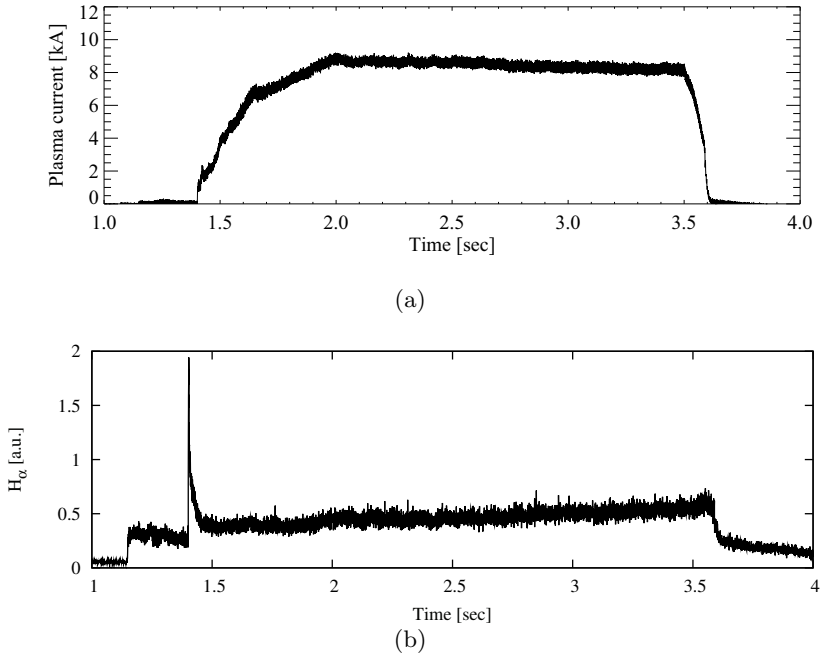

Fig. A.1: Evolutions of plasma current (a) and Hα line emission (b) for a limiter configuration discharge (shot no. 15238).

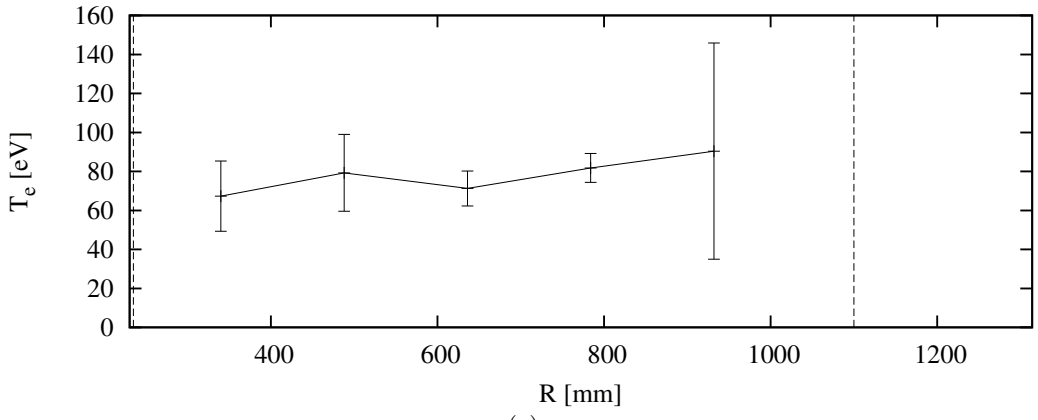

(a)

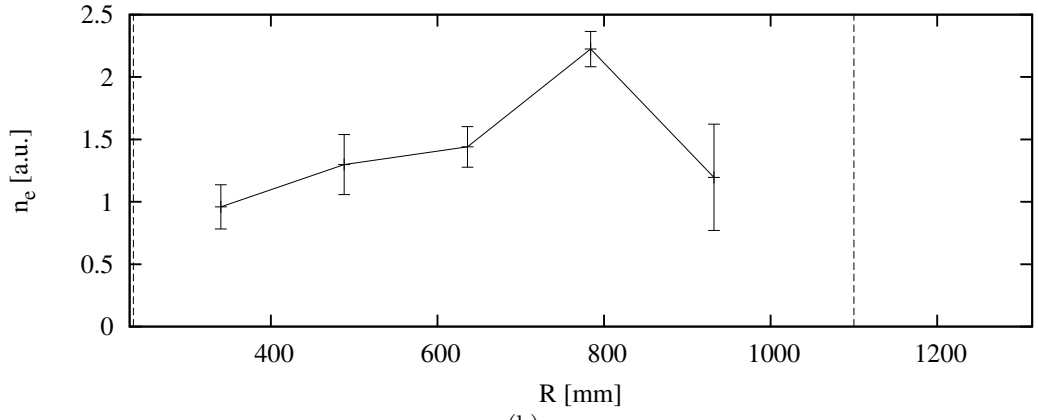

(b)

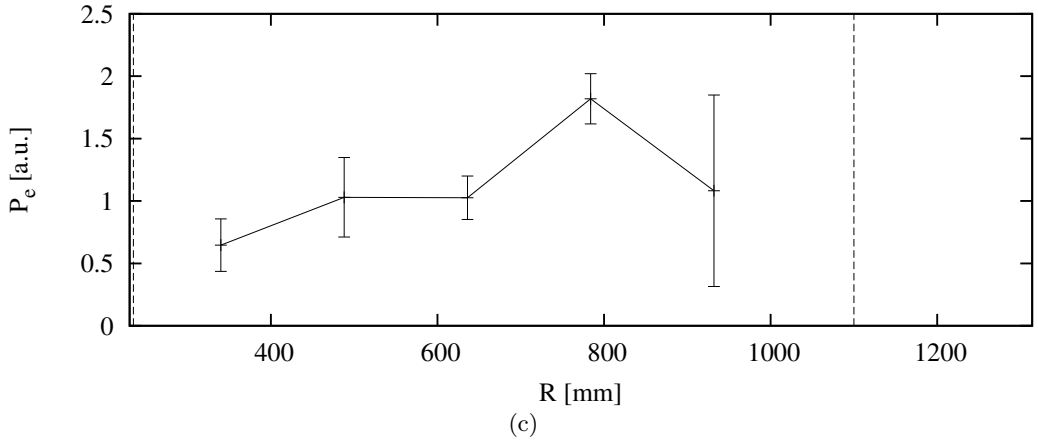

(c)

Fig. A.2: Profiles of electron temperature (a), density (b), and pressure (c) for a limiter configuration plasma with $B_T = 0.20\,T$ (shot nos. 15238 – 15261, 2.0 – 3.5 s). The dashed vertical lines indicate the inboard and outboard positions of LCFS determined by RTFIT.

A flat electron temperature profile was obtained (Fig. A.2). In QUEST limiter configuration plasmas, a peaked temperature profile has not been observed so far.

A.2 Divertor configuration

Electron temperature and density profiles were measured in a divertor configuration plasma with a plasma current of 13 kA, sustained by 105 kW of 8.2 GHz RF power (Fig. A.3). The temperature profile has a peak in the plasma core (Fig. A.4).

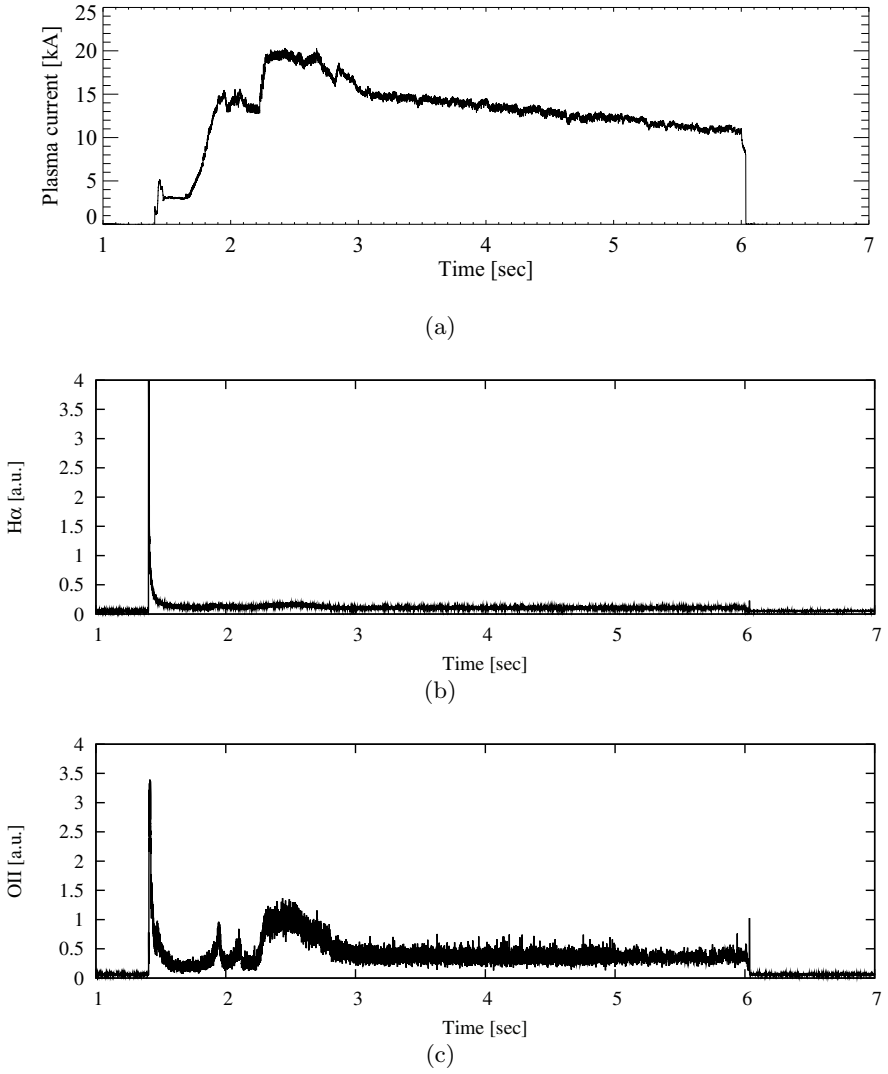

Fig. A.3: Evolutions of plasma current (a) Hα line emission (b) and OII line emission (c) for a divertor configuration discharge (shot no. 19209).

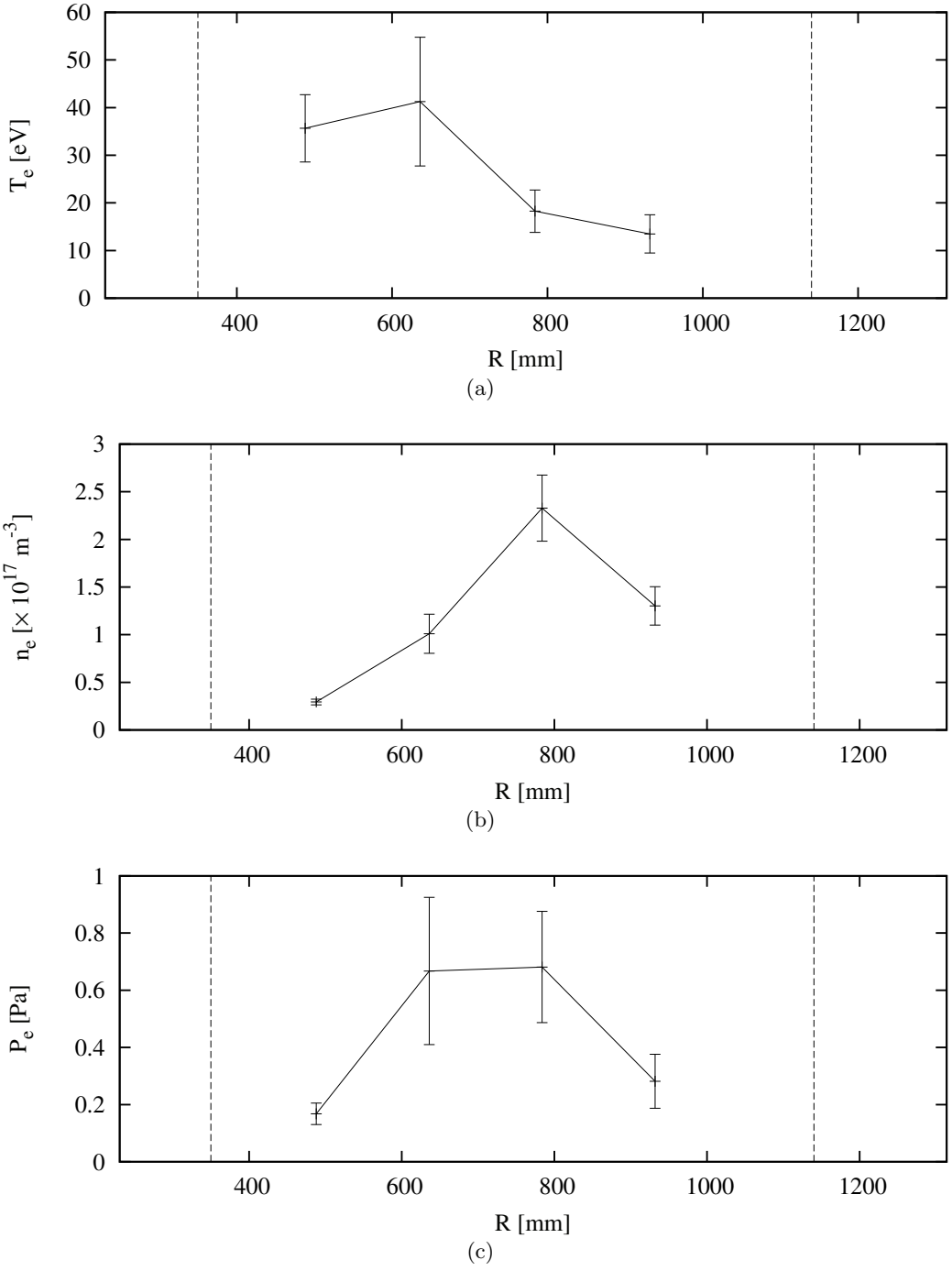

Fig. A.4: Profiles of electron temperature (a), density (b) and pressure (c) for a divertor configuration plasma with $B_T = 0.13\,T$ (shot nos. 19209 – 19217, 3.3 – 5.7 s). The dashed vertical lines indicate the inboard and outboard positions of LCFS determined by RTFIT.

A.3 Ohmic discharge

Profiles were measured in an inboard limited Ohmic discharge (Fig. A.5). Profiles measured at $t = 1.3\,\mathrm{s}$, when the scattered signal was maximum, are shown in Fig. A.6. The Ohmic heating power is weak and the electron temperature is much lower compared to other tokamaks [2]. The electron density is an order of magnitude higher than in noninductively sustained plasmas.

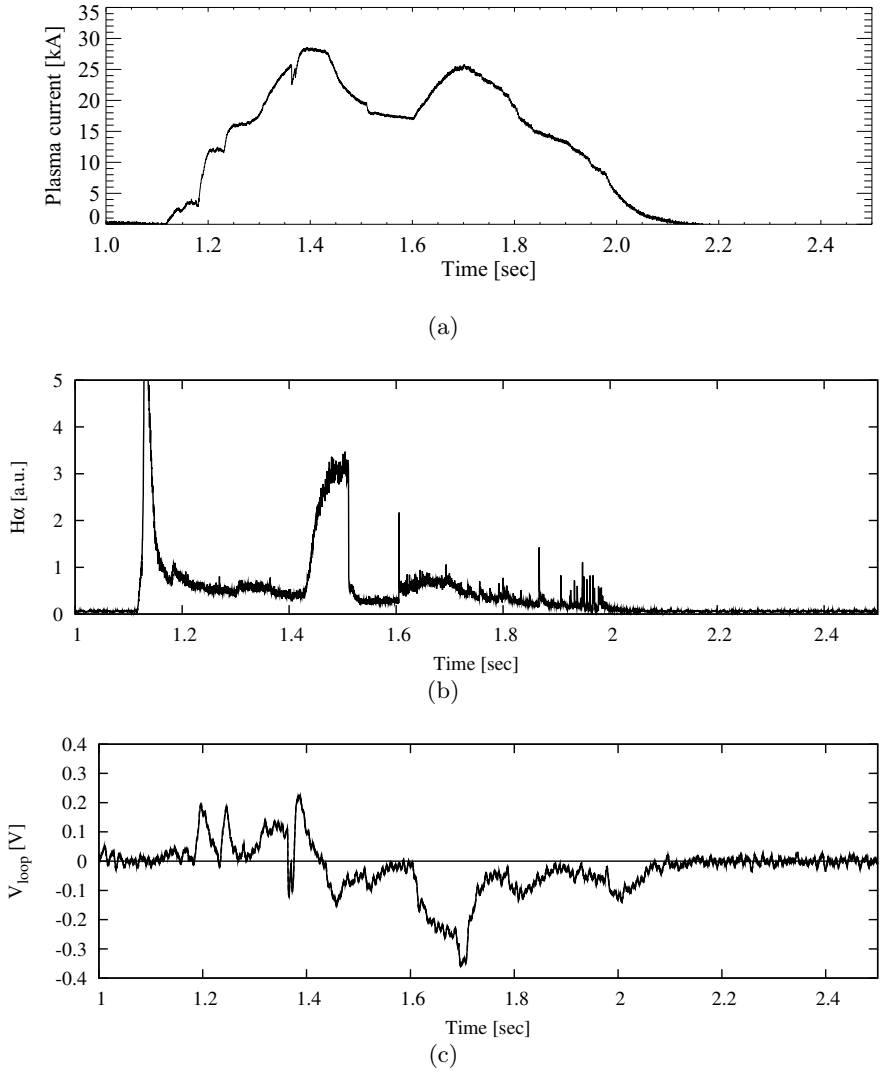

Fig. A.5: Evolutions of plasma current (a), Hα line emission (b), and loop voltage (c) for an inboard limited Ohmic discharge (shot no. 23659).

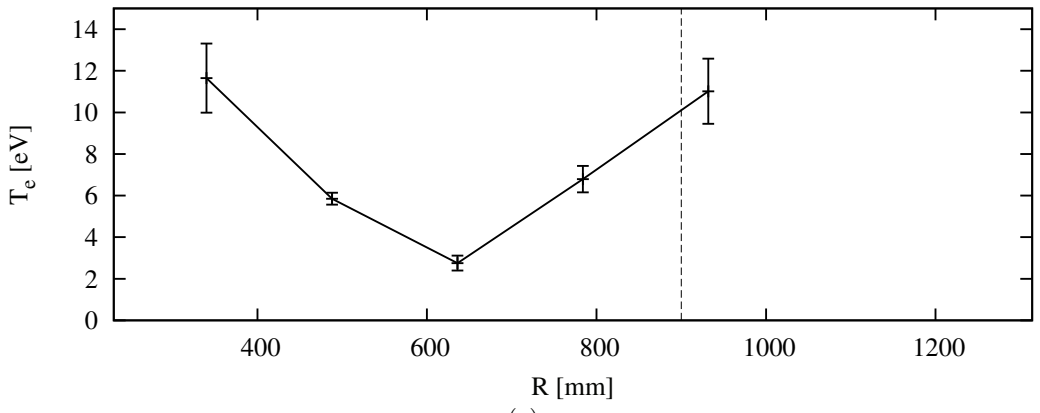

(a)

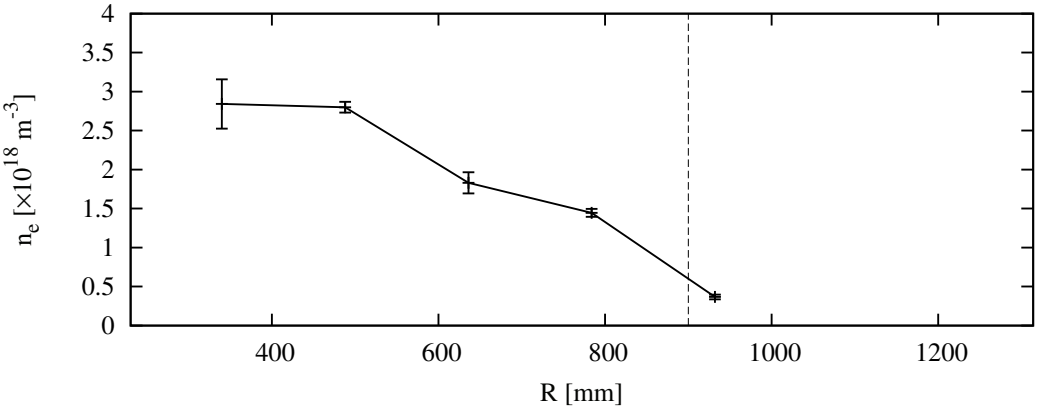

(b)

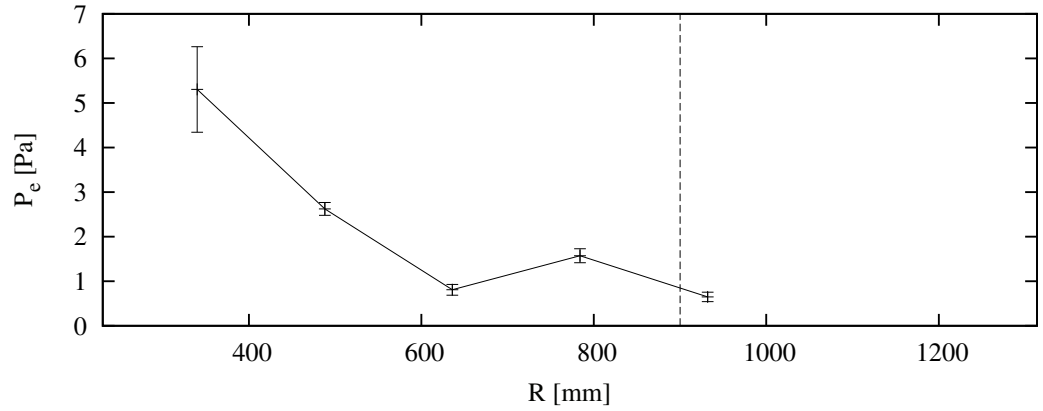

(c)

Fig. A.6: Profiles of electron temperature (a), density (b) and pressure (c) for an inboard limited Ohmic discharge (shot no. 23659 at 1.3 s). The dashed vertical line indicates the outboard position of LCFS determined by RTFIT.

Appendix B

8.2 GHz additional heating of 28 GHz sustained plasma

8.2GHz RF power was injected into an overdense plasma sustained by 28 GHz RF power (Fig. B.1) to search for the effect of heating by the EBW. The 28 GHz fundamental resonance was located at $R = 160\,\mathrm{mm}$ and the second harmonic resonance was at $R = 320\,\mathrm{mm}$. The 8.2 GHz fundamental resonance was at $R = 545\,\mathrm{mm}$. No clear evidence of EBW heating of was observed (Fig. B.2).

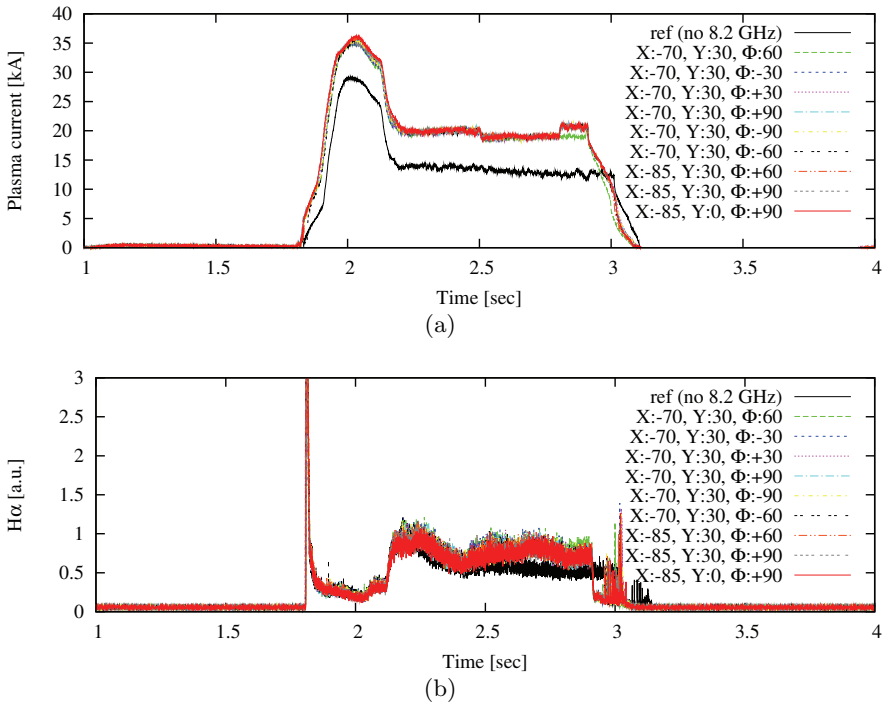

Fig. B.1: Evolutions of plasma current (a) and Hα line emission (b) for a 28 GHz ECCD discharge with 8.2 GHz additional heating.

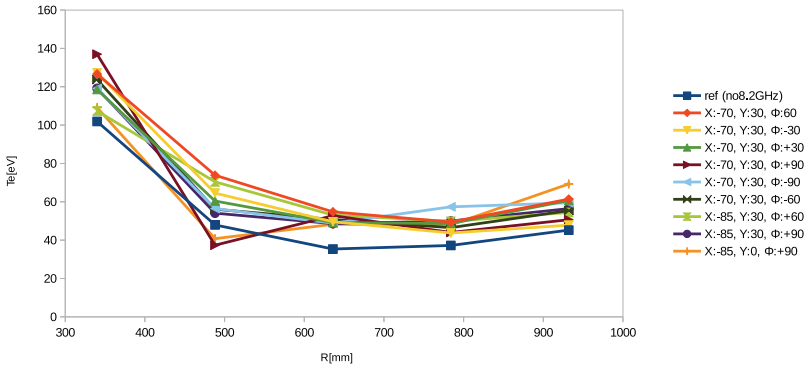

(a)

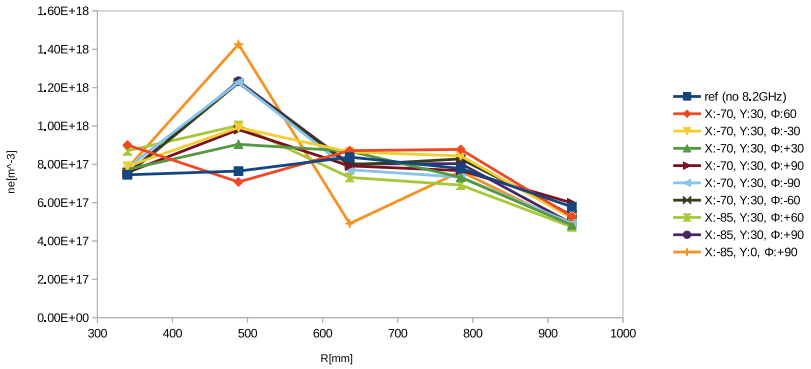

(b)

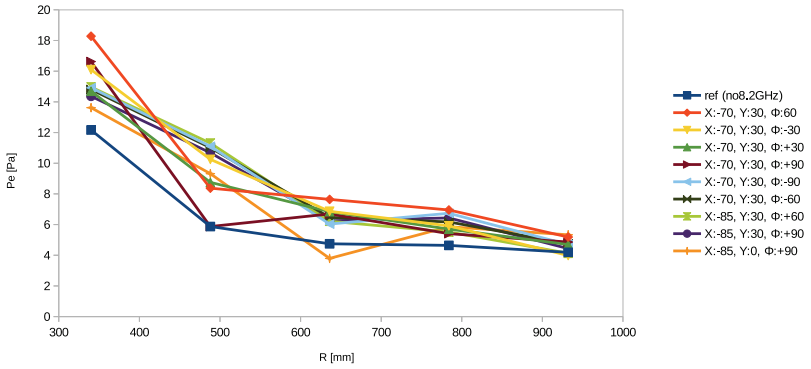

(c)

Fig. B.2: Radial profiles of electron temperature (a), density (b) and pressure (c) for a 28 GHz ECCD discharge with 8.2 GHz additional heating.

Appendix C

Compact torus injection

Compact torus (CT) injection can be used for particle fueling. Particles contained in a CT plasma can penetrate deeper into the plasma compared to gas puffing. CTs were injected into plasmas with inboard poloidal field null configuration at $t = 3.0\,\mathrm{s}$. Thomson scattering measurements were performed for the following three cases.

1. $B_\mathrm{T} = 0.18\,\mathrm{T}$ (Fig. C.1, Fig. C.2).
2. $B_\mathrm{T} = 0.18\,\mathrm{T}$, CT gas puff alone (Fig. C.3, Fig. C.4).
3. $B_\mathrm{T} = 0.13\,\mathrm{T}$ (Fig. C.5, Fig. C.6).

CT injection into plasmas with $B_\mathrm{T} = 0.18\,\mathrm{T}$ and $B_\mathrm{T} = 0.13\,\mathrm{T}$ were compared. The CT plasma has a spheromak magnetic configuration and penetrates into the target ST plasma by pushing the ST magnetic field lines away. Therefore, the injected CT plasma will not reach the plasma core if the magnetic field is too strong. In the "CT gas puff alone" case, gas puffing was performed without CT injection. In this case it is expected that the central electron density does not increase as much as in the case with CT injection. The rates of density increase and decay were slower for the CT gas puff alone case. The sharp spike observed on the Hα emission at the moment of CT injection was absent for the CT gas puff alone case. Rapid fueling by CT injection was demonstrated, with a decay time constant of 150 ms. Figure C.7 shows the ratio of the density after CT injection ($t = 3.0\,\mathrm{s}$) to that before injection ($t = 2.9\,\mathrm{s}$) at different major radial locations. No large difference is observed among different cases.

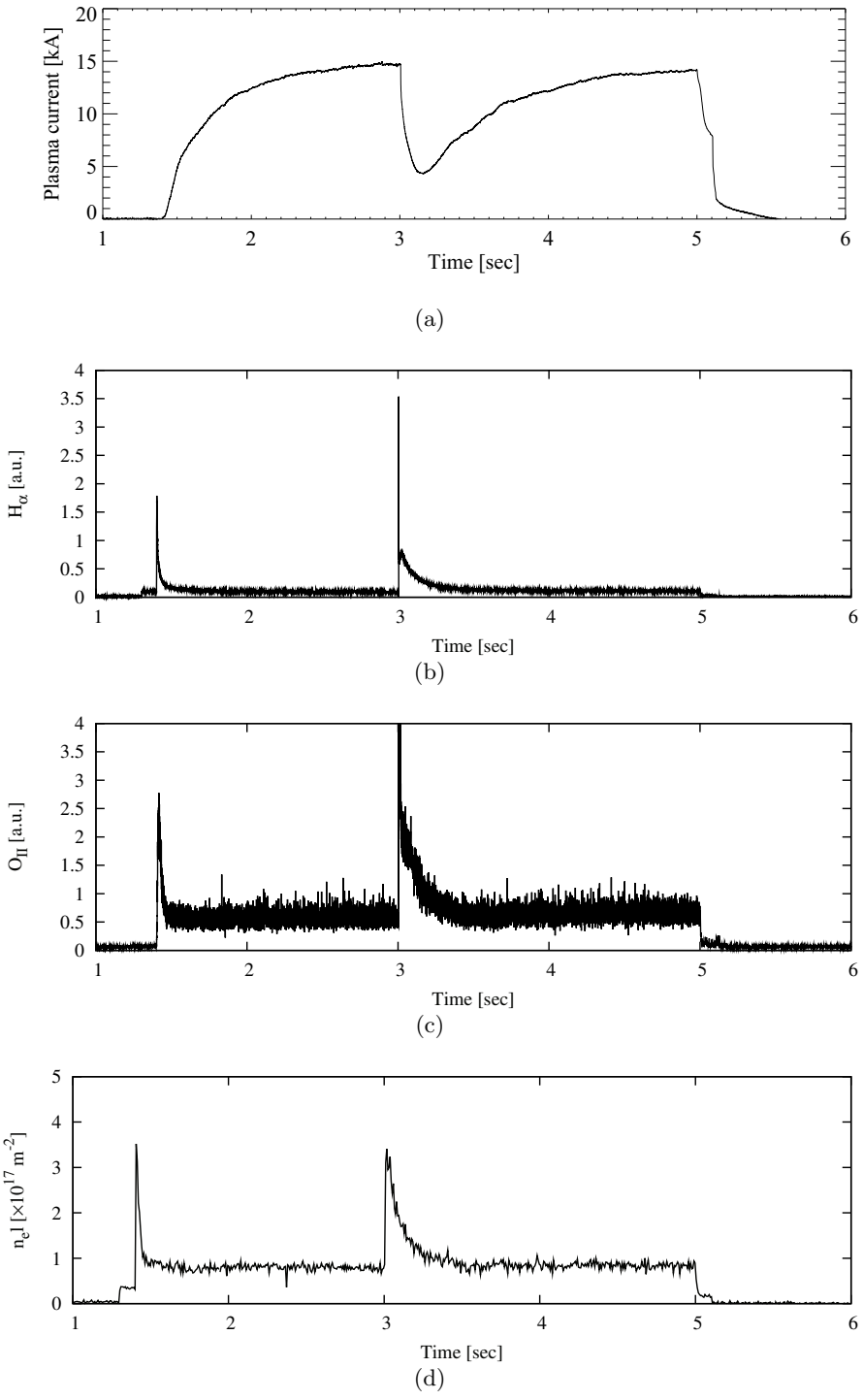

Fig. C.1: Evolutions of plasma current (a), Hα line emission (b), OII line emission (c), and line integrated density (d) for CT injection into an inboard null configuration plasma sustained by 8.2 GHz RF power ($B_{\mathrm{T}} = 0.18\,\mathrm{T}$, shot no. 21067).

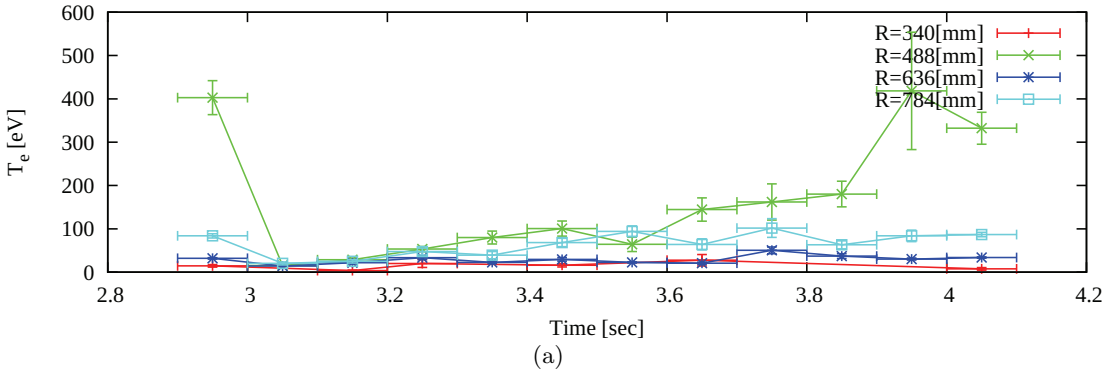

(a)

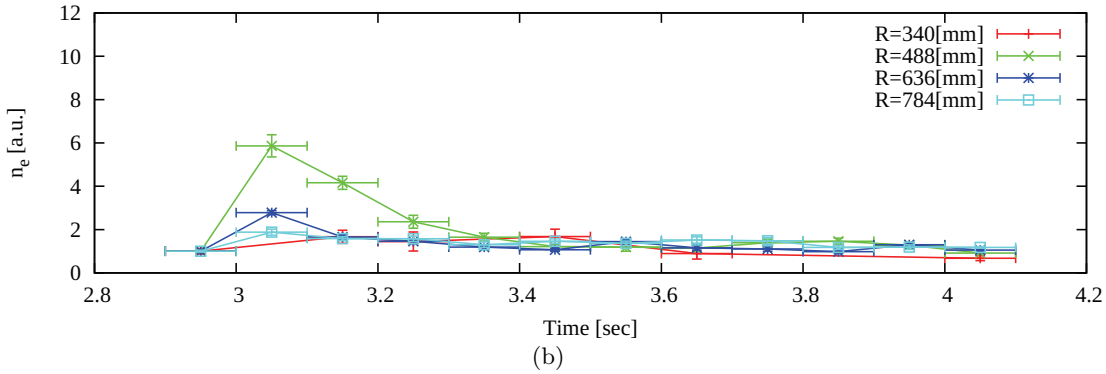

(b)

Fig. C.2: Evolutions of electron temperature (a) and density (b) for CT injection into an inboard null configuration plasma sustained by 8.2 GHz RF power ($B_{\mathrm{T}} = 0.18\,\mathrm{T}$, shot nos. 21062 – 21067).

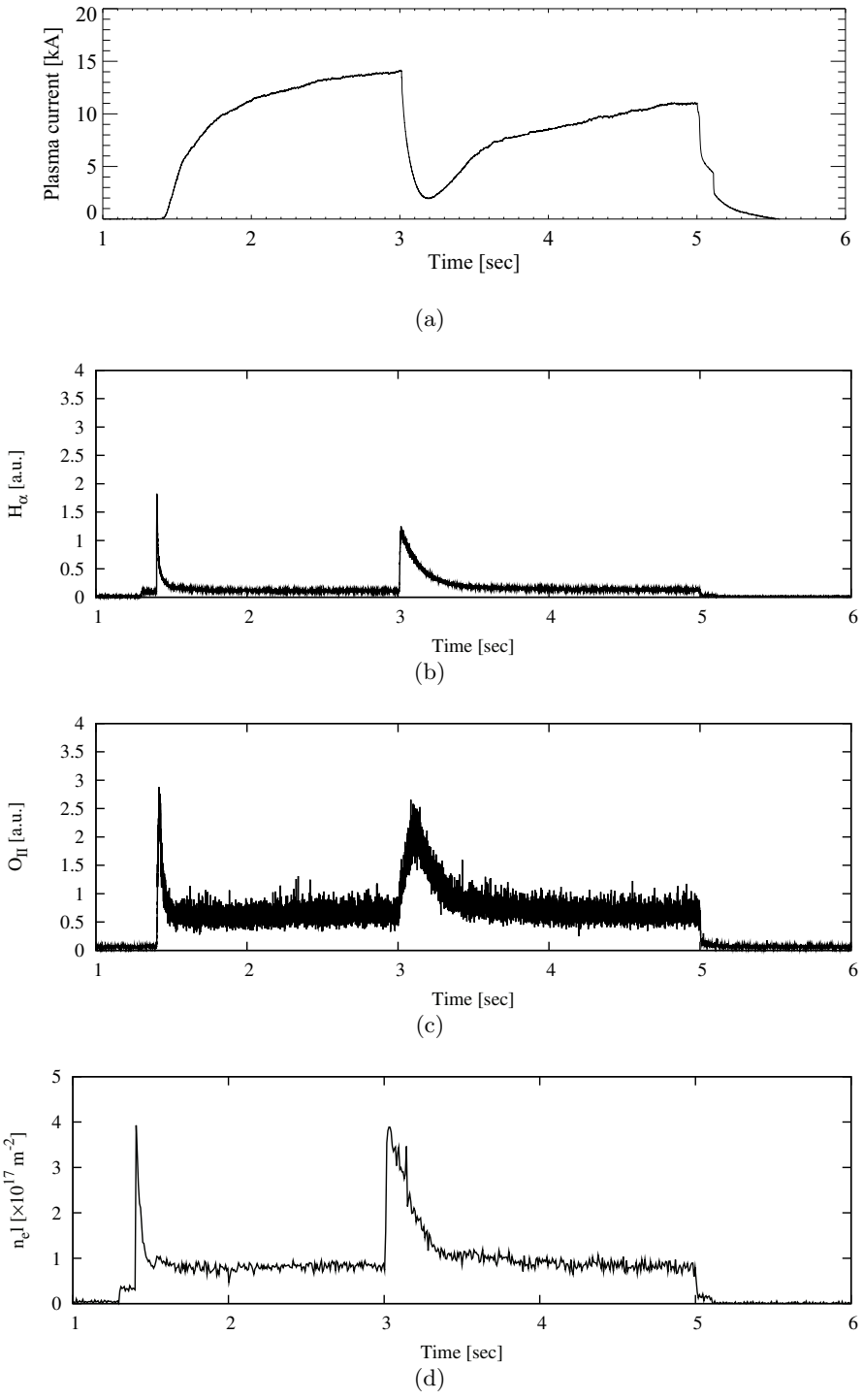

Fig. C.3: Evolutions of plasma current (a), Hα line emission (b), OII line emission (c), and line integrated density (d) for CT gas puff alone into an inboard null configuration plasma sustained by 8.2 GHz RF power ($B_{\mathrm{T}} = 0.18\,\mathrm{T}$, shot no. 21077).

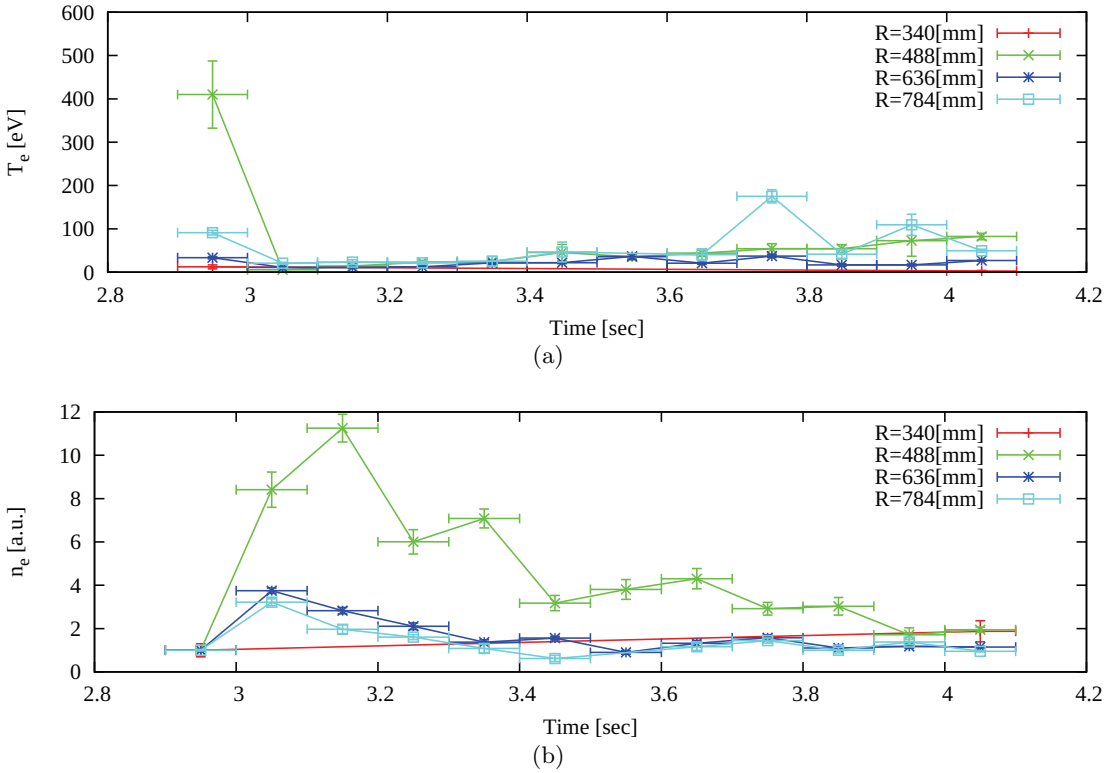

Fig. C.4: Evolutions of electron temperature (a) and density (b) for CT gas puff alone into an inboard null configuration plasma sustained by 8.2 GHz RF power ($B_{\mathrm{T}} = 0.18\,\mathrm{T}$, shot nos. 21077 – 21080).

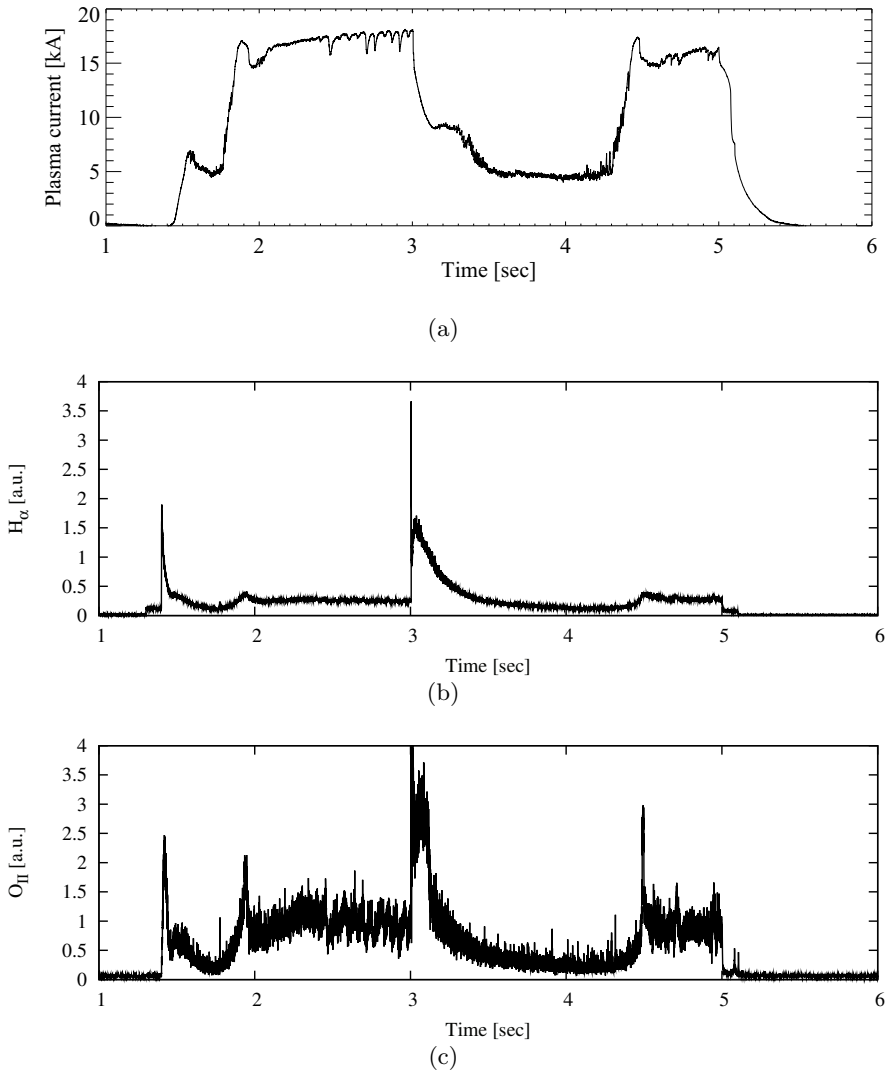

Fig. C.5: Evolutions of plasma current (a), Hα line emission (b), OII line emission (c), and line integrated density (d) for CT injection into an inboard null configuration plasma sustained by 8.2 GHz RF power ($B_{\mathrm{T}} = 0.13\,\mathrm{T}$, shot no. 21081).

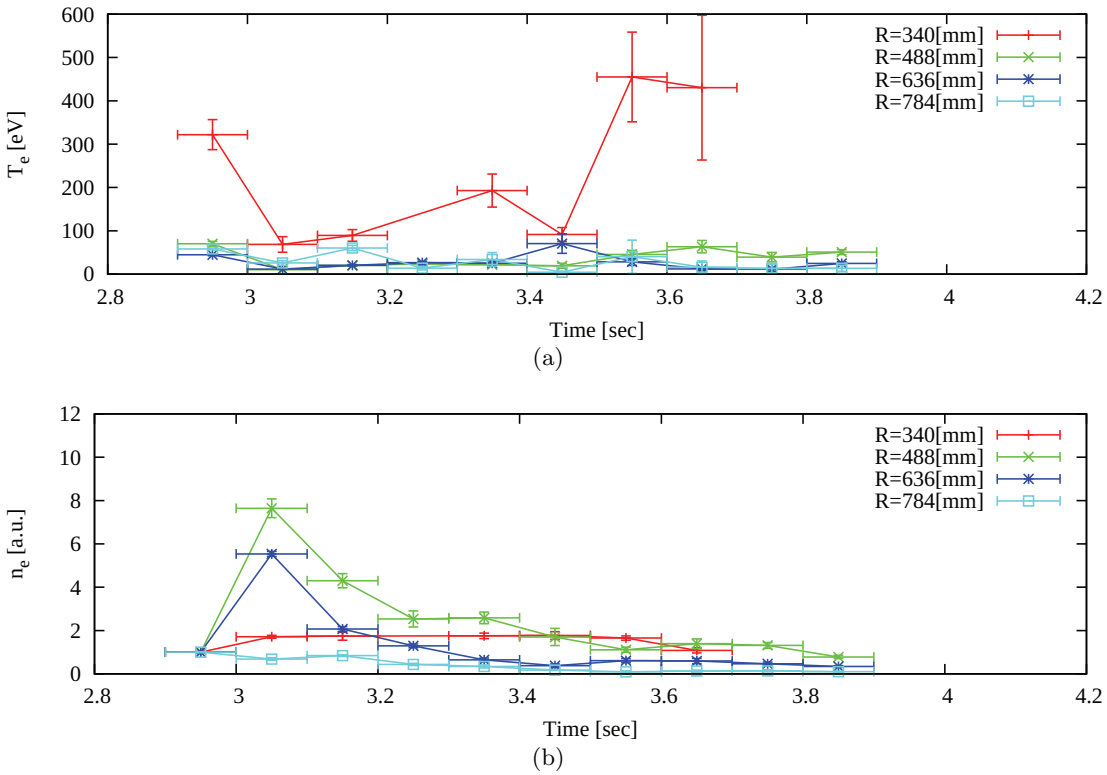

Fig. C.6: Evolutions of electron temperature (a) and density (b) for CT injection into an inboard null configuration plasma sustained by 8.2 GHz RF power ($B_T = 0.13\,T$, shot nos. 21081 – 21086).

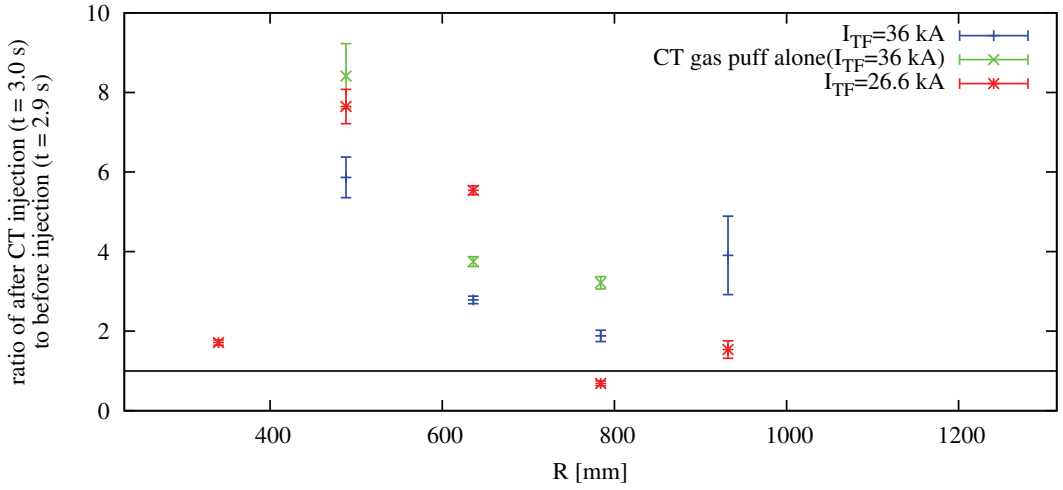

Fig. C.7: The ratio of density after CT injection ($t = 3.0\,s$) to that before injection ($t = 2.9\,s$) at various major radii.

Bibliography

[1] F. F. Chen, Introduction to Plasma Physics and Controlled Fusion, T. Uchida, trans. (Maruzen, Tokyo 1977).

[2] J. Wesson, Tokamaks 3rd edition (Oxford Univ. Press, New York 2004).

[3] K. Miyamoto, Fundamentals of Plasma Physics and Controlled Fusion Revised Edition (Univ. Tokyo Press, Tokyo 2001).

[4] T. H. Stix, Waves in Plasmas (AIP, New York 1992).

[5] S. Ide and the JT-60 Team, Nucl. Fusion **45**, S48 (2005).

[6] J. Paméla et al., Nucl. Fusion **43**, 1540 (2003).

[7] A. Iiyoshi et al., Nucl. Fusion **39**, 1245 (1999).

[8] M. Hirsch et al., Plasma Phys. Control. Fusion **50**, 053001 (2008).

[9] P. Martin et al., Nucl. Fusion **49**, 104019 (2009).

[10] R. D. Wood et al., Nucl. Fusion **45**, 1582 (2005).

[11] D. B. Montgomery, Proceedings of the IEEE **69**, 977 (1981).

[12] T. Cho et al., Fusion Sci. Tech. **51**, 11 (2007).

[13] JAEA web site, http://www.naka.jaea.go.jp/ITER/.

[14] Y. K. M. Peng, Nucl. Fusion **7**, 1692 (2000).

[15] S. Kubo et al., Phys. Rev. Lett. **50**, 1994 (1983).

[16] K. Toi et al., Phys. Rev. Lett. **52**, 2144 (1984).

[17] F. Jobes et al., Phys. Rev. Lett. **52**, 1005 (1984).

[18] Y. Takase et al., Phys. Fluids **30**, 1169 (1987).

[19] H. Zushi et al., Nucl. Fusion **45**, S142 (2005).

[20] K. Ogura et al., Nucl. Fusion **30**, 611 (1990).

[21] R. Prater, Journal of Fusion Energy, **9**, 19 (1990).

[22] R. M. Gilgenbach et al., Phys. Rev. Lett. **44**, 647650 (1980).

[23] Z. A. Pietrzyk et al., Phys. Rev. Lett. **86**, 15301533 (2001).

[24] G. L. Jackson et al., Nucl. Fusion **51**, 083015 (2011).

[25] M. Uchida et al., Nucl. Fusion **51**, 063031 (2011).

[26] A. Ejiri et al., Nucl. Fusion **46**, 709 (2006).

[27] J. Sugiyama et al., Plasma Fusion Res. **3**, 026 (2008).

[28] A. Ejiri et al., Nucl. Fusion **49**, 065010 (2009).

[29] Y. Takase et al., Nucl. Fusion **53**, 063006 (2013).

[30] T. Wakatsuki et al., "Results of lower hybrid wave experiments using a dielectric loaded waveguide array antenna on TST-2", 20th Top. Conf. Radiofrequency Power in Plasmas (Sorrento, Italy, 2013) AIP Conf. Proc. **1580**, 422 (2014)

[31] T. Maekawa et al., Phys. Rev. Lett. **86**, 3783 (2001).

[32] V. Shevchenko et al., Phys. Rev. Lett. **89**, 265005 (2002).

[33] A. Mueck et al., Phys. Rev. Lett. **98**, 175004 (2007).

[34] G. Taylor et al., Phys. Plasmas **11**, 4733 (2004).

[35] A. D. Piliya et al., Plasma Phys. Control. Fusion **47**, 379 (2005).

[36] R. A. Cairns et al., Phys. Plasmas **7**, 4126 (2000).

[37] C. B. Forest et al., Phys. Plasmas **7**, 1352 (2000).

[38] M. Uchida et al., "Noninductive Formation of Spherical Tokamak at 7 Times the Plasma Cutoff Density by Electron Bernstein Wave Heating and Current Drive on LATE", EX/P6-18, Proc. 24TH IAEA FUSION ENERGY CONFERENCE 8–13 October 2012, San Diego, USA.

[39] V. F. Shevchenko et al., Nucl. Fusion **50**, 022004 (2010).

[40] N. J. Peacock et al., Nature **224**, 488 (1969).

[41] H. Murmann et al., Rev. Sci. Instrum. **63**, 4941 (1992).

[42] K. Narihara et al., Rev. Sci. Instrum. **72**, 1122 (2001).

[43] T. Hatae et al., Fusion Eng. Des. **34-35**, 621 (1997).

[44] R. Scannell et al., Rev. Sci. Instrum. **79**, 10E730 (2008).

[45] D. M. P. Marquez et al., Rev. Sci. Instrum. **81**, 10D525 (2010).

[46] M. D. Bowden et al., J. Appl. Phys. **73**, 2732 (1993).

[47] T. Hori et al., Sci. Technol. **14**, 144 (1996).

[48] T. Hori et al., Appl.Phys. Lett. **69**, 3683 (1996).

[49] T. Hori et al., J. Phys. Lett. **83**, 1909 (1998).

[50] M. A. M. ElSabbagh et al., Appl. Phys. Lett. **78**, 3187 (2001).

[51] H. Röhr et al., Nucl. Fusion **22**, 1099 (1982).

[52] S. Kainaga et al., Plasma Fusion Res. **3**, 027 (2008).

[53] T. Yamaguchi et al., Plasma Fusion Res. **5**, S2092 (2010).

[54] H. Zushi et al., Nucl. Fusion **43**, 1600 (2003).

[55] M. Sakamoto et al., Nucl. Fusion **44**, 693 (2004).

[56] K. Hanada et al., Plasma Fusion Res. **5**, S1007 (2010).

[57] H. Zushi, "The overview of QUEST experiments", The 5th QUEST Symposium (Kasuga, Japan, 30-31 August 2010) paper III-4, http://www.triam.kyushu-u.ac.jp/QUEST_HP/5th_sympo.html [in Japanese].

[58] J. Roth et al., Journal of Nuclear Materials **390-391**, 1 (2009).

[59] R. Raman et al., Nucl. Fusion **37**, 967 (1997).

[60] M. Nagata et al., Nucl. Fusion **41**, 1687 (2001).

[61] N. Fukumoto et al., Nucl. Fusion **44**, 982 (2004).

[62] H. Zushi, "The recent experiments result of QUEST", The 6th QUEST Symposium (Kasuga, Japan, 2-3 August 2011) paper II-5, http://www.triam.kyushu-u.ac.jp/QUEST_HP/6th_sympo.html [in Japanese].

[63] S. A. Sabbagh et al., Phys. Fluids B **3**, 2277 (1991).

[64] S. Tashima et al., Plasma Fusion Res. **8**, 2402118 (2013).

[65] Theory group at General Atomics web site, https://fusion.gat.com/theory/Efit.

[66] T. Yoshinaga et al., Nucl. Fusion **47** 210 (2007).

[67] M. Ishiguro et al., J. Phys.: Conf. Ser. **511** 012041 (2014).

[68] M. Hasegawa, private communication (2012).

[69] H. Idei, "The present state of the steady electron Bernstein heating and current drive system", The 5th QUEST Symposium (Kasuga, Japan, 30-31 August 2010) paper III-6, http://www.triam.kyushu-u.ac.jp/QUEST_HP/sympo/5th_sympo.html [in Japanese].

[70] V. Erckmann et al., Plasma Phys. Control. Fusion **36**, 1869 (1994).

[71] I. B. Bernstein, Phys. Rev. Let. **109**, 10 (1958).

[72] A. G. Litvak et al., Phys. Lett. A **188**, 64 (1994).

[73] S. Nakajima et al., Phys. Lett. A **124**, 295 (1987).

[74] S. Nakajima et al., Phys. Rev. A **38**, 43734376 (1988).

[75] A. K. Ram et al., Phys. Plasmas **7**, 4084 (2000).

[76] A. K. Ram et al., Phys. Plasmas **9**, 409 (2002).

[77] F. W. Crawford et al., J. Applied Physics **36**, 2930 (1965).

[78] H. P. Laqua, Plasma Phys. Control. Fusion **49**, R1(2007).

[79] H. Idei et al., Journal of Plasma and Fusion Research SERIES **8**, 1104 (2009).

[80] E. Kalinnikova et al., IEEJ Transactions on Fundamental and Materials, **132**, 505 (2012).

[81] H. Idei et al., "Electron Bernstein Wave Heating and Current Drive Effect in QUEST", EX/P6-17, Proc. 24TH IAEA FUSION ENERGY CONFERENCE 8–13 October 2012, San Diego, USA.

[82] I. H. Hutchinson et al., Principles of plasma diagnostics (Cambridge Univ. Press, Cambridge 1987).

[83] J. Sheffield, Plasma Scattering of Electromagnetic Radiation (Academic Press, NewYork 1975).

[84] T. Matoba et al., Japanese Journal of Applied Physics **18**, 1127 (1979).

[85] Continuum, Power Lite 8010, USA.

[86] Fiberguide Industries, Inc., Plastic Clad Silica APC Data Sheet, New Jersey, USA.

[87] PerkinElmer Optoelectronics, Avalanche Photodiode a User Guide, Fremont, California, USA.

[88] Hamamatsu Photonics, Si APD / Selection guide.

[89] Hamamatsu Photonics, S8890-30 data sheet.

[90] I. Yamada et al., Rev. Sci. Instrum. **74**, 1675 (1999).

[91] C. M. Penny et al., J. Opt. Soc. America **64**, 712 (1974).

[92] B. Kurzan et al., Plasma Phys. Control. Fusion **46**, 299 (2004).

[93] W. H. Press et al., Numerical Recipes in C. 2nd Edition, (Cambridge Univ. Press, Cambridge 1992).

[94] Marquardt, J. Soc. Ind. Appl. Math. **11**, 431 (1963).

[95] G. Giruzzi et al., Current Drive and Profile Control in NET Plasmas, Nieuwegein (1989).

[96] H. Zushi et al., "Non-inductive Current Start-up and Plasma Equilibrium with an Inboard Poloidal Field Null by Means of Electron Cyclotron Waves in QUEST", EX/P2-14, Proc. 24TH IAEA FUSION ENERGY CONFERENCE 8–13 October 2012, San Diego, USA.

[97] S. Tashima et al., Nucl. Fusion **54** 023010 (2014).

[98] A. Montes et al., Phys. Fluids **29**, 2988 (1986).

[99] M. Ishiguro et al., Rev. Sci. Instrum. **82**, 113509 (2011).

[100] M. Ishiguro et al., Phys. Plasmas **19**, 062508 (2012).